Severe mesoscale weather events over the Nordic Seas: Numerical modelling and sensitivity experiments

Muralidhar Adakudlu

Dissertation for the degree of Philosophiae Doctor (PhD)

Faculty of Mathematics and Natural sciences
University of Bergen

April 2011

Acknowledgements

I wish to avail this opportunity to express my indebtedness to my supervisor Dr. Idar Barstad for his valuable guidance and advice during the last three and a half years. It is because of his constant encouragement and timely scrutinies of my work that I could attain my research goals without much temporal set-backs. The discussions I had with my co-supervisors−Dr. Haraldur Ólafsson and Dr. Melvyn Shapiro−have helped me a lot to prepare the articles presented in this thesis in the current form. I am grateful to you, Haraldur and Mel. I would also like to extend my gratitude to Dr. Nils Gunnar Kvamstø for reviewing my articles and providing crucial feedbacks. I appreciate Dr. Jürgen Bader for his clever questions regarding my work and helping me with technicalities of scientific computing. My office-mate and friend, Giulio, and other friends at the Geophysical Institute too deserve a part of my acknowledgement for making the research atmosphere lively. Thanks a lot, friends. My thanks also go to the technical staff at Uni Computing for providing me timely help on issues related to parallel computations. Last but not the least, I would like to thank my parents for supporting and motivating me at critical situations.

Muralidhar Adakudlu
April 2011, Bergen

Abstract

The Nordic seas region, due to its unique geographical and climatological conditions, experiences a number of adverse mesoscale weather events that have proven fatal for human activities in the area. Most of these weather events occur in the winter season and include orography-induced wind extremes, shallow and sharp fronts that often form in the vicinity of the ice edge and intense storms called polar lows. In order to assess such high impact weather conditions, a field campaign was conducted over the Nordic seas in February-March 2008 as part of the IPY-THORPEX project. During this field campaign, measurements of a number of severe weather cases were collected through the dropsonde and lidar sensors on-board the DLR-FALCON aircraft. This thesis deals with high resolution modeling experiments of some of the cases observed during the IPY-THORPEX field campaign, with focus on the sensitivity of these events to underlying surface conditions and several physical factors. The results of these experiments are presented in the form of three scientific articles.

Paper-I presents the airborne measurements of a case with strong gap winds observed at the exit region of the Hinlopen Strait in Svalbard archipelago. The DLR-FALCON aircraft flew along the Hinlopen strait and recorded winds of strength ~ 20 ms^{-1}, which was about four times higher than the upstream wind, near to the surface. In addition, formation of a wake with return currents in the lee of the terrain was also recorded by the lidar sensors carried by the aircraft. This case was simulated in a fine-resolution numerical model with a high degree of accuracy. The simulations showed the existence of small-scale cloud banners extending downstream of the lee of the mountains. The causal mechanisms for such cloud features were investigated through an idealised approach. The ideal experiments indicated that the vertical circulations set up by the terrain features cause the cloud banners and a relatively warm ocean surface maintains them by supplying moisture and buyoancy.

In paper-II, numerical simulations of another adverse weather case occurred during the IPY-THORPEX field campaign is described. The simulations indicated the formation of a low pressure system at the surface over the Barents Sea on 29 February 2008. Later on, the low intensified while propagating in a northwestward direction and crossed the ice-edge on 1 March followed by its dissipation. The sensitivity of this surface low to underlying surface conditions is explored in two sensitivity experiments, wherein the ice-cover was removed in the first and the sea-surface temperature was raised by 5 K in the second. The Barents Sea surface low persists for a longer duration in the no-ice experiment but eventually dissolves, perhaps due to high static stability in the region. In the second experiment with warmer sea-surface temperature, the surface low is found to persist near the Svalbard archipelago, leading to a significant advection of cold and stable Arctic air over to the warmer Norwegian Sea. This situation triggers

an intense polar low over the Norwegian Sea. Certain dynamical aspects of this polar low are also presented in this paper.

The sensitivity of polar lows to upper-level features and important physical factors such as static stability, baroclinicity and surface heating is the subject of paper-III. The study was carried out in a numerically set idealised baroclinic channel with a horizontal grid spacing of 10 km. The formation of polar lows was forced in the channel by imposing a finite amplitude perturbation at the tropopause level at the initial conditions. A number of sensitivity experiments were conducted, each with a different set of initial conditions that differ in the degree of baroclinicity, static stability, surface heating and the scale of upper-level perturbation. This paper shows that the pattern of the vertical motion associated with a polar low is highly sensitive to the amount of baroclinicity and surface heating. Static stability appears to have more profound influence on the growth rate of the polar low than on the associated vertical motion. The structure and scale of the polar low happens to be directly proportional to the features of upper-level perturbation.

List of papers

1. Idar Barstad and Muralidhar Adakudlu. 2011. *Observation and modelling of gap flow and wake formation on Svalbard*. Quarterly Journal of Royal Meteorological Society. **Accepted**.

2. Muralidhar Adakudlu and Idar Barstad. 2011. *Impacts of the ice-cover and sea-surface temperature on a polar low over the Nordic Seas: A numerical case study*. Quarterly Journal of Royal Meteorological Society. **Accepted**.

3. Muralidhar Adakudlu. 2011. *Impacts of different initial conditions on the growth of polar lows: Idealised baroclinic channel experiments*. Quarterly Journal of Royal Meteorological Society. **In review**.

Contents

List of Figures

Chapter 1

Introduction

The region comprising of the Greenland Sea, the Norwegian Sea, the Barents Sea and a part of the ice-covered Arctic ocean is popularly referred to as 'The Nordic Seas' (Figure 1.1). This region also covers the landmasses of the eastern coast of Greenland, Iceland, coastal Norway and the Svalbard archipelago. Due to such a geographical structure, complex air-sea/land-air interactions take place in the Nordic Sea area. Further, the radiatively cooled air over the sea ice is often advected southwards over to the relatively warm ocean basins, thereby leading to the formation of sharp frontal zones associated with strong winds. From a climatological perspective, major extratropical storm tracks lie over the Nordic Sea area as shown in Figure 1.2 with green arrows. The storms propagating along these tracks, mostly in winter, lead to strong air-sea interactions. The warm North Atlantic ocean current associated with the Gulf stream brings anomalously high temperatures from tropical latitudes to the Nordic Sea area. As indicated by Figure 1.2, the temperature at 2 m depth for the present-day climate of the Nordic Seas is warmer by $\sim 10-15^0$ C than its zonal annual mean. Such a warm anomaly causes a strong meridional temperature gradient in the area. The temperature gradient attains very strong values at the Arctic ice-edge resulting in the formation of shallow and sharp baroclinic zones. Complex interactions take place between these zones and the prevailing large-scale flow. All these conditions make the Nordic Sea region prone to a wide range of mesoscale ($\sim 1-1000$ km) weather events throughout the year.

Many of these mesoscale events are of extreme nature and have caused numerous shipwrecks over the years in the Nordic Seas. As per the statistics, 56 vessels have drowned and 342 lives have lost in such accidents during the last century (according to Wilhelmsen in Grønås and Skeie, 1999). A striking feature of these severe weather events is their ability to generate strong winds and heavy precipitation over a small area. Due to such small-scale impacts of such events, several ships have sunk in the Nordic Seas within a short range from other ships that experienced no damage. In addition, owing to their small temporal and spatial scales, these severe events mostly appear as a matter of surprise with little or no signal. Therefore, reasonable forecasting of such events has been a major challenge which makes the extreme weather conditions over the Nordic Seas a potential threat to the coastal community and the human activities over this area.

Scientific research into the adverse mesoscale weather conditions over the Nordic Seas gained momentum after the advent of polar orbiting weather satellites during the

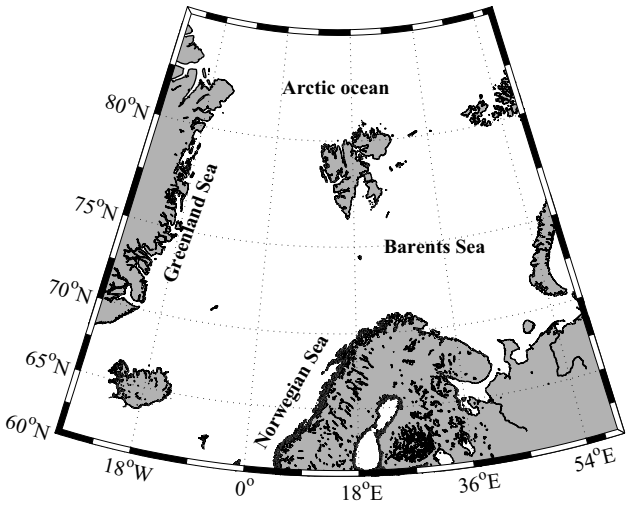

Figure 1.1: *The Nordic Seas.*

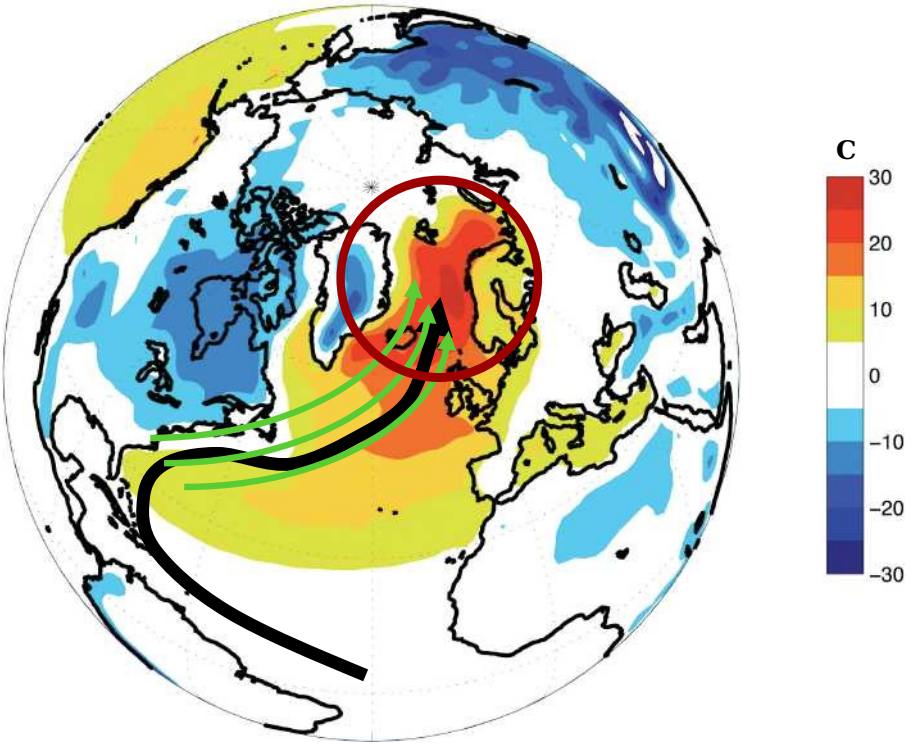

Figure 1.2: *The Nordic Sea region is shown with the deviations of 2 m temperature from its zonal annual mean (in colour) overlaid by the storm tracks (green arrows) and the North Atlantic ocean current (thick, black arrow). Adapted from Drange et al. (2005).*

mid 20^{th} century (Rasmussen and Turner, 2003). Synoptic weather maps that existed prior to the era of weather satellites were not able to show the severe events due to the mesoscale nature of such events. Furthermore, the numerical models were too coarse to simulate these mesoscale extremes. The data retrieved by the weather satellites were helpful in analysing the structure, cloudiness, wind fields and form climatologies of the extreme weather cases. Further, the availability of high performance computing techniques in recent years has been crucial in the development of sophisticated numerical models that are in use to improve the knowledge about the driving physical processes

and dynamics of the extreme events.

The mesoscale extremes over the Nordic Seas have been reported to be more frequent during the winter season (Skeie and Grønås, 2000; Grønås and Skeie, 1999; Wilhelmsen, 1985) and comprise mainly of orography-induced tip (or corner) jets and gap flows, Arctic fronts and intense cyclones called polar lows. Tip jets account for the low-level wind maxima that are generated when the atmospheric flow is driven off high topography zones along the coastal area over to the open sea. Such jets are common in areas such as Cape Farewell along the southern tip of Greenland, the Denmark strait between Greenland and Iceland (Moore and Renfrew, 2005), the southern tip of Spitsbergen (Skeie and Grønås, 2000) and coastal Norway (Barstad and Grønås, 2005, 2006), to name a few. Gap flows refer to the strong near-surface winds that form between narrow gaps in isolated moutains when a stratified airstream flows over them (Gaberšek and Durran, 2004).

In the vicinity of the Arctic ice-edge, shallow but sharp baroclinic zones often develop during the outbreak of cold and stable Arctic air from the ice-cap over to the relatively warm open sea. Such zones are termed as Arctic fronts and are characterised by strong low-level winds (Grønås and Skeie, 1999). Generation of severe ocean waves are highly likely due to the strong surface winds connected to the Arctic fronts. A number of the accidents that took place in the Nordic Seas so far are believed to be caused by Arctic fronts only. One example is that of Gaul, a British trawler that drowned in the vicinity of Bjørnøya in 1974 with 36 men on board, as suggested by the studies of Norhagen (2004). It used to be a difficult task earlier to simulate Arctic fronts and understand the interconnections between the frontal circulation and other synoptic scale circulation systems in the Nordic Seas region. This task has become more tractable in recent times with the application of very high resolution numerical models and an increased network of observing systems.

Often, short wave troughs develop at upper-levels in the proximity of synoptic scale cyclones that propagate in a northeastward direction over the Nordic Seas during winter. When these upper-level troughs move over pre-existing lower-level baroclinic zones or Arctic fronts, they trigger low pressure systems near the frontal zones as per the baroclinic instability theory (Holton, 2004). The low pressure systems may intensify further leading to the formation of intense mesoscale cyclones, termed most commonly as polar lows. Polar lows are associated with conditions such as severe snowfall, wind speeds of hurricane force and cause devastating effects around the area where they develop and move. The earliest references to these storms were made by Sumner (1950) and Dannevig (1954) who considered static instability through deep atmospheric layers to be responsible for the development of such systems. Imagery provided by the weather satellites indicate that a wide spectrum of polar lows exists over the Nordic Seas, which mainly includes stratified comma clouds, spiraliform clouds, merry-go-round clouds, and instant occlusion clouds (Rasmussen and Turner, 2003; pp 17). In some cases, intense polar lows with a clear eye at the center, which is a common structure of tropical hurricanes, have also been reported (e.g., Nordeng and Rasmussen, 1992). In order to explain the manifestation of polar lows in such a variety of structures, a number of theories have been proposed of which the important ones are the baroclinic instability mechanism (e.g., Harrold and Browning, 1969; Mansfield, 1974) and the convective instability of the second kind (CISK) mechanism (e.g., Rasmussen, 1977, 1979; Økland, 1977). The literature regarding polar lows is affluent with attempts to understand

the dynamics of these systems and their sensitivity to various background conditions using different approaches. However, certain gaps still exist regarding different aspects involved in the genesis and growth of polar lows over the Nordic Seas.

Given the disastrous impacts of the severe weather events over the Nordic Seas, it becomes desirable to improvise the present understanding about the dynamics and other features of such phenomena and provide reliable forecasts to the coastal community. Extensive field campaigns using advanced observational instruments are being carried out over the Nordic Seas in order to record quality observations of the extreme cases so that these observations can be incorporated into high-resolution numerical models and the simulations be improved. The IPY-THORPEX field experiments carried out at Andøya in Northern Norway during February−March 2008 was one such campaign aimed at recording the extreme weather conditions over the Nordic Seas (Barstad et al. 2008). Measurements of a gap flow, an Arctic front, a polar low and several other events were collected during the campaign using dropsonde, wind lidar and water vapour lidar sensors aboard the DLR-FALCON research aircraft (Kristjansson et al., 2010).

The present thesis is a collection of three scientific papers, the goal of which were to investigate some of the key events recorded during the IPY-THORPEX field campaign and understand the sensitivity of these events to various background conditions. Paper-I presents a model- and observation-based study of an event of gap flow which occurred along the Hinlopen strait in the Svalbard archipelago. Paper-II describes a case study of a polar low with focus on its sensitivity to the ice-cover and sea-surface temperature. The sensitivity of polar lows to the scale of the upper-level short wave troughs, and parameters like static stability and baroclinicity is investigated in paper-III through an idealised approach. The next chapter provides a brief overview of various adverse weather conditions, their characteristics and underlying physical mechanisms, and major breakthroughs achieved in the history of the research related to these conditions.

Chapter 2

Background

2.1 Synoptic conditions favourable for extreme mesoscale features

Extra-tropical synoptic scale cyclones propagating over the Nordic Seas mostly during the winter season are the basic large-scale circulation systems that cause the formation of the mesoscale extremes over the region (Rasmussen and Turner, 2003). Such systems generate large-scale cross-mountain flows, giving rise to strong downslope winds (tip jets or coastal jets) and wind maxima along the channel between two mountain barriers (gap winds) (e.g. Grønås and Sandvik, 1999; Moore and Renfrew, 2005). The synoptic cyclones often cause deep outbreak of cold, stable and dry Arctic airmass over to the warm, open sea regions of the Nordic Seas. The leading edge of such Arctic air outbreaks manifests as a sharp frontal zone called 'Arctic front', which is associated with low-level wind maxima, over the sea. Mesoscale polar lows are highly likely to develop under such conditions.

2.2 Orography-forced wind extremes

The orographical structures that bound the Nordic Seas induce small-scale modifications into the prevailing large-scale flow and cause highly localised wind speed extremes. Such events comprise of, for example, the barrier winds along the eastern coast of Greenland near the Denmark strait, the left-side jet off the west coast of Norway, the northeasterly jet extending from the southern tip of Spitsbergen, and the gap winds and wake flows in Svalbard archipelago.

The dynamics of orography-induced mesoscale structures depends on a non-dimensional mountain height ($\hat{h}$) given by $\hat{h} = NH/U$ (Smith, 1989a). Here, N refers to the Brunt-Väisälä frequency, H refers to the mountain height and U to the upstream wind velocity. Smith (1989a) suggested three flow regimes past an idealised three-dimensional mountain on the basis of the dynamical mountain height $\hat{h}$. The first flow regime occurs for a mountain with a low dynamical height (i.e., a small $\hat{h}$) and is characterised by a slight deflection of the flow around and above the mountain with weak gravity wave activity. The other two regimes are characterised by the formation of stagnation points at different altitudes depending on the value of the dynamical mountain height $\hat{h}$. For a broad and intermediate mountain ($\hat{h}$ around unity), the stagnation point

forms at a certain altitude at the leeward slope of the mountain and wave-breaking is expected at this point (Smith, 1989a). On the other hand, for a narrow and tall mountain, the stagnation typically occurs upstream of the mountain next to the ground resulting in flow splitting around the mountain. For a critical value of $\hat{h}$ (~ 1.3), it is understood that both the stagnation points tend to form.

Smolarkiewicz and Rotunno (1989) found that the windward stagnation case could cause the formation of wakes with weaker winds behind the mountain barrier. The simulations of Smolarkiewicz and Rotunno showed the formation of two counter-rotating vortices at the mountain edges on the leeward side as the upstream flow splits and moves around the barrier. They attributed the vorticity formation to the baroclinicity produced by the tilting of the isentropes when flow passes around the mountain. Schär and Smith (1993) suggested that the dissipation, which takes place as the flow goes through a hydraulic jump, is another candidate for the generation of vorticity. The vorticity thus produced on the lee side may cause strong downslope winds.

In addition to strong downslope winds and wakes, orography-induced severe mesoscale events also include gap winds that develop along a gap between two isolated mountain ridges. Idealised simulations by Zängl (2002) indicate that strong gap winds develop as a response to mesoscale pressure gradients, between the entrance and exit regions of the gap, generated due to a large-scale cross-barrier flow. Gaberšek and Durran (2004), through their idealised simulations, found that the percentage of a flow passing through a gap is relatively independent of $\hat{h}$ in contrast to the strong dependence of flow-over-the-ridge and flow-around-the-ridge on $\hat{h}$.

2.2.1 Barrier winds along the Denmark strait

Barrier winds occur when cold and stably stratified air is driven towards a topographical barrier by the prevailing large-scale circulation (King and Turner, 1997). The area between southeast Greenland and Iceland, referred to as the Denmark strait, happens to be the area where a major storm track lies (Hoskins and Hodges, 2002). The cyclonic circulation associated with the passage of cyclones along this storm track often drives the wind along the Denmark strait from its northern to southern extent. The presence of west coast of Iceland and southeast coast of Greenland on either side of the strait causes the wind speed to increase locally to extreme values, resulting in the formation of the barrier flow. Moore and Renfrew (2005) have formed a climatology of the barrier winds, alongwith that of the tip jets off the southern tip of Greenland (not discussed in this thesis since this area lies outside the Nordic Seas boundary), on the basis of high resolution QuickSCAT dataset. They noticed that maximum wind speed associated with such events can reach as high as 50 ms^{-1} and they occurred frequently during the winter months. They also suggested that the barrier flows and tip jet events could have high impacts on the wind driven circulation of the East Greenland current and cyclonic gyres.

Aircraft observations of a barrier flow event were recorded during the Greenland Flow Distortion Experiment (GFDex; Renfrew et al., 2008), conducted over the southeast coast of Greenland between February and March 2007. The barrier flow had formed over the Denmark strait as a low pressure system to the north of Iceland channelled a northeasterly flow into the strait. A mesoscale cyclone which was centered near Iceland extended the channelling effect to the south of the Denmark strait. The

barrier winds were further strengthened by a synoptic scale cyclone located over the Irminger sea. The dropsonde observations along the Denmark strait indicated that the wind speed had increased from ~ 15 ms^{-1} to ~ 40 ms^{-1} between the entrance and exit regions of the strait (Petersen et al., 2009). A sharp temperature gradient capped the barrier jet below the mountain summit. Numerical simulations of the same event carried out by Petersen et al. (2009) suggest that the Greenland barrier jets have a significant ageostrophic component and are controlled mostly by the synoptic scale flow.

2.2.2 Mesoscale wind maxima off coastal Norway

The landscape of the coastal belt of Norway is made up of a range of mountains with steep valleys, plateaus, narrow and long fjords. When the large-scale flow, which is often southerly to southwesterly, prevails over such a landscape, adverse mesoscale events such as downslope winds and gap flows are likely to arise. Due to the lack of sufficient three-dimensional observations of the structure of such small-scale jets, an understanding of their dynamical features has been meagre.

Barstad and Grønås (2005, 2006) studied the ideal behaviour of such events and their sensitivity to the direction and speed of the large-scale flow by using the PSU/NCAR MM5 model. These findings indicated that the wind speed associated with the jet attains maximum values when the prevailing wind direction is southwesterly and tends to be minimum when the wind is southerly. Barstad and Grønås suggest that differential friction, rotation, the scale of the underlying mountain ranges, dissipation and wave breaking are crucial factors that control the dynamics of the wind jets off the Norwegian coast.

In October 1996, a synoptic scale cyclone was seen over northern Norway and was associated with large-scale southwesterly flow impinging on the coastal mountain ranges of northern Norway (Grønås and Sandvik, 1999). With the help of a high resolution numerical model, Grønås and Sandvik (1999) simulated the mesoscale modifications invoked by steep orographical features of the coastal northern Norway onto the large-scale southwesterly flow. The simulations showed the formation of a re-circulation with return currents on the lee side of the steep mountains. It was found that the re-circulation caused strong turbulence on the lee side which led to the formation of wind gusts of over 50 ms^{-1}. These wind gusts caused significant damage to the power pylons situated in the area.

2.2.3 Mesoscale structures around Svalbard archipelago

The geography of Svalbard archipelago is such that it contains a number of isolated mountain ridges and fjords. Spitsbergen and Nordaustlandet are the two main islands in this archipelago, with Spitsbergen having the tallest mountain peak with a height of ~ 1717 m. The easterly flow impinging on the terrain features of Svalbard archipelago during the winter months gives rise to several small-scale phenomena including wakes, gap flows and jets. Of all the jets, maximum wind speed happens to be associated with the northeasterly jet extending downstream from the southern tip of Spitsbergen (Skeie and Grønås, 2000). Skeie and Grønås investigated a case of such a feature generated by strongly stratified easterly flow crossing the Svalbard archipelago by using a numerical model, and found that the strongest velocity associated with the jet was of the order

$\sim 35-40$ ms^{-1}. They suggested that the asymmetrical distribution of the topography and planetary rotation play a crucial role in the formation of jets and wakes near the coastal line of Svalbard archipelago.

The Spitsbergen and Nordaustlandet islands are separated by a long, southeast-to-northwest running fjord called the Hinlopen strait. Strong gap flows often develop at the exit region of this strait due to the local topographical distribution and, to some extent, to the channeling effect of the strait on the upstream flow (Sandvik and Furevik, 2002). Gap winds are usually associated with cloud banners emanating from the tips of the mountain ridges in the northern lee of Spitsbergen and Nordaustlandet. On either side of the jet core corresponding to gap winds, i.e., below the cloud banners, there exists a wake area with weak return currents. Paper-I of this thesis shows that the formation of the cloud banners is more favourable under reversed wind shear conditions and their maintenance depends on the buoyancy and moisture availability from the warm ocean surface downstream of the lee.

2.3 Arctic fronts

During the winter season, synoptic scale low pressure systems propagating in a north-east direction over the Nordic Seas draw the cold, stable Arctic airmass over to the Nordic Seas. This phenomenon, commonly referred to as Marine Cold Air Outbreak (MCAO; e.g. Kolstad and Bracegirdle, 2008), forms a shallow ($\sim 1-3$ km extending from the surface) and sharp zone separating the Arctic airmass from the warm maritime airmass over the open sea. This zone is termed as 'Arctic front (AF)' and is characterised by sharp cross-gradients of temperature, wind and density. AFs form on the poleward side of the main polar front, some distance away from the Arctic ice-edge. Note that sharp, shallow fronts exist also along the ice-edge and are often termed as 'ice-edge fronts'. In some literature, the terminology 'Arctic fronts' has also been used to denote these ice-edge fronts. Ice-edge fronts owe their existence to differential heating of the boundary layer over open water and the adjacent ice-cover (Grønås and Skeie, 1999; Businger and Reed, 1989a). In general, AFs are associated with severe winds and heavy precipitation and have caused several accidents in the Nordic Seas over the years. Formation of an AF is a potential situation for the development of intense mesoscale storms called polar lows, provided the upper-level conditions meet certain requirements.

2.3.1 Important characteristics of Arctic fronts

Figure 2.1 shows a NOAA-4 infra-red image of an AF formed over the Norwegian sea on 29 February 2008. Dense cloud streets behind the AF indicate the cold air advection from the ice-cap. The strongly stratified cold airmass caps a neutrally/unstably stratified boundary layer over the sea behind the AF. This is clearly shown in Figure 2.2 which portrays a vertical slice taken across the AF indicated by Figure 2.1. The neutral stratification of the boundary layer is due to the strong air-sea interaction triggered during the advection of the cold airmass from the ice-cover. A low-level northeasterly jet with wind speed reaching 20 ms^{-1} is discernible over the top of the capping inversion. Such a low-level jet is an important feature of AFs and it is this jet that potentially

leads to dangerous situations in the vicinity of AFs.

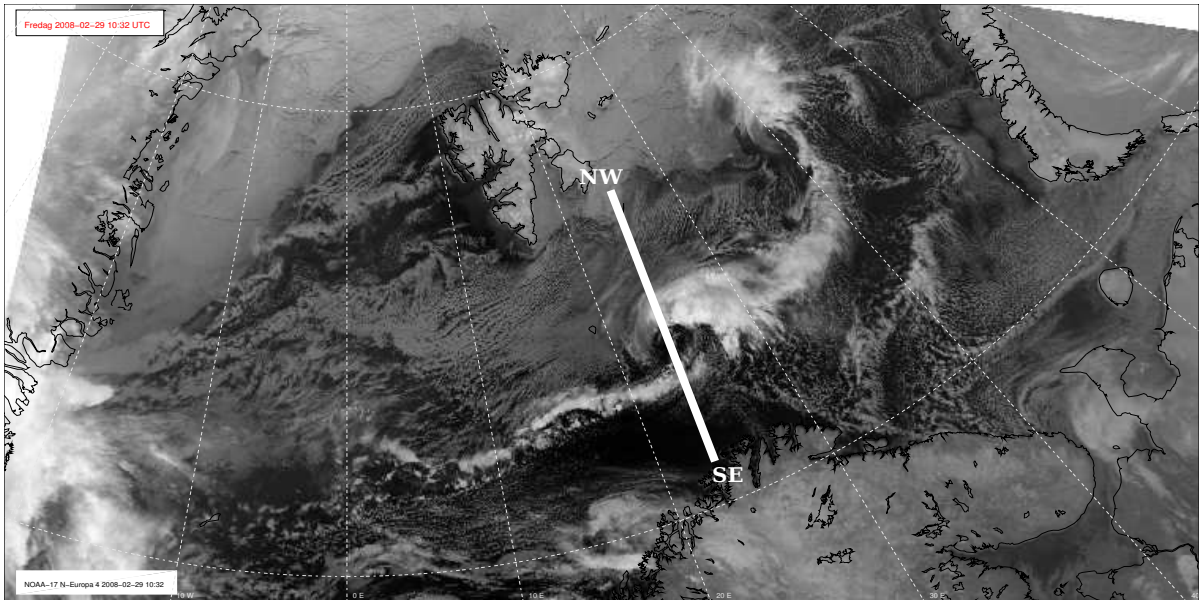

Figure 2.1: *Snapshot of an Arctic front that formed over the Norwegian sea at 1200 UTC, 29 February 2008.*

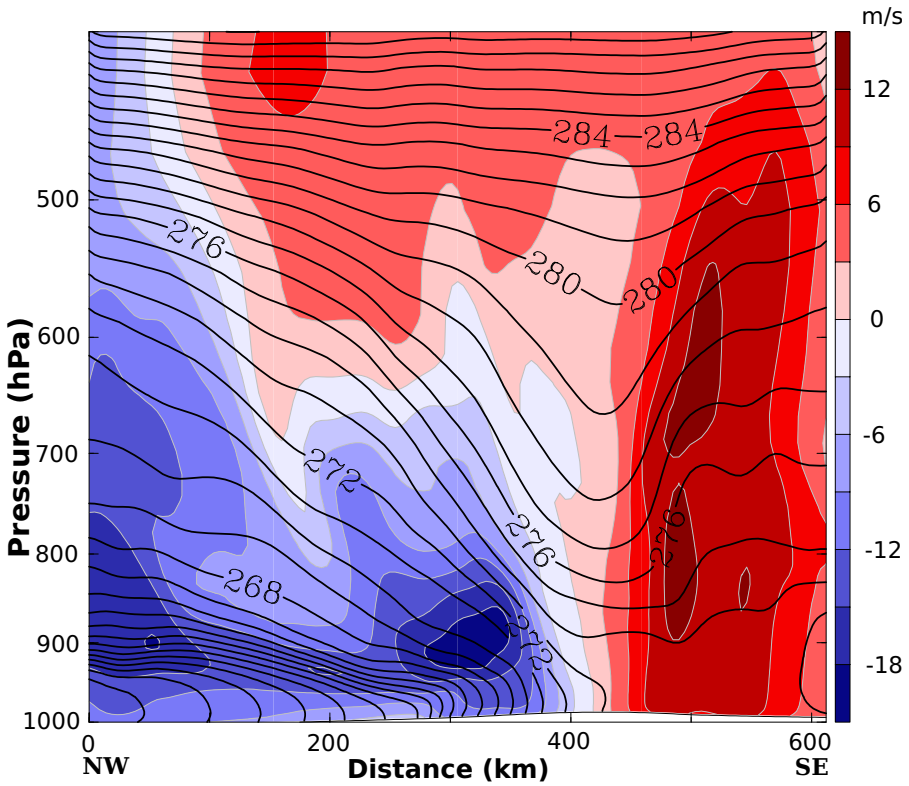

Figure 2.2: *A vertical cross section of the AF shown in Figure 2.1. This plot is taken from paper-II.*

Similar structures have been identified in several investigations of the cases with AF developments. For instance, the Arctic Cyclone Expedition carried out in 1984

recorded an AF near the Spitsbergen ice-edge (Shapiro et al., 1989) which was later simulated by Thompson and Burk (1991). These observational and numerical studies reported a low-level jet along the front as the one shown in Figure 2.2. Økland (1998) studied another case in which an unexpected increase of northeasterly winds to hurricane-force took a coast guard ship near the Bear Island by surprise. He suggested that a possible reason for such an increase in the wind speed could be the strengthening in the magnitude of the upward heat fluxes as a result of the cold air outbreak from the ice-cap. Grønås and Skeie (1999) simulated Økland's case and showed that the reported strengthening of the wind speed could also be attributed to an interaction of the easterly low-level jet corresponding to the cold front (leading edge of the outbreak) and the easterly flow in front of a warm occlusion approaching the cold front from the south. They also pointed out that this AF was characterised by reverse-shear conditions, wherein the lower-level thermal wind blows in an opposite direction to that of the mean flow.

2.3.2 Sensitivity of Arctic fronts to background conditions

The general theory of frontogenesis is based on Sawer-Eliassen equation and semi-geostrophic dynamics (e.g., Hoskins and Bretherton, 1972; Thorpe and Emanuel, 1985; Holton, 2004, pp 274). As per the theory, major frontogenetic processes (i.e., the processes that generate fronts) are either or a combination of a deformation in the mean (large-scale) flow and diabatic heating. From the perspective of AFs, one or more of the above processes become active during a MCAO, thereby forcing an AF to form. For example, the advection of cold air from the Arctic over to relatively warm open sea basin deforms the surface pressure distribution in such a way that strong pressure gradients are created along the direction of the flow. Diabatic heating can be perceived as the release of strong sensible and latent heat fluxes from the warm ocean towards the overlying cold airmass and also the condensation heating along the frontal zones. Strong sensible heating of the cold air over the water is considered to be the major cause of the strong winds observed at AFs (Økland, 1998).

To understand the sensitivity of AFs to conditions such as diabatic heating and the inversion over the ice-cover, simulations of an AF were carried out in an ideal baroclinic channel. The base state temperature profile used for the simulation is similar to the profile documented by Grønås and Skeie (1999), which corresponds to a case of AF formation near Bear Island. The profile has a neutral boundary layer below ~ 900 hPa and is capped by an inversion layer of depth ~ 700 m. Three sensitivity experiments were performed apart from the control (CTL) experiment, the details of which are given in Table-2.1. In all the simulations, the baroclinic channel was initialised by prescribing skin temperature as 280 K in the southern half of the channel. In the northern half, the skin temperature was kept unperturbed at ~ 263 K. The motive behind prescribing a relatively high temperature in the southern half was to obtain a strong temperature gradient across the front.

Figure 2.3 shows a south-north vertical cross section of the baroclinic channel at 0 h and at 18 h prognoses in the CTL experiment. The model forecast shows the formation of a shallow, convective boundary layer in the southern half of the channel as a response to the warm surface. A cold front develops in the channel with the frontal band tilting vertically from the surface up to ~ 900 hPa towards the colder northern half of the

Exp.	Type	Inversion over the ice-cover	Condensational heating	Surface heat fluxes
1	CTL	Normal	Yes	Yes
2	INV	Strong	Yes	Yes
3	NCH	Normal	No	Yes
4	NFX	Normal	Yes	No

Table 2.1: *List of idealised experiments.*

channel as indicated by the slanting isentropes. The cross frontal scale at the surface is nearly 100 km with a temperature contrast of about 7 K across this distance. The front appears to be shallow with the associated cross-frontal circulation being confined below ~ 800 hPa. The maximum strength of this vertical motion is around 5 ms^{-1}. An easterly low-level jet with a maximum wind speed of ~ 10 ms^{-1} develops at the boundary of the cold front as a baroclinic response to the horizontal temperature gradient. The ideal representation of an AF shown in Figure 2.3b looks to be consistent with real cases of AFs. (e.g., Figure 2.2).

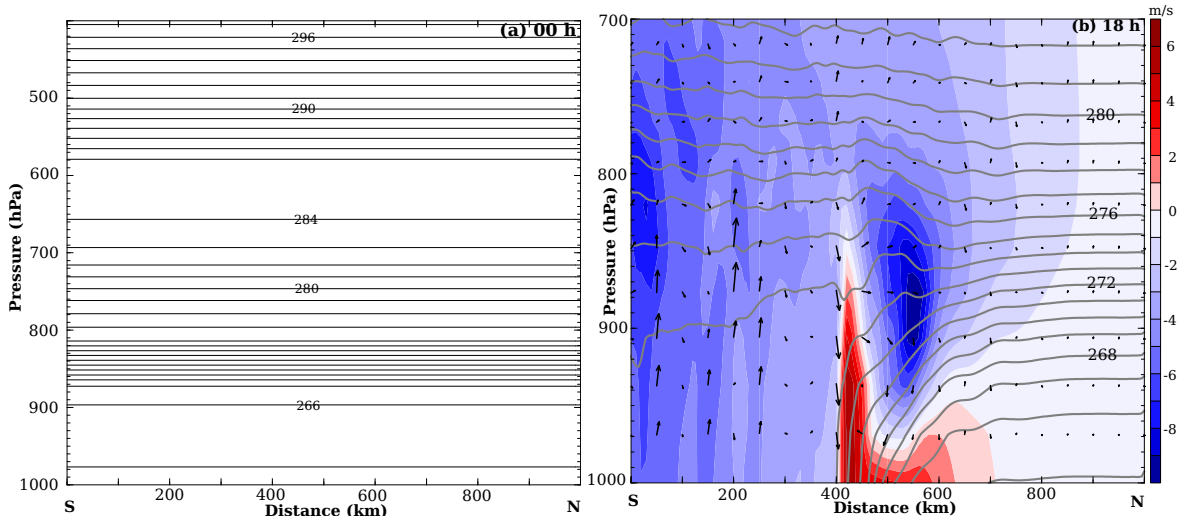

Figure 2.3: *A south-north vertical cross section of the ideal baroclinic channel for the CTL simulation. (a) The initial condition. Black contours represent isentropes at 1 K interval, and (b) 18 h forecast. Light gray contours represent isentropes at 1 K interval, coloured contours represent wind speed normal to the cross section. Negative values indicate a motion into the plane of the cross section and positive values indicate the opposite. Black arrows represent ageostrophic circulation vectors.*

In the INV simulation, the inversion layer of the base state profile was extended down to the surface which results in a deeper and stronger inversion layer with respect to that in the CTL simulation. Similar strong inversions are common in the Arctic during winter (e.g., Grønås and Skeie, 1999; Serreze et al., 1992). The results of the experiment INV are shown in Figure 2.4a. Apparently, the strength of the cross-frontal circulation increases to ~ 13 cms^{-1} in this experiment from ~ 5 cms^{-1} in the CTL run.

Also, the maximum wind speed associated with the easterly low-level jet appears to have increased in the INV run to ~ 11 ms^{-1} from ~ 10 ms^{-1} in the CTL run. Another notable change is the strengthening of the vertical circulation in the convective boundary layer in the southern half of the channel. Such a strengthening of the features associated with the AF and the vertical mixing in the boundary layer could be attributed to a sharper low-level temperature gradient produced by the stronger inversion over the ice-cover.

Through the experiments NCH and NFX, the sensitivity of the AF to diabatic heating was studied. The condensation heating was switched off in the NCH run whereas the surface fluxes of sensible and latent heat were switched off in the NFX run. This methodology also aids in the assessment of the relative influence of condensation heating and surface heat fluxes on the cross-frontal circulation associated with the AF. The results of the experiments NCH and NFX are shown in Figures 2.4b and c respectively. The removal of condensation heating seems to have nullified the vertical mixing in the shallow boundary layer in the southern half of the channel adjacent to the AF. However, it is interesting to note that the cross-frontal circulation associated with the AF as well as the strength of the easterly jet at the AF remain unchanged in the NCH run when compared with that of the CTL simulation. Thus it looks as if condensation heating may not be that important as far as low-level AFs are concerned. Nevertheless, condensation heating might be crucial when it comes to the interactions of shallow low-level AFs and upper-level disturbances that lead to cyclogenesis.

In contrast to the NCH experiment, the removal of the surface heat fluxes in the NFX experiment acts to reduce the strength of the AF and the vertical mixing in the neutral boundary layer substantially (Figure 2.4c). The depth of the boundary layer too has reduced roughly by a factor of two in comparison with that of the CTL simulation. These results highlight the importance of surface heating in frontogenesis, and are in accordance with the findings of Moore (1991) and Økland (1998) who investigated real cases with an analytical approach. In addition to what the earlier results based on real cases have shown, the idealistic results presented here also reflect the striking difference between the impacts of condensation heating and surface heating on the features related to AFs.

2.4 Polar lows

Polar lows refer to a wide range of small-scale cyclonic systems that develop at high latitudes in both the hemispheres mainly during winter. Major part of the polar low research has been focusing on the systems that develop in the Northern hemisphere due to a better observational coverage when compared to that in the Southern hemisphere (for a detailed overview of the polar low research in both the hemispheres, see Rasmussen and Turner, 2003). Polar orbiting weather satellites have shown the existence of a number of types of polar lows over the Nordic Seas with distinguishable cloud structures associated with them. According to Rasmussen and Turner (2003), Kerry Emanuel first introduced the term 'polar low spectrum' (at the International Conference on Polar Lows in Oslo, 1986) which includes all the polar low types. Individual polar lows in this spectrum possess different structural and dynamical features with respect to one another. Considering this, it has been a difficult task to define these systems unambigu-

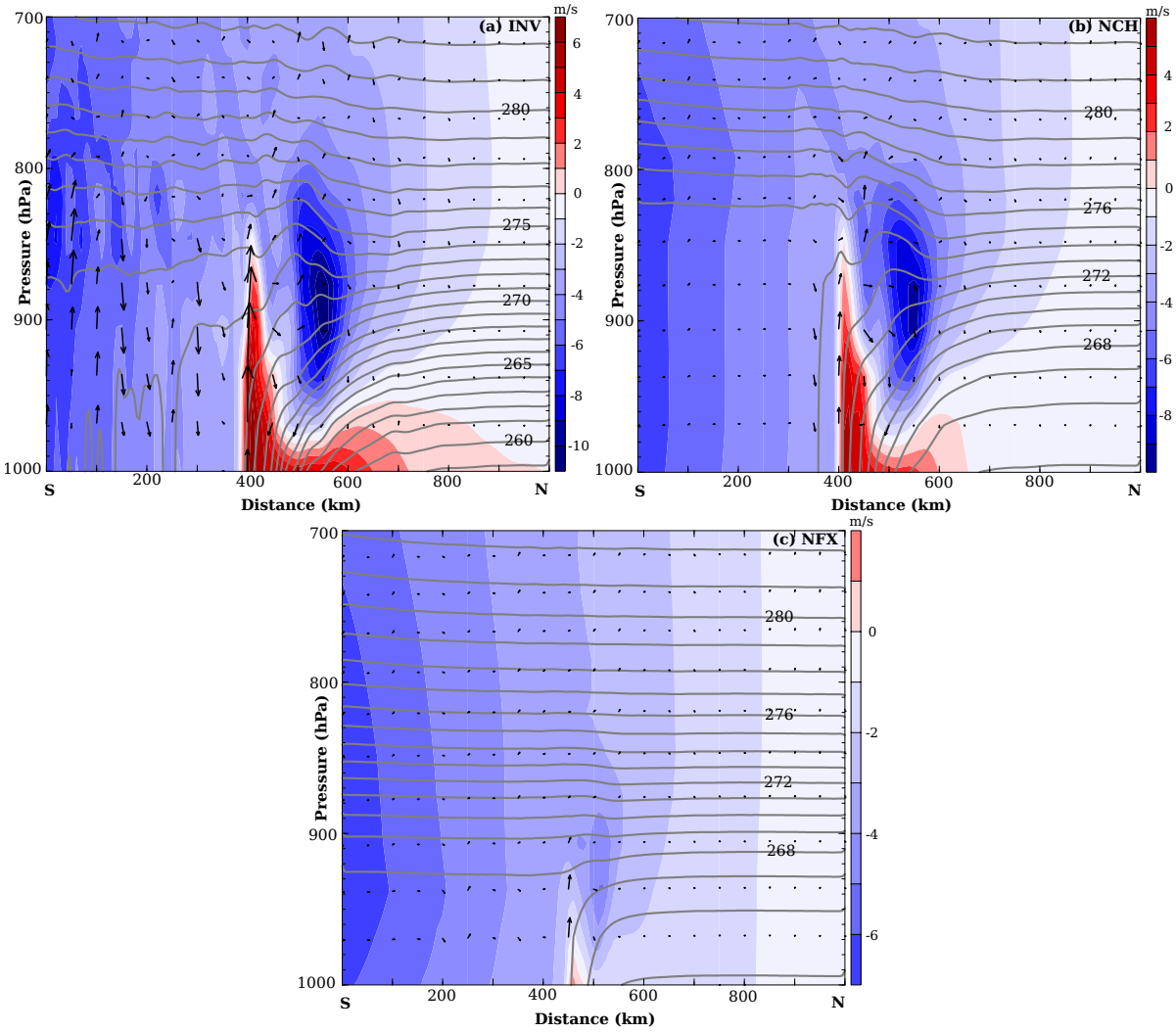

Figure 2.4: *South-north vertical cross section of the ideal baroclinic channel for different sensitivity simulations (see Table-2.1 for experimental details). Contour details are as in Figure 2.3b. All the three plots are valid at 18 h prognosis.*

ously. A general definition which moreorless covers the whole spectrum of polar lows was suggested by Rasmussen and Turner (2003), and is given by;

"A polar low is a small, but fairly intense maritime cyclone that forms poleward of the main baroclinic zone (the polar front or other major baroclinic zones). The horizontal scale of the polar low is approximately between 200 and 1000 kilometres and surface winds near or above gale force (above 15 ms^{-1})."

Data provided by polar orbiting weather satellites have played a crucial role in the research of polar lows. These satellite provide useful information regarding the location of polar lows, their composition, structure, cloud-top temperature, cloud liquid water content and integrated water vapour (Rasmussen and Turner, 2003). A couple of types of polar lows, distinguishable in their structure, have been identified through the imagery of the cloud distribution taken from these satellites. The most common types observed over the Nordic Seas are polar lows with stratified comma clouds and that with convective spirali-form clouds (Carleton, 1995). An example each for these two types are shown in Figures 2.5 and 2.6. Many observational and numerical experiments

have been carried out to understand the driving mechanisms that give rise to different structural manifestations of polar lows.

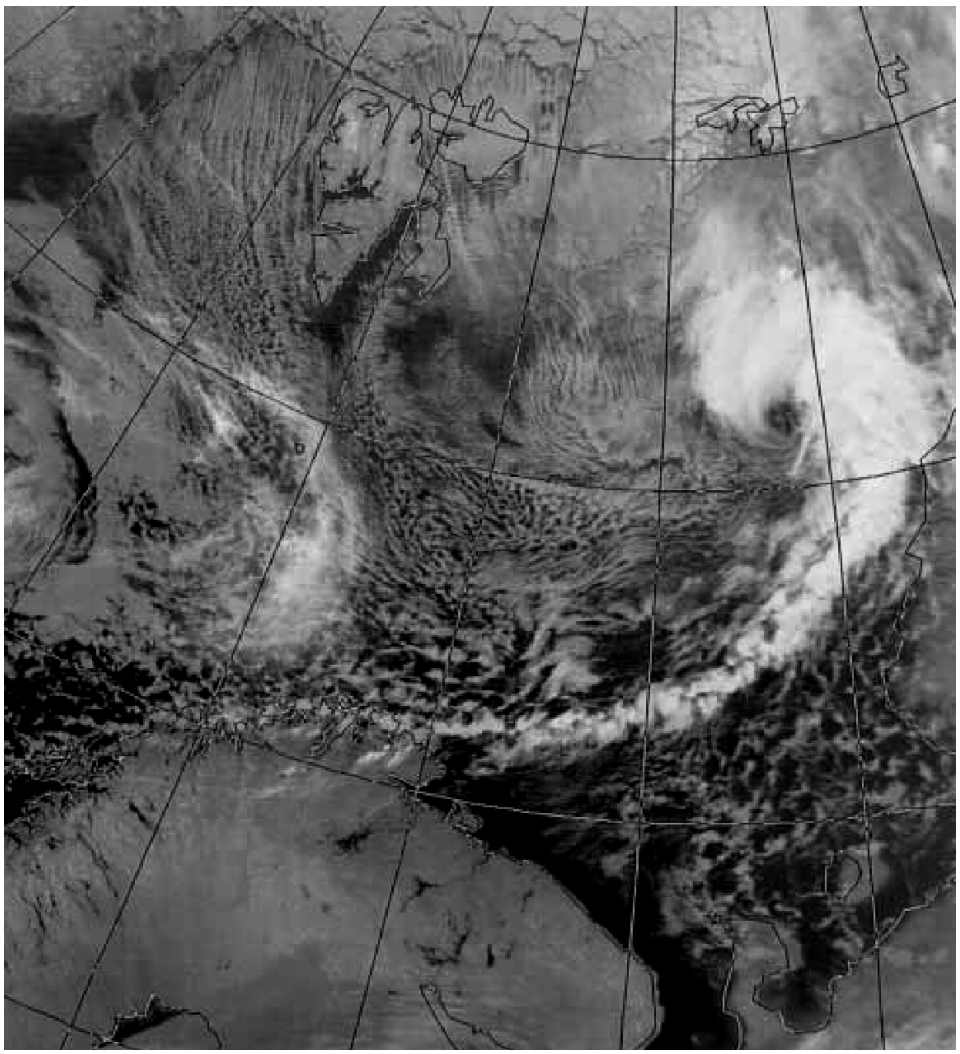

Figure 2.5: *Example of a comma-shaped polar low over the Barents sea. The image was taken by NOAA-11 at 1244 GMT, 20 October 1992. (Image courtesy: The NERC Satellite Receiving Station, University of Dundee.)*

2.4.1 Theory

A couple of theories have been proposed to explain the genesis and growth of polar lows of various types. Out of these, the major theoretical explanations that account for most of the types happen to be baroclinic instability and conditional instability of the second kind (CISK). Barotropic instability too has been considered but polar lows with this as a driving mechanism are found to develop rarely over the Nordic Seas (Rasmussen and Turner, 2003). Investigations over the years suggest that polar lows may either develop as pure baroclinic systems or pure convective systems (that develop through CISK). Many studies have also indicated the possibilities of polar lows being influenced by both the mechanisms. It should be noted that baroclinic developments always involve some convection but it is relatively weaker than that occurs in pure

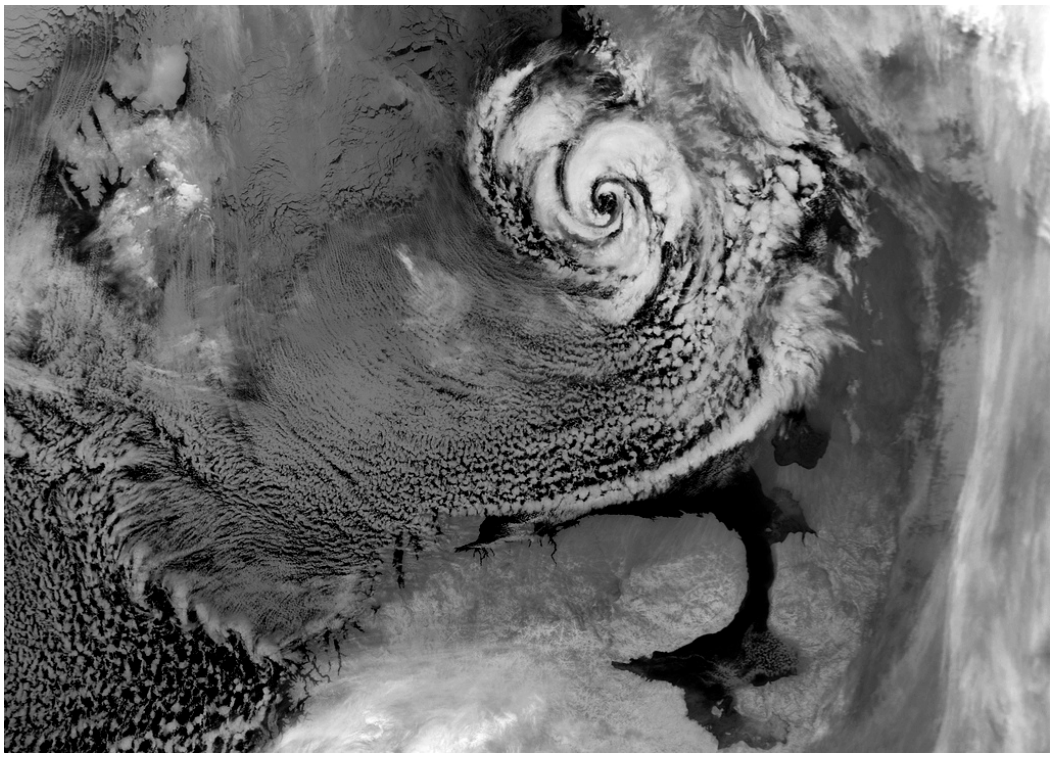

Figure 2.6: *A satellite image of a spirali-form polar low over the Barents sea valid at 0204 UTC, 20 December 2002. (Image courtesy: The NERC Satellite Receiving Station, University of Dundee.)*

convective developments. Hence, pure baroclinic polar lows are generally weaker than pure convective systems.

Baroclinic instability

Theory of baroclinic instability was basically formulated to explain the development of synoptic scale cyclones that originate over mid-latitudes near the deep baroclinic zone associated with the polar front (Charney, 1947; Eady, 1949). Essentially, baroclinic instability is the process in which small-scale fluctuations in the atmosphere convert the potential energy available in the baroclinic zones to kinetic energy and amplify exponentially. The conversion of potential energy to kinetic energy manifests through a thermally direct circulation (ascending and descending motions). In its simplest form, the theory assumes a zonally uniform flow with a rigid lid at a height H (presumably at the tropopause level), a meridional temperature gradient $\nabla\theta$, Coriolis parameter f corresponding to mid-latitudes, and static stability N. The governing equations are solved by assuming a wave-like solution to obtain an expression for the unstable waves (Eady, 1949). The scale of the unstable waves (or, Rossby radius of deformation) is proportional to NH/f and their growth is a linear function of $f\nabla\theta/N$. The fastest growing mode has a scale of ~ 4000 km which fits well with the observed value of the wavelength of the mid-latitude baroclinic waves.

On the adaptation of baroclinic instability theory to explain the development of mesoscale cyclones like polar lows, it should be noted that the latitudes where polar

lows form have a higher f than the mid-latitudes. Moreover, the value of H is reduced considerably during the outbreaks of cold and stable air over warm seas since an outbreak is generally associated with a trough at the tropopause level as per the geopotential tendency equation (Holton, 2004). An outbreak of cold air also leads to a reduction in N in the marine boundary layer due to enhanced air-sea interaction during such a situation. With these modified parameters, the scale of the resulting unstable waves becomes comparable to that of the observed polar lows.

Analysis of the development of polar lows through the framework of baroclinic instability first came probably by Harrold and Browning (1969). Through conventional dropsonde and radar measurements of a polar low, they noticed a slantwise ascent of air along a narrow tongue, which typifies the baroclinic energy conversion. In the same paper, Harrold and Browning discussed a few other polar lows that formed in the vicinity of a low-level temperature gradient and concluded that baroclinic instability can also account for the growth of polar lows in addition to the large-scale mid-latitude cyclones. This view was later supported by Mansfield (1974). Mansfield extended the observational study of Harrold and Browning with a numerical approach. Mansfield applied the normal mode baroclinic theory for the two polar lows mentioned by Harrold and Browning and showed that the growth rate, wavelength and the phase speed of the polar lows are very close to the predictions of the baroclinic theory. Duncan (1977, 1978), Reed and Duncan (1987) also justified the application of baroclinic instability theory to explain the development of polar lows in their numerical studies of various polar low cases.

An important feature of most polar lows driven by baroclinic instability is the presence of mobile, upper-tropospheric troughs above the region of cyclone development (e.g., Businger and Reed, 1989a). These troughs are usually embedded in the large-scale extra-tropical cyclones propagating northeastwards over the Nordic Seas. The troughs are associated with a secondary vorticity maxima and a corresponding positive vorticity advection (PVA) and provide an upper-level forcing for the growth of polar lows. As the cyclone develops, the features associated with the upper-level disturbance tend to propagate downwards and couple with the features associated with the surface cyclone. Rapid intensification of the polar low takes place once such a coupling is achieved (Rasmussen and Turner, 2003).

The process of a vertical coupling followed by a rapid intensification of a polar low can be better understood in an isentropic potential vorticity (PV) framework. Such an attempt was first made successfully by Hoskins et al. (1985) to diagnose the role of upper-level forcing in the growth of extra-tropical cyclones. For their study, Hoskins et al. (1985) considered the two important characteristics of PV that make it an useful diagnostic tool−the invertibility principle and the conservation of PV in an adiabatic, frictionless flow. According to the invertibility principle, it is possible to determine the distribution of wind and temperature for a particular flow once the PV associated with that flow field is known. Furthermore, a positive PV anomaly associated with the upper-level trough induces a similar anomaly at lower-levels, and a coupling between the upper-level and lower-level features is achieved during the intensification of a cyclone. For the sake of clarity, the important relations from Hoskins et al. (1985) is rewritten below.

The invertibility principle for a frictionless, adiabatic and axisymmetric flow in isen-

tropic coordinates (r, θ) is given by

$$\frac{\partial}{\partial r}\left(\frac{1}{r}\frac{\partial(r\upsilon)}{\partial r}\right)+g^{-1}\xi_\theta\frac{\partial}{\partial\theta}\left(\frac{f}{R}\frac{\partial\upsilon}{\partial\theta}\right)=\sigma\frac{\partial\xi_\theta}{\partial r} \tag{2.1}$$

where υ is the horizontal wind field and ξ_θ is the potential vorticity. r is the radial distance from the center of the vortex and θ refers to the potential temperature. g and f have their customary meaning. σ is the density in $xy\theta$ space. R is defined as

$$R(p)=\left(\frac{d\Pi(p)}{dp}\right)$$

where $\Pi(p)$ is called the Exner function and is given by

$$\Pi(p)=c_p\left(\frac{p}{p_0}\right)^{\kappa}$$

Equation (2.1) implies that a particular anomaly in the PV $\xi(r,\theta)$ induces a similar anomaly in the wind field $\upsilon(r,\theta)$ or vice-versa. The wind anomaly induced by a PV anomaly at a particular level in the atmosphere tends to decay exponentially above and below the location of the PV anomaly in order to preserve the thermal wind balance. The depth through which the wind field decreases by a factor e (the e-folding depth) is termed as *Rossby penetration depth* or simply *Rossby height*. In other words, *Rossby height* represents the vertical penetration depth of the upper-level PV anomaly. By using the hydrostatic balance, an expression for the *Rossby height D* can be obtained in physical space (for the derivation, see Rasmussen and Turner, 2003 in page 367). The expression is as given below:

$$D\approx\frac{\sqrt{f(f+\zeta_\theta)}L}{N} \tag{2.2}$$

where ζ_θ is the isentropic relative vorticity, L is the horizontal scale of the PV anomaly and N is static stability. Note that the penetration depth of an upper-level PV anomaly depends on the horizontal scale of the anomaly and the static stability.

After Hoskins et al. (1985) elaborated the application of isentropic potential vorticity in the analysis of upper-level forcing in the development of synoptic-scale cyclones, the approach has been applied to many cases of polar low developments (Sunde et al., 1994; Røsting et al., 2003; Røsting and Kristjansson, 2006). The same approach has been used in paper-II and paper-III of this thesis to analyse the growth of a polar low. An example of a vertical PV coupling, taken from paper-II, is shown in Figure 2.7 which portrays a vertical cross section through a polar low. The polar low was characterised by a strong baroclinic zone at lower-levels (the western flank in the cross-section) associated with a jet of strength ~ 30 ms^{-1}. Since a particular wind anomaly has a corresponding anomaly in PV as per the relation (2.1), there was a lower-level positive PV anomaly on the western flank of the polar low. A positive PV anomaly associated with the upper-level trough penetrated downwards and coupled with the lower-level anomaly as the polar low grew in its strength. The figure clearly illustrates this situation. Similar results have been obtained in several other case studies as well (see, for example, Sunde et al., 1994).

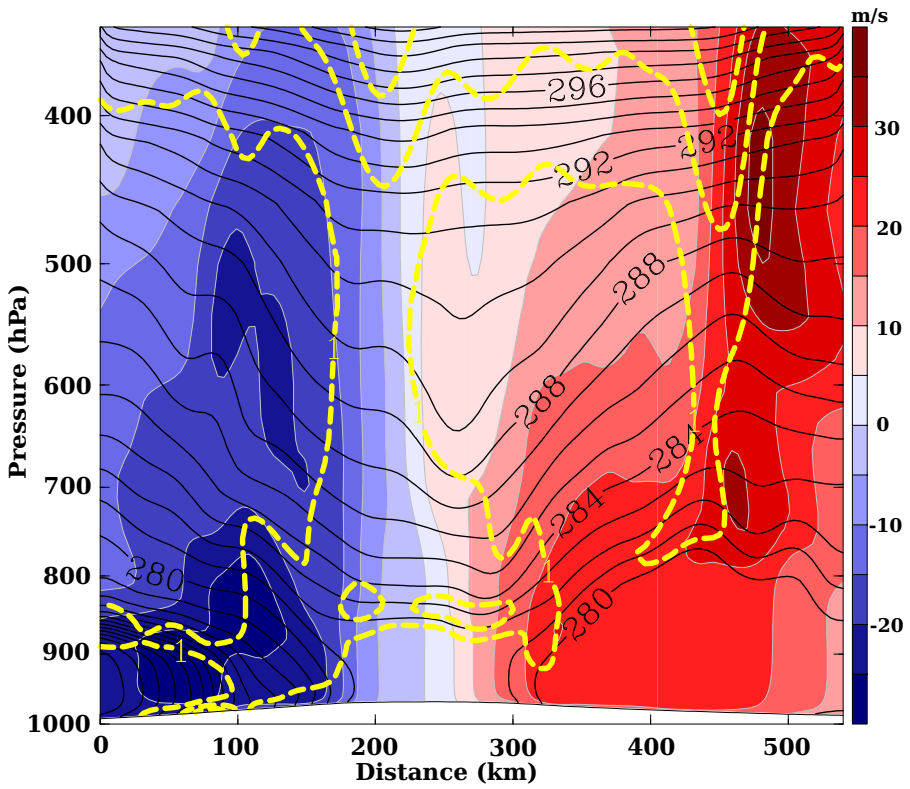

Figure 2.7: *Vertical cross section through a polar low at 1800 UTC, 3 March 2008, illustrating the vertical potential vorticity coupling. This plot is taken from paper-II. Solid, black contours represent isentropes (at 1 K interval) and thick, yellow contours represent PV (1, 2.5 and 4 PVU contours are displayed). The coloured area indicates the wind speed normal to the cross section (positive values represent the motion into the cross-section and negative contours denote the opposite).*

Conditional instability of the second kind

The theory of baroclinic instability could only explain the formation and development of polar lows characterised by comma-shaped clouds. It was not effective in explaining the origin and maintenance of the organised cumulus convection which forms convective spiraliform clouds, sometimes with a clear eye at the center. Polar lows with a spiraliform structure have been observed in numerous satellite images. Økland(1977) and Rasmussen (1977, 1979), assuming a reservoir for convective available potential energy (CAPE), used the theory of the conditional instability of the second kind (CISK) to explain the nature of the organised circulation around the vortex.

The CISK theory was initially put forward by Charney and Eliassen (1964) and Ooyama (1964) in order to describe the dynamics of tropical hurricanes. The necessary pre-requisites for CISK to favour a cyclone development are the presence of an initial disturbance or a low pressure area at lower-levels and sufficient amount of CAPE (Rasmussen and Turner, 2003; pp 394). Moisture convergence associated with the low-level disturbance leads to cumulonimbus convection in a conditionally unstable but unsaturated atmosphere. The latent heat released by the cumulus clouds creates a solenoidal field which will set-up a circulation with upper-level divergence and low-level convergence. The lower-level convergence feeds the vortex with moisture and causes an increase in the relative vorticity associated with the vortex. The increase in the relative

vorticity will strengthen the vertical velocity at the top of the Ekman layer as per the Charney-Eliassen formula (Charney and Eliassen, 1964). New convection will begin once the surface air is in this way lifted to its lifting condensation level and a positive feedback loop is initiated which will further amplify the convection and the vortex. The whole process of CISK is illustrated in Figure 2.8 in the form of a flow-chart. The loop would persist until the moisture from the surface is cut-off as the cyclone moves over land-masked area.

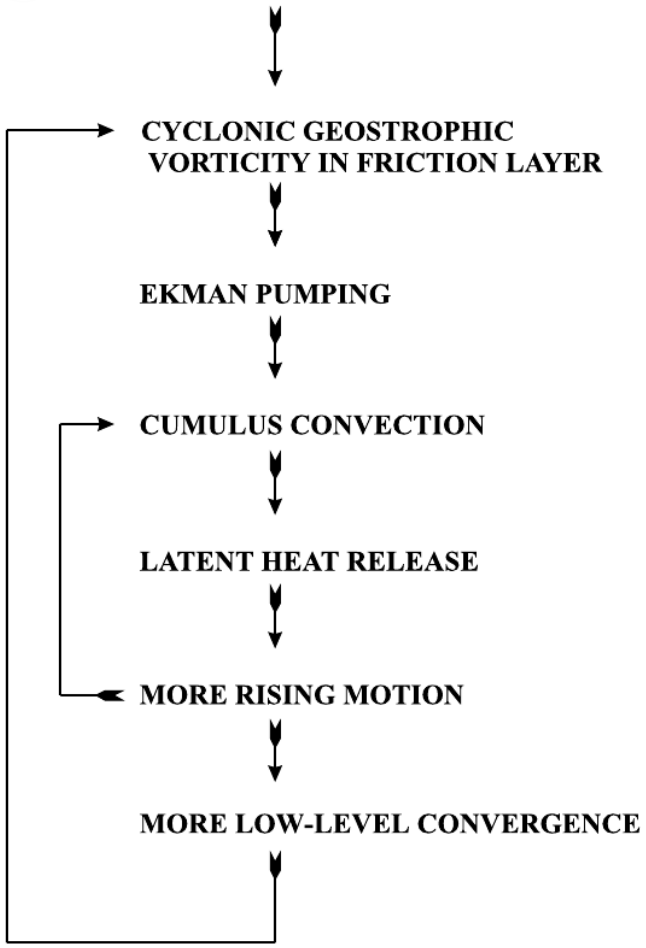

Figure 2.8: *Illustration of the CISK mechanism. Adapted from Bluestein (1993).*

The use of CISK theory to explain cyclone developments, including the tropical systems and polar lows, was challenged in a number of papers (Emanuel, 1986a; Emanuel and Rotunno, 1989). According to Emanuel and Rotunno, the tropical atmosphere is nearly neutral rather than being conditionally unstable and hence a reservoir of CAPE does not exist as was assumed by Charney, Eliassen and Ooyama. Emanuel (1986a) proposed the mechanism of air-sea interaction instability (ASII, now called Wind Induced Surface Heat Exchange or WISHE)' wherein the maintenance of the cyclonic vortex was attributed to turbulent heat transport from the ocean surface into the cyclonic vortex. However, the application of CISK to the development of polar lows was justified by Rasmussen (1979) in a case study of a polar low. He showed that the

CAPE values were as high as 1100 Jkg^{-1} during the formation of this polar low and argued that similar situations may occur at high latitudes during the polar air outbreaks that bring cold and highly stable air over to warm ocean basin, thereby triggering deep convection.

2.4.2 Classifications of polar lows

As stated by Businger and Reed (1989a), there is no widely accepted method for classifying polar lows. Apart from the two classifications based solely on the structural features viz., the comma-shaped polar lows and the spirali-form polar lows, several classifications have been made based either on the associated synoptic conditions or on the driving mechanisms (e.g., Businger and Reed, 1989a; Rasmussen and Turner, 2003). In a review paper, Businger and Reed (1989a) categorised polar lows into three types based on the distinctive synoptic conditions associated with the developments. The three types were; i) short-wave/jet-streak type, ii) Arctic-front type, and iii) cold-low type. From a physical perspective, the above categories are distinct in the degree of baroclinicity, static stability and the surface fluxes of latent and sensible heat. The short-wave/jet-streak systems are characterised by a positive potential vorticity anomaly at upper-levels, moderate baroclinicity and modest surface fluxes. On the other hand, the Arctic front systems are typified by strong surface fluxes and strong and shallow baroclinicity whereas the cold-low type polar lows are identified by weak baroclinicity, strong surface fluxes and deep convection.

Rasmussen and Turner (2003) provided a broader classification scheme which is based on the synoptic conditions and the driving physical mechanisms. Using this scheme, Rasmussen and Turner divided the polar low cases reported by Wilhelmsen (1985) into seven groups shown in Table 2.2. It should be noted that the case study by Wilhelmsen (1985) took into account only the polar low developments occurred between $1978-1982$ over the Nordic Sea area. This constraint makes this scheme valid largely for the polar lows over the Nordic Seas only. Rasmussen and Turner pointed out that since polar low developments are strongly dependent on local climatological factors, this scheme may not be applicable for other genesis areas.

All the polar low types in Table 2.2, except the 'orographic polar lows', and also the three types of Businger and Reed (1989a) could be classified either as baroclinic-driven systems or as convective-driven systems or a combination of both. As the name suggests, the 'orographic polar lows' are driven mostly by the orography-induced processes. Since the possibility of the development of this type of polar lows over the Nordic Seas is relatively low as indicated by Table 2.2, they are excluded here and the importance is given only to the rest of the types that fall into the category of baroclinic systems and/or convective systems.

Baroclinic-driven polar lows

From the polar low types in Table 2.2, reverse-shear systems, forward-shear systems and the boundary layer fronts (BLFs) can be placed in the category of baroclinic-driven polar lows. The Arctic front systems in the Businger and Reed (1989a) classification happen to be the types identical to BLFs only. Polar lows of this type mostly develop

Group	Type of polar low	Number of cases
1	Reverse-shear systems	8
2	Trough systems	5
3	Boundary-layer fronts	5
4	Cold lows (including merry-go-round systems	9
5	Comma clouds	1
6	Baroclinic wave-forward shear	2
7	Orographic polar lows	2

Table 2.2: *Polar lows found in the Wilhelmsen file. Adapted from Rasmussen and Turner (2003).*

under reverse-shear conditions (Businger and Reed, 1989a) and hence can be considered amongst the reverse-shear polar lows.

Reverse-shear conditions are typified by the lower-tropospheric thermal wind and the mean wind blowing in opposite directions to each other in contrast to the forward-shear conditions wherein the thermal wind and the mean wind blow in the same direction. In other words, while the mean wind speed decreases with height in a reverse-shear flow, it increases with height in a forward-shear flow. The main dynamical difference between the two conditions is that a positive vorticity advection (PVA) at upper-levels is required for a polar low to develop under the forward-shear conditions, but it is not a requirement for the formation of a polar low under the reverse-shear conditions (Businger and Reed, 1989a). The similarity between the two conditions is that a comma cloud develops in conjunction with the polar low development under both the conditions.

Duncan (1978) was the first one to identify a reverse-shear polar low and describe its properties. He suggested that reverse-shear conditions are highly likely to prevail between Greenland and Norway during winter due to the influence of cold East Greenland ocean current on the western flank of the flow and the relatively warmer water of the Gulf Stream on the eastern side. The cold-air outbreaks occurring over the Nordic Seas during winter potentially favour the reverse-shear conditions since the outbreaks have a northerly or northeasterly mean flow at lower-levels and a thermal wind directed towards north or northeast (due to the presence of the Greenland ice-sheet to the west).

An example of a reverse-shear polar low development is shown in Figure 2.9. A couple of investigations in the past have indicated that reverse-shear polar lows might be dominant over the Nordic Seas. The classifications made by Rasmussen and Turner (2003), which is shown in Table 2.2, indicates that out of a total of 15 baroclinic-driven polar lows occurred between 1978−1982, only two cases had developed under forward-shear conditions with the rest of the cases being of a reversed-shear nature. The dominance of reverse-shear developments has also been justified by a number of investigations (Grønås et al., 1987a; Rabbe, 1987).

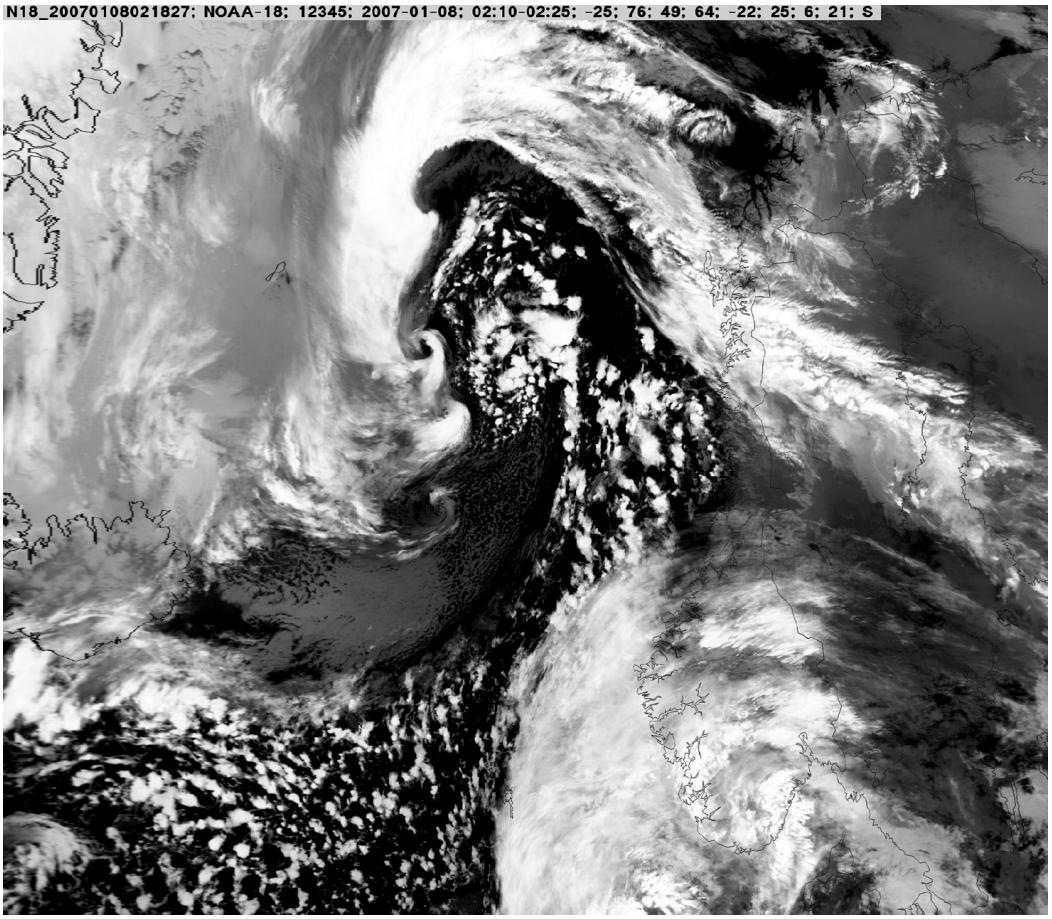

Figure 2.9: *Example of a wave-train of reverse-sheared polar lows over the Norwegian sea near Jan Mayen on 8 February 2007. Adapted from Kolstad (2007, PhD thesis).*

Convective-driven polar lows

The classification 'cold lows' in Table 2.2 falls into the category of convective-driven polar lows. Note that this type is also one of the three classifications made by Businger and Reed (1989a). The main forcing mechanism of convective-driven polar lows is CISK (see section 2.4.1). These polar lows are characterised by convective spiraliform cloud signatures, sometimes with a clear eye at the center, indicating deep, organised convection (Rasmussen and Turner, 2003). Figure 2.6 is an example for convective-driven polar lows.

Convective-driven polar lows usually develop within the inner cores of large-scale baroclinic wave occlusions or upper-level cold core vortices without any obvious influence from upper-level short waves or low-level frontal features (Businger and Reed, 1989a). As evident from Table 2.2, this type of polar lows constitutes the largest of all the groups. These polar lows tend to form when the upper-level cold core vortices move out over a warm sea basin from the ice-cover (Rasmussen and Turner, 2003). Such a process triggers deep convection in the cold air masses which leads to a conditionally unstable lapse rate in the troposphere, thereby favouring the CISK mechanism as explained in section 2.4.1.

Polar lows of both baroclinic and convective nature

Polar lows of the type 'trough systems' and 'comma clouds' (from Table 2.2) and the 'short-wave/jet-streak type' (from the Businger and Reed classification) can be grouped in this particular category since these types are influenced by both baroclinic and convective processes. These polar lows are triggered by upper-level short-wave troughs through baroclinic instability, when such troughs advect over lower-level baroclinic zones. A lower-level baroclinic zone over the Nordic Seas usually marks an east-west oriented surface trough axis of a pre-existing synoptic scale cyclone and is associated with large values of vorticity (Rasmussen and Turner, 2003). The local vorticity maximum associated with the upper-level short-wave trough interacts with the low-level vorticity through a spin-up effect (or a vertical coupling. See section 2.4.1), leading to the genesis of a polar low. Such a spin-up effect enhances the low-level baroclinicity, and a comma-shaped cloud (see, for example, Figure 2.5) develops in the regions of enhanced baroclinicity (Businger and Reed, 1989a). Once formed in this way, polar lows may amplify due to the effect of convection and latent heat release from the cloud bands.

Often, this type of polar lows develop as a series of comma clouds along the surface trough axis of a synoptic scale cyclone. A satellite image of such a development which was observed on 18 November 1981 is shown in Figure 2.10. Ralph et al. (1994) distinguished between two classes of such a wave-train formation, viz.,

(i) meso-cyclones that form due to 'frontal instability' and characterised by a quasi-simultaneous growth of more than one cyclone, and

(ii) meso-cyclones that form sequentially downstream of an initial cyclone.

The example shown in Figure 2.10 indicates the first type i.e., a simultaneous development due to frontal instability. The second type of development i.e., the sequential, downstream development of new meso-cyclones in an ideal baroclinic channel is illustrated in paper-III.

It is possible to estimate the degree to which baroclinic processes and/or convective processes influence the cyclone by an analysis of the vertical motion (ω) associated with the system using the quasi-geostrophic omega equation (Holton, 2004; pp 165) which is given by

$$\left\{\nabla^2 + \frac{f^2}{\sigma}\frac{\partial^2}{\partial p^2}\right\}\omega = \frac{f}{\sigma}\left\{\frac{\partial v}{\partial p}.\nabla(f+\zeta)\right\} - \nabla^2 H \tag{2.3}$$

where H represents the contribution to ω from diabatic effects, σ refers to static stability parameter and ζ denotes relative vorticity. $\partial v/\partial p$ signifies the thermal wind. f is the Coriolis parameter. The terms on the right-hand side of the above equation represent the ω-forcing due to the advection of relative vorticity with the thermal wind (adiabatic forcing) and that due to diabatic effects respectively.

Nordeng (1990) utilised the above relation to diagnose two polar lows with similar initial developments but different characteristics during the mature phase. He noticed that, in one of the two developments the vertical motion was forced by the advection of relative vorticity only. But in the case of the second polar low, diabatic processes played a significant role that led to a prolonged phase of the polar low. The same

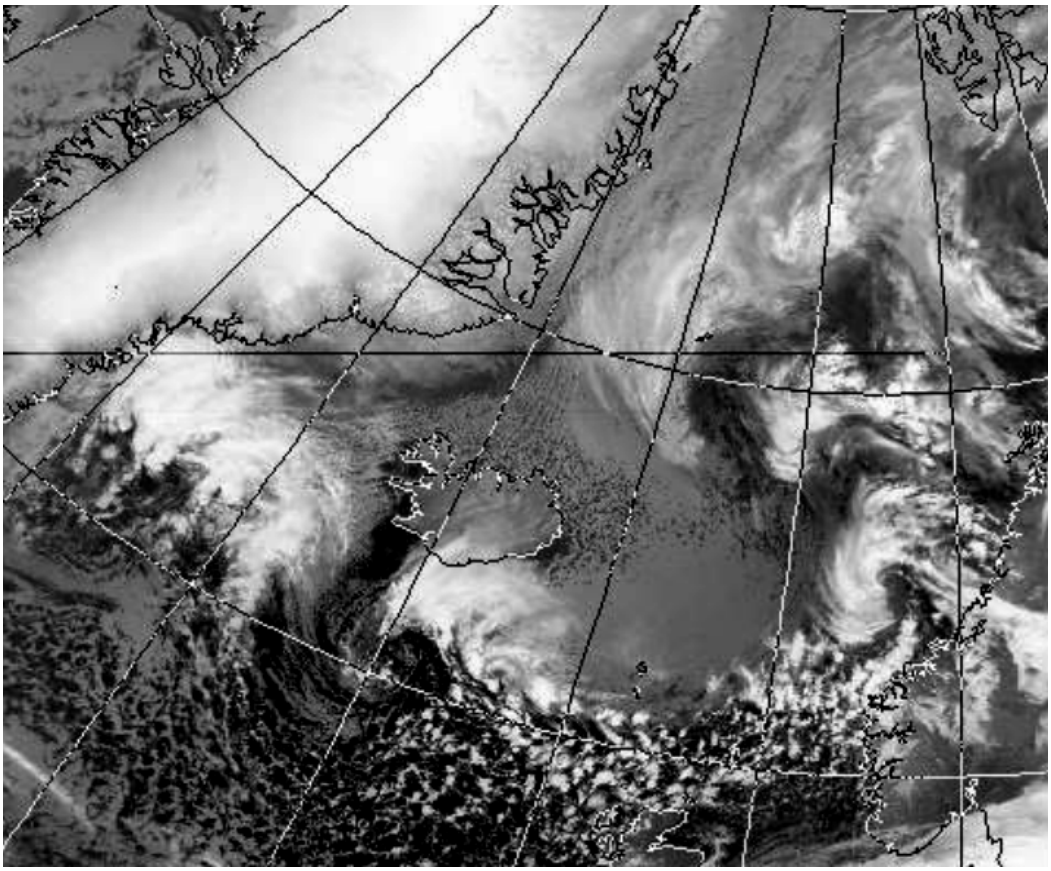

Figure 2.10: *An infrared satellite image valid at 1423 GMT, 18 November 1981 showing four comma-shaped polar lows over the Norwegian sea. (Image courtesy: NERC satellite receiving station, University of Dundee).*

approach has been used in paper-II and paper-III to understand the sensitivity of the pattern of vertical motion associated with polar lows to certain background conditions.

2.4.3 Nordic Seas climatology of polar lows

In this section, some important climatological investigations, each with a different approach, of polar low occurrences is described. The first subjective climatology of polar lows occurring over the Nordic Seas was given by Wilhemlsen (1985). From weather maps corresponding to the Nordic Sea region for the time period 1978-1982, Wilhelmsen identified 33 cases of polar lows with winds of gale force or higher. Wilhelmsen found that these polar lows were more frequent in December and January. All the polar lows were observed in weather situation with wind either from north or northeast or northwest over the Nordic Seas and with synoptic cyclones situated anywhere between Iceland and Novaya Zemlya. Average phase speed of all the polar lows was in the range 8 to 13 ms^{-1}. Most of the polar lows formed above 70^0 N and propagated in a southerly direction. Later, Rasmussen and Turner (2003) classified the polar lows studied by Wilhelmsen into different groups based on the associated synoptic conditions. These classifications are given in Table 2.2.

Through a statistical approach, Businger (1985) constructed composites of 500 hPa height and temperature, 1000−500 hPa thickness and surface pressure fields in connection with polar low outbreaks between 1971−1982. 52 cases were identified by Businger on the basis of the data from satellite imagery and Norwegian coastal stations. The results from this composite study revealed the presence of significant negative anomalies in both 500 hPa height and temperature fields, indicating strong positive vorticity and low static stability during the polar low events, over the Norwegian and Barents seas. As observed by Wilhelmsen (1985), significant northerly component of the low-level flow, which results in strong low-level baroclinicity, was found during each polar low outbreak event. Further, rapid intensification of the polar lows was associated with deep convection caused by low static stability.

Using satellite imagery spanning the period October 1993−September 1995, Harold et al. (1999a, b) analysed polar low developments over northeast Atlantic and Nordic Seas. Harold et al. (1999a, b) found strong seasonality for the polar lows, with peak activity in winter and weak in spring. Most meso-cyclones formed over more northern latitudes near the ice-edge, with 86% of the meso-cyclones having a diameter less than 400 km. The lifetime of most of the systems was less than a day and were seen to be covering short distances before being dissipated. The causal mechanism of the short-scale systems was baroclinic instability as they formed in the proximity of shallow baroclinic zones associated with the ice-edge. For larger systems (still in the mesoscale domain), convective instability was the major forcing mechanism.

In the classification of Rasmussen and Turner (2003), which is shown in Table 2.2, reverse shear polar lows constitute one of the major groups. Kolstad (2006) constructed a new climatology of favourable conditions for reverse shear polar low developments over the Nordic Seas. Kolstad applied two dynamical constraints−one on static stability and the second on the magnitude of the reversed wind shear−to the ERA-40 dataset in order to identify the developments. The constraint on static stability is that it must be sufficiently low so that the normalised dimensionless Rossby radius of deformation (R_N) is less than 80. The relation between Rossby radius of deformation and static stability is given by:

$$R_N = \frac{L_R}{H} = \frac{N}{f_0} \tag{2.4}$$

where H is the height of the tropopause, f_0 is the Coriolis parameter and N is static stability. L_R is the actual Rossby radius of deformation (which is given by $L_R = NH/f_0$). The constraint on the magnitude of the reversed wind shear is that the angle (α) between the thermal wind vector and the mean wind vector at the steering level (either the 775 hPa level or 850 hPa level in Kolstad, 2006) is between 135 and 225 degrees, i.e., $135^0 \leq \alpha \leq 225^0$.

Kolstad (2006) analysed the 'polar low potential', which signifies the fulfillment of either or both of the constraints defined by him, for the months November to March (NDJFM) during the period 1960-61 to 1999-2000. Figure 2.11 shows the mean percentage of the occurrence of the polar low potential in different regions. Figure 2.11a shows that the regions most affected by the reverse shear constraint are the Greenland and the Norwegian seas, with the Barents sea also showing considerable response. The percentage of the wintertime when the low static stability constraint was fulfilled (i.e., $R_N \leq 80$) is shown in Figure 2.11b. The Norwegian and the Barents seas seem to sat-

isfy this constraint nearly half the time during the 40 years of time period. Regarding the polar low potential in terms of both the constraints, it is clear from Figure 2.11c that the Nordic Seas account for a major part of this potential. Furthermore, the polar low potential appears to occur with high frequency over the Norwegian sea (>15% of the time during NDJFM) with a local maximum over the southern Denmark strait (>10%) and the Bering sea and Sea of Okhotsk (>5%).

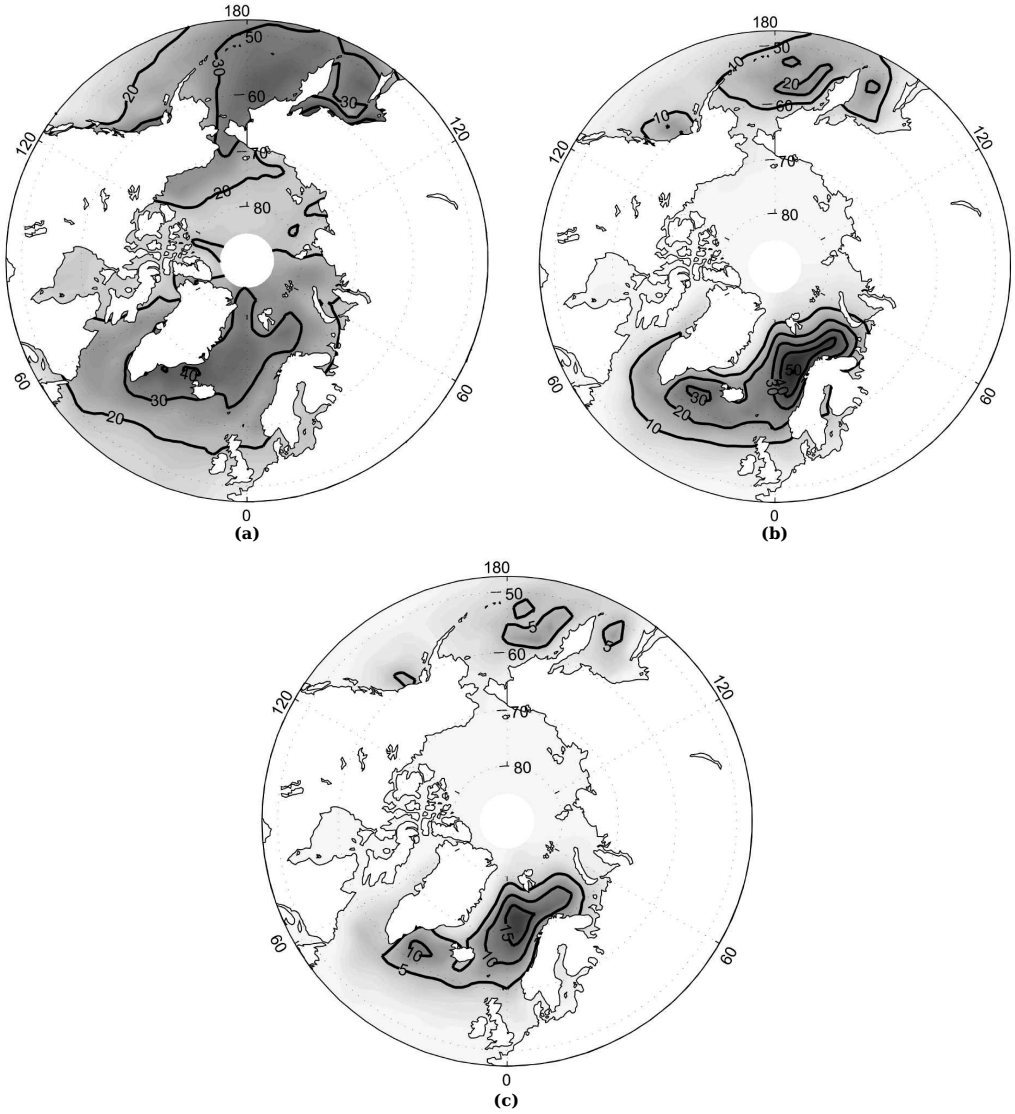

Figure 2.11: *Mean percentage of the time during NDJFM 1960-61 to 1999-2000 for each grid point with, (a) the reverse-shear constraint only, (b) the static stability constraint only, and (c) with both the constraints. From Kolstad (2006).*

The interannual variability of the polar low potential with regard to the local maxima as in Figure 2.11c was also studied by Kolstad (2006). He selected two basins for the analysis: the Norwegian sea and the Sea of Okhotsk. Figure 2.12 shows the interannual variability of the occurrences of polar low potential for the Norwegian sea. The figure indicates that there is a fairly large year-to-year variability in the polar low potential. Kolstad (2006) suggests that there might be a link between the number of occurrences of potential during one winter and the frequency of blocking high-pressure systems over Scandinavia over the same period.

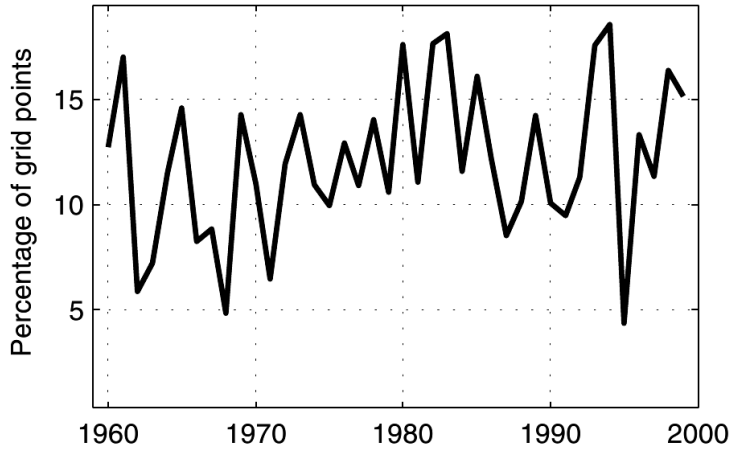

Figure 2.12: *Interannual variability of occurrences of polar low potential for Norwegian sea. From Kolstad (2006).*

Bracegirdle and Gray (2008) compiled a new climatology of polar lows developed over the Nordic Seas during January 2000−April 2004 based on an objective technique. They chose the Cyclone Database developed by Hewson (1998a) which is a database of diagnostics of objectively identified cyclonic activity during the January 2000 to April 2004 period. Bracegirdle and Gray quantified the cyclonic activity in terms of an index called the 'count density', which refers to the occurrence of cyclonic events within area bins of 200 km radius at each model grid and at each time interval. Further, they classified the polar lows on the basis of dynamical forcing in terms of a quantity called the 'U/L ratio' which refers to the ratio of upper to lower level forced vertical circulation. When the ratio was greater than 4.0, the polar lows were considered to be of a convective nature and when the ratio was under 4.0, the polar lows were considered to be of a baroclinic nature. Figure 2.13 show the count density of both types of polar lows occurred over the Nordic Seas during the above-mentioned period. The convective-driven polar lows were found to be restricted over the region south of 70^0 N (Figure 2.13a) and the baroclinic-driven systems were observed to develop mostly north of this latitude (Figure 2.13b).

2.4.4 Numerical modelling of polar lows

Earlier research into polar lows relied heavily on various in-situ and remote sensing observations since the numerical models were too coarse to simulate these mesoscale phenomena. A breakthrough for the simulation of polar lows was achieved when a mesoscale NWP model system (Norwegian Limited Area Model - NORLAM) was established as part of a polar low project organised by the Norwegian Meteorological Institute (DNMI) in the 1980s (Lystad, 1986; Rasmussen and Lystad, 1987; Grønås et al., 1987b; Grønås and Hellevik, 1982; Nordeng, 1986). The first realistic numerical simulations of some polar lows were obtained from this model (Grønås et al., 1987a, Nordeng, 1987). These simulations, and further high resolution modelling experiments that followed later on, provided crucial insight into the dynamics of polar lows over the Nordic Seas and other genesis areas. A brief description of some important modelling

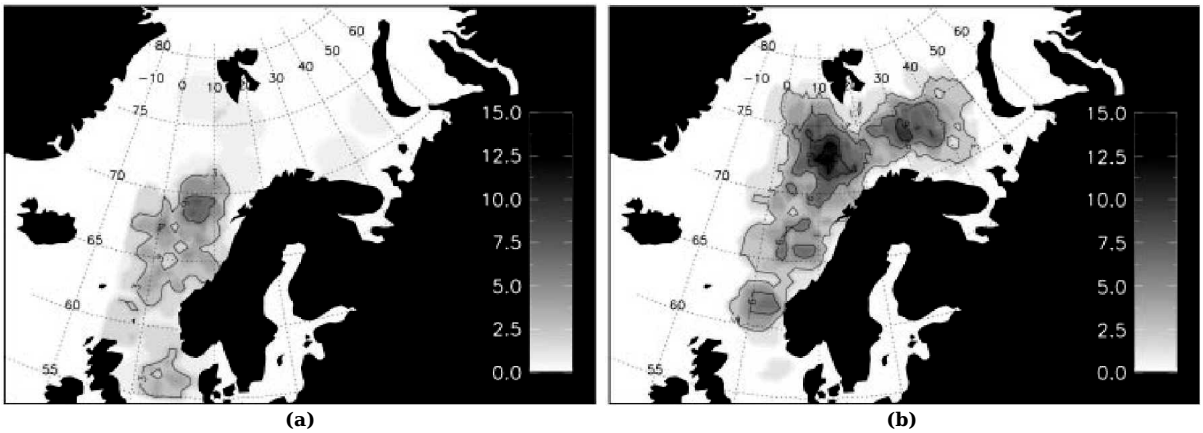

Figure 2.13: *Count density of polar lows for (a) polar low events with U/L>4.0, and (b) polar low events with U/L<4.0. From Bracegirdle and Gray (2008).*

studies of polar low developments over the Nordic Seas is given below.

Grønås et al. (1987a) used the NORLAM system at a horizontal resolution of 50 km and with 10 σ-levels in the vertical. The lateral boundary conditions were obtained every 6 hours from a larger domain (with a horizontal resolution of 150 km) of the same model which in turn used the information from the ECMWF analyses at its lateral boundaries. The model was hydrostatic. Using this set-up, Grønås et al. (1987a) simulated a number of polar low developments and compared the results with published subjective analyses. Grønås et al. (1987a) showed that the mesoscale model was able to predict the location and the time of development of all the polar lows rightly, though the predicted intensity was quite weaker. Nordeng (1987) followed up this study with an objective of investigating the importance of parametrisation of condensation processes at different scales on the simulations of polar lows. The simulations of Nordeng showed that the release of latent heat is very important for predicting the observed intensity of polar lows.

Nordeng (1990) utilised NORLAM with a horizontal resolution of 25 km and 18 vertical levels to diagnose two polar low developments that took place over the Norwegian Sea. This model-based study showed that the driving physical mechanism of polar lows are very sensitive to underlying surface features. Both the lows studied by Nordeng (1990) were initiated due to baroclinic instability. However, convective instability became important for one polar low as it grew with strong influences from a warm sea-surface. On the other hand, the second polar polar low was not affected by convective instability due to the effects of ice-covered sea-surface and the low decayed after the lower-level baroclinic zone weakened. Using the same model set-up, Nordeng and Rasmussen (1992) investigated a polar low which had a clear cloud-free eye surrounded by convective cloud bands, a structure similar to tropical cyclones. Nordeng and Rasmussen identified an upper-level positive potential vorticity anomaly above the location where the polar low started to develop, indicating that the triggering mechanism was baroclinic instability. A deep vertical circulation developed later on and the polar low intensified through the self-induced CISK mechanism (see section 2.4.1) and acquired a spiral shape.

Grønås and Kvamstø (1995) analysed four cases that satisfied the conditions favourable for the development of polar lows−a northerly cold air outbreak followed

by an Arctic inversion−as suggested by Wilhelmsen (1985) and Businger and Reed (1989b). For their analysis, Grønås and Kvamstø employed the NORLAM model at a horizontal resolution of 50 km and 18 vertical σ-levels with the addition of a hydrological cycle according to Sundqvist et al. (1989). They found that polar lows had developed in only two of the four cases. To understand as to why polar lows did not develop in the rest of the two cases in spite of all the four cases satisfying the basic necessary conditions, Grønås and Kvamstø focused on the vertical distance (H) between the tropopause (defined by them as the 2 PVU surface) and the top of the convective boundary layer. Their study indicated that H was ~ 1 km in the two cases where polar lows formed, implying a significant tropopause fold and a vertical PV coupling. In the cases where no polar lows formed, H was higher than 2.5 km. These results demonstrate that an upper-level forcing might be necessary pre-requisite for many polar lows developing over the Nordic Seas apart from the basic conditions suggested by Wilhelmsen (1985) and Businger and Reed (1989b). Additionally, the simulations by Grønås and Kvamstø highlighted the importance of latent heat release during the growth of many Nordic Sea polar lows.

Nielsen (1997) simulated a polar low, which formed over the Norwegian sea in October 1993, using an experimental version of HIRLAM (a mesoscale model from the Danish Meteorological Institute). The model was run at a horizontal grid distance of 0.42^0 and 31 vertical levels with a domain coverage of the European region, North Atlantic, the polar region and a part of Canada. Nielsen's analysis of the model simulations, using the quasi-geostrophic tendency and the omega equations, revealed that the polar low had developed due to baroclinic instability. During its growth, the air-sea interaction instability gradually took over the baroclinic mechanism. Nielsen reports that the environment where the polar low developed was neutral to deep convection and CAPE values were insignificant, which prompted him to exclude CISK as a driving mechanism for the growth of the polar low. However, Rasmussen and Turner (2003) computed CAPE values during the growth of this polar low from NCEP/NCAR reanalysis and claimed that the CAPE values were indeed high and hence CISK could have played an important role in the growth of the polar low. Rasmussen and Turner suggested that the discrepancy might probably be due to the convection schemes used in the HIRLAM by Nielsen. Nielsen (1997) conducted another experiment wherein the latent heating was excluded. No polar low formed in this experiment, which highlights the importance of latent heat release for the formation of polar lows over the Norwegian Sea.

Role of observations in modelling polar lows

Observations of polar lows have been a crucial component in the modelling as well as forecasting issues of polar lows. Observations aid modelling issues of polar lows by either or both of the following two ways. First, the use of observations to validate model results. If a model shows large deviations from the corresponding observations, one may consider to look where the model is going wrong and modify parametrisation schemes so that the simulations become comparable with the observations. Once a model shows minimal deviations from the observations, the model can be used as a forecasting system. Second, improving the initial conditions of a model by ingesting the observations into the model through advanced assimilation systems. With these

methods, reasonable simulations of polar lows have been made in recent years (e.g., Grønås et al., 1987a; Nordeng, 1987; Nordeng, 1990; Rasmussen and Nordeng, 1992; Nielsen, 1997).

On the issue of predictability of polar lows, Nordeng (1990) suggests that at least some polar lows, those triggered by upper-level short wave disturbances, are predictable. The reasoning of Nordeng (1990) is that the forecasting problem reduces to forecasting the upper-level vorticity maxima correctly, since the lower-level baroclinic zones are strongly related to fixed surface features. Røsting et al. (2003) and Røsting and Kristjansson (2006) have shown that polar low forecasts can be improved by modifying the potential vorticity fields associated with upper-level disturbances by the use of satellite-derived water-vapour images and singular vector dynamics.

Initially, satellite observations and two-dimensional surface measurements and/or vertical profiles were the only source of observations of polar lows. The first observations of the three-dimensional structure of a polar low over the Norwegian sea were collected during the Arctic Cyclone Expedition (ACE) in February 1984 and are reported in Shapiro et al. (1987). Airborne measurements of wind, temperature, moisture and precipitation associated with the polar low were taken by flying the NOAA WP-3D research aircraft, containing dropwindsonde and radar sensors, into the polar low during ACE. The polar low development took place as a response to baroclinic forcing by a short-wave, eastward propagating upper-level trough and was very intense with a surface wind speed of ~ 35 ms^{-1} and upward surface fluxes exceeding 1000 Wm^{-2}. Unlike many polar lows over the Norwegian sea that develop under reversed-shear conditions, the polar low observed by Shapiro et al. (1987) developed under forward-shear conditions. Grønås et al. (1986) simulated this polar low with a 25 km version of the NORLAM system and found that the model failed to show the rapid intensification of the polar low as reported by Shapiro et al. (1987) since the model did not account for sub-grid scale processes like subsidence at the cyclone core (Grønås et al., 1987a).

Another field campaign was conducted over the Nordic Seas during February-March 2008 as part of the IPY-THORPEX project with the objective of collecting observations of adverse weather in the Arctic region (Barstad et al., 2008). Upper-air observations of various severe cases were recorded during the campaign with the help of dropwindsonde, wind and water-vapour lidar sensors aboard the DLR-FALCON research aircraft. The aircraft was flown into a polar low which developed over the Norwegian sea on 3-4 March 2008 and the mesoscale structure of this polar low was recorded (Wagner, 2011). Apart from this, an interesting event was also observed on 1 March 2008 during the field campaign. During the early hours of 1 March, a low pressure system had formed at the surface on the Barents sea. Later on, this low propagated northwestwards while showing signs of deepening. However, the surface low crossed the ice edge after 1200 UTC, 1 March and immediately started decaying. Sensitivity experiments were performed for this case in order to test if, by removing the ice-cover or by increasing the sea-surface temperature, the surface low could develop further as a polar low. These experiments are described in paper-II of this thesis.

Sensitivity experiments-assessing the sensitivity of polar lows in numerical models

Sensitivity of polar lows to model physics and resolution, underlying surface features like sea-surface temperature and the distribution of ice-cover, scale and structure of

upper-level disturbances, and different physical parameters like static stability and baroclinicity has been investigated in many studies. Roch et al. (1991) showed the importance of very high resolution model integrations to simulate polar lows and understand their sensitivity to various parameters. The polar lows studied by Roch et al. (1991) showed more sensitivity to the ice-cover in a 25 km resolution run than that in a 50 km resolution run. Roch et al. (1991) prescribed complete ice-cover in one of the sensitivity runs which did not favour the genesis of a polar low, implying the importance of open water for the formation of polar lows.

Albright et al. (1995) extended the case study of Roch et al. (1991) with more sensitivity experiments. Albright et al. (1995) focused on the significance of sea-surface temperature and surface fluxes on the polar low simulated earlier by Roch et al. (1991). The sensitivity experiments revealed that the fluxes of heat and moisture from open water and the associated latent heating in deep organised convection were essential for the polar low development. In an experiment wherein the SST was raised by 8^0 K, the strength of the polar low increased significantly from that in the control run, with the associated wind speed reaching hurricane force (~ 30 ms^{-1}).

Sardie and Warner (1985) simulated certain polar low cases and conducted a couple of sensitivity experiments to understand relative importance of CISK and baroclinic instability in the formation and growth of the polar lows. Different combinations of model physics were prescribed at the initial conditions by switching on/off convective and non-convective parametrisation, and upward surface fluxes so that the degree of baroclinicity and CISK are different in each of the experiment. The polar lows had grown to the observed wavelengths at observed rates in the control experiment (with full model physics). The growth rates and wavelengths obtained from the sensitivity experiments showed certain deviations with respect to the observed values. The experiment with no convective parametrisation (i.e., no CISK) produced the least deviation of all, which prompted Sardie and Warner to conclude that baroclinic instability was dominant during the initial stages of the polar low development. However, CISK-driven processes were essential for the maintenance of the polar lows.

Using the NORLAM system, Heinemann (1998) simulated a case of mesoscale cyclone development that occurred over the Weddel Sea in the Antarctic during the Winter Weddel Sea Program field phase 1986. The simulations were realistic when compared to very high resolution radiometer data and radiosonde measurements made by the vessel *Polarstern*. The mesoscale cyclone considered by Heinemann was formed near the sea-ice front of northern Weddel sea and moved eastward parallel to the sea-ice front during its growth. Sensitivity experiments performed by Heinemann showed that both baroclinic instability and diabatic heating in the clouds were crucial during the initial 24 hours of the growth of this cyclone. During its mature phase, the cyclone was associated with a pronounced frontal band and Heinemann suggests that baroclinic instability was the major forcing mechanism at this stage. The simulations revealed the presence of a positive potential vorticity anomaly at upper-levels above the cyclone during the mature phase.

Sensitivity experiments in an idealised atmosphere have proven useful in order to account for the relative importance of individual physical processes in the development of polar lows. Using a three-dimensional non-hydrostatic model, Yanase and Niino (2007) investigated the way individual processes influence polar lows. The basic state for the study was characterised by an axi-symmetric vortex at the surface with a finite

radius and an uniform vertical shear of the zonal wind. The experiments of Yanase and Niino revealed that the structure of the polar low was highly sensitive to the degree of baroclinicity present in the troposphere. An inclusion of condensation heating and surface fluxes resulted in an enhancement of the growth rate of the polar low. This work effectively demonstrated the impacts of different physical conditions on the growth rate, energetics and structure of polar lows.

Paper-II and paper-III of this thesis too deal with sensitivity of polar lows to the modifications in the surface conditions and background physical factors. Paper-II is based on a real case wherein certain conditions favourable for polar low development were observed but no polar low developed. By modifying the Arctic ice-cover and sea-surface temperature, the possibility of triggering a polar low from the favourable conditions is tested in the paper. In paper-III, polar low developments are investigated in an ideal baroclinic channel. The impacts of different initial conditions with varied degree of baroclinicity, surface heating and static stability on the internal dynamics of polar lows are studied in this paper.

2.5 General conclusions and future perspectives

In the form of three scientific articles, this thesis highlights the sensitivity of severe mesoscale weather events occurring over the Nordic Seas to underlying surface conditions and several physical factors. The first two papers are based on the real cases of adverse weather conditions observed during the IPY-THORPEX field campaign over the Nordic Seas during February-March 2008. The last paper brings forth the experiments carried out in an ideal baroclinic channel in order to study the relative significance of important physical parameters on the growth of polar lows. Important findings of this thesis are:

(i) The relatively warm basins of the Nordic Seas are likely to modify the mesoscale flows associated with strong winds emanating from the mountain ridges in the coastal regions. The warm surface provides moisture and buoyancy to the mesoscale structures, and thus contributes significantly to the maintenance of these flow structures.

(ii) Fluxes of sensible and latent heat released from the warm Nordic Seas play a decisive role in the formation of Arctic fronts in the vicinity of the ice-edge. It appears also that Arctic fronts are sensitive to the strength of the inversions over the ice-cover.

(iii) The relatively high sea-surface temperature of the Nordic Seas might have strong impacts on the characteristics of small-scale upper-level perturbations embedded in large-scale extratropical cyclones. Strong air-sea interactions caused by high values of sea-surface temperature could force a downward penetration of the upper-level disturbances, leading eventually to the genesis of polar lows.

(iv) The dynamics and structure of polar lows are highly sensitive to several physical parameters such as the degree of baroclinicity, static stability, surface heating, and the scale and structure of the upper-level perturbations. Concerning the relative

influence of these parameters on the characteristics of polar lows, baroclinicity and surface heating seem to have the strongest influence on the pattern of vertical motion associated with a polar low. On the other hand, growth rate of a polar low looks to be more dependent on the degree of static stability than on baroclinicity and/or surface heating.

Given the wide spectrum of polar lows spanning up over the Nordic Seas, the above conclusions may not be applicable to all the categories. Particularly, the relative influence of individual physical parameters on the formation and growth of polar lows was assessed only for the polar lows developing under forward-shear conditions. It remains to be seen if the reverse-shear polar lows too have a similar behaviour as their forward-shear counterparts. Furthermore, the impacts of topographical barriers on polar lows is unclear. This issue could be accounted for by setting up ideal or real topography in the ideal baroclinic channel used for the present work.

Having assessed the sensitivity of polar lows to sea-surface temperature and the distribution of ice-cover, it would be interesting to analyse the role of sea-surface temperature gradients near the ice-edge on the development of polar lows. Option of carrying out certain numerical experiments regarding this aspect is being considered. Also, assimilating the observations of several high impact weather cases recorded during the IPY-THORPEX field campaign into a numerical model using three- or four-dimensional variational analysis technique could be one of the ways ahead.

Chapter 3

Scientific results

Paper I

I

3.1 Observation and modelling of gap flow and wake formation on Svalbard

List of authors
Idar Barstad and Muralidhar Adakudlu
Quarterly Journal of Royal Meteorological Society. 2011. **Accepted**.

Observation and modelling of gap flow and wake formation on Svalbard

as of 18th Aug'10
Rev:12 Nov'10

Idar Barstad and Muralidhar Adakudlu
Bjerknes Centre for Climate Research

Abstract

Aircraft observations, satellite information and model simulations are presented for an episode with significant local disturbances in the vicinity of Spitsbergen, Svalbard archipelago in the Barents Sea. Relative weak upstream winds from the east gave rise to strong local winds in the Hinlopen Strait which separates Spitsbergen from the Nordaustlandet Island. The aircraft data encompassed wind lidar, water vapour lidar and dropsondes observations. The aircraft flew through the Hinlopen Strait and found winds near 20 ms^{-1} in magnitude close to the surface. This is a factor of about four to the upstream wind magnitude. In the lee of the terrain, a wake with return currents was formed and this was clearly documented by the lidar observations. The model simulations reproduced the episodes with high degree of fidelity. In the lee of the mountains, small-scale cloud features appeared both in the lidar data and in the satellite observations. For wind directions with easterly and northerly components, these features are frequently observed on satellite pictures downstream Spitsbergen. In the model framework, the cloud streamers were further investigated. Through sensitivity tests and more idealized simulations, it was found that the features plausibly stem from vertical circulations set up by terrain and maintained by the positive buoyancy gain downstream over the relatively warm water.

Keywords: Arctic, Svalbard, Spitsbergen, gap flows, wakes, jets, lidar.

1. Introduction

The element of surprise in weather forecasting has proven fatal for many fishermen and other users of the seas. Abruptly changing weather conditions have caused far more dangerous situations than more severe, but well forecast events. Poor forecasts may have several origins. Improved understanding of model capabilities as well as understanding of the phenomena in question will ultimately enable users to take precautions. Strong winds in terrain gaps (gap flow) and wakes are commonly found along the rugged coast of Norway, and have caused many accidents. Gap flows with wind speeds well above gale force are typically found adjacent to weak wind areas in wakes –often

with opposite flow directions. In between, strong shear lines exist. A fishing boat steaming from the calm weather in the wake into the strong gap wind will often be taken by surprise and inexperienced seamanship may lead to fatalities.

The IPY/Thorpex-Norway project focused primarily on adverse weather in various forms and stages of development, see Barstad et al. (2008). The weather phenomena of particular interest were polar lows, arctic fronts and terrain induced disturbances. The DLR-Falcon (FA20) aircraft was used during this campaign. In this note, we will present observations taken by the FA20, satellites and model simulation results related to terrain-induced disturbance in the Svalbard archipelago, Barents Sea.

On February the 27th, 2008, there was a period of relative calm weather around Svalbard (The 10-m winds in the ECMWF-analysis were about 5 ms^{-1}). Weak east to southeasterly winds prevailed and the FA20 equipped with a wind lidar and dropsonde unit, flew a mission surveying the disturbances in the vicinity of Svalbard. The mission was designed to observe the gap flow in the Hinlopen Strait separating the islands Nordaustlandet and Spitsbergen in the Svalbard archipelago. The mission was extended by a perpendicular oriented leg behind the tallest mountains, in the exit region of the strait.

The theory of gap flows have long been studied, both in terms of a single-layer hydraulics theory approach (e.g. Schär and Smith, 1993a,b), Boussinesq approximation linear theory (e.g. Pan and Smith, 1999), numerical modeling of fully a compressible atmosphere (e.g. Garbesek and Durran, 2004) and through studies of observations (e.g. Armi and Mayr, 2007). See Mayr et al. (2007) for an overview on the theory and a lengthy discussion on gap flow studies. During the MAP field campaign (Bougeault et al.; 2001), studies of the jets associated with gaps in the Alpine terrain showed that individual terrain obstacles produced potential vorticity (PV) banners, e.g. Jiang et al (2003); Schär et al. (2003). From the above studies, it is agreed upon that the main mechanisms driving the gap flows is the pressure difference across the barrier, but the role played by dissipative mechanisms in formation of the lee side wakes, is more uncertain.

The theory of wakes has been investigated by many authors throughout the years. The definition of wakes has been disputed. Smolarkiewicz and Rotunno (1989) related wakes to relative vorticity signal whereas Smith (1989; 2001) point at PV-generation criterion as a better measure for wakes. Smith et al. (1997), Grubisic et al. (1995) and Schär and Smith (1993a,b), investigated wakes and found four regimes appearing as the mountain becomes progressively larger; i) no wake, ii) long straight wake and

for tall mountains iii) eddy shading or a iv) steady eddy structure. Barstad and Grønås (2005; 2006) highlighted the effect of southern Norway on the formation of mesoscale features, and found the linear theory holds well for jets and upstream minima, but performs poorly for wake-like features.

Sandvik and Furevik (2002) described a similar case as the one herein, but their investigation had solely surface observations to rely upon. They modeled the flow with a 2 km grid and compared with SAR images and ship measurements taken in the area. They found a speed-up in the Hinlopen Strait of about 3 times (maximum 15 ms^{-1}) the magnitude of the upstream winds, concluding that the model under-predicted the wind speed magnitude in the Hinlopen Strait.

In section 2, the methodology used for our investigations is presented along with our observational platform in the campaign. In Section 3, observations of the event along with model simulations are presented. The conclusions are found in Section 4.

2. The observational platform and model configuration

During the IPY/Thorpex-Norway campaign (February and March 2008), the FA20 was stationed at Andøya in northern Norway. The aircraft carried its wind and water vapor lidar (Weissmann et al., 2005) and had the capability to launch dropsondes. The aircraft also sampled fluxes measured by flux probes mounted on the aircraft. In this paper, we will focus on the data collected by the lidars and the dropsonde unit. The FA20's mission for 27 February 2008, shown in Figure 1, was to record offshore flows along the Finnmark coastline, perform a lidar scan across the remains of an occluded front in the Barents Sea, and to sample gap flows in the Hinlopen Strait, which separates the Nordaustlandet and Spitsbergen islands. The duration of the mission required refueling at Longyearbyen, Spitsbergen. In this paper, we will focus on the Hinlopen Strait observations including the observations on the lee side of Spitsbergen and Nordaustlandet, and these observations were taken between 14:00 and 14:30 UTC the 27th of February 2008.

The Weather Research and Forecasting model (WRFV3.1-ARW; Skamarock et al., 2005) has been used to simulate the weather conditions on 27 February 2008. The model simulation had three 2-way nests with 9-3-1 km horizontal grid spacing and 51 vertical levels. 22 layers were confined to the lower 1 km. The two inner domains are shown in Figure 2. The simulation of the outer domain started the 26 February at 00 UTC, followed by the intermediate domain at 12 UTC and the inner domain at 18 UTC.

The simulation was terminated 27 February at 18 UTC. The ECMWF-analysis provided the lateral boundaries and forced the lower boundary SST and sea-ice cover. Based on satellite information, the ECMWF sea-ice was corrected. As a result of this procedure, the sea-ice in the Hinlopen Strait was correctly removed. In order to ensure a synchronization between simulation and observations (Barstad et al. 2009), we apply a weak spectral nudging for wind, temperature and geopotential height (24 hr relaxation time for waves longer than 1000 km in the outer nest) outside the boundary layer. Mixing and vertical transport in the boundary layer is based on Hong et al. (2006). Computation of friction velocities and exchange coefficient at the surface is according to the Monin-Obukhov similarity theory (Monin and Obukhov, 1954; Janjic, 1996, 2002). Soil processes are accounted for through the 5-layer thermal diffusion scheme (Dudhia, 1996). Sub-grid scale convection in the 9 – and 3 km domains are parametrized using the Kain-Fritsch scheme (Kain and Fritsch, 1990, 1993). The property of sea-ice is similar as for snow covered land points in the simulation. In addition to the simulation of the episode (called CTL run), we have sensitivity tested the mesoscale features observed to sea-ice cover, referred to as SI-run. In this run, the whole area has been covered by sea-ice. There are also two idealized model simulations discussed later, and they have a similar set-up except as indicated in the text.

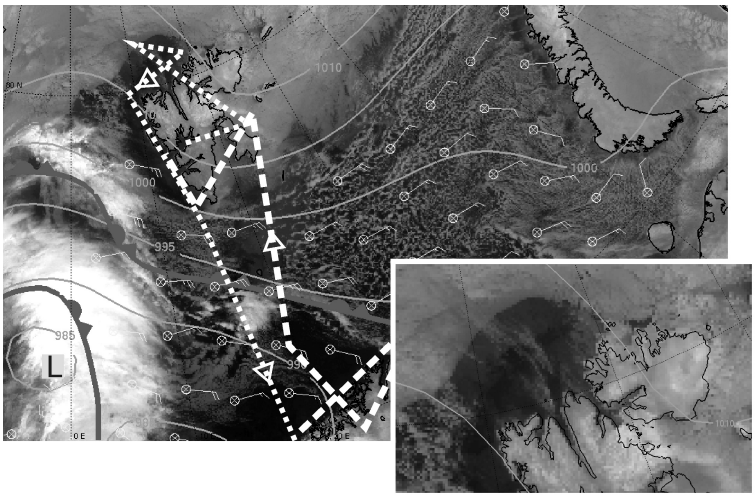

Figure 1. 12 UTC, 27 Feb 2008: NOAA-16, (infrared channel 5) overlaid by MSLP from the ECMWF +12 hr forecast, weather analysis from met.no, ASCAT-derived 10-m wind barbs and the flight track for the morning before refueling (white dashed line) and afternoon after refueling (white dotted line). Long tick in the wind barb reflects 10 kts winds. Zoomed-in section in the lee of Spitsbergen shown in white frame (flight tracks are omitted).

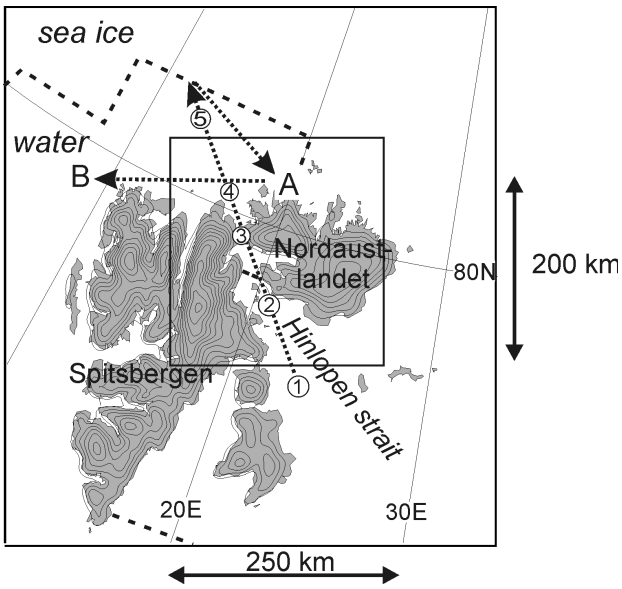

Figure 2. The area for the 3 km domain and the nested 1 km domain along with geographical names. The terrain contours every 100 m are shown for the 3 km grid. The sea ice edge for the CTL-run is indicated as a dashed line. Dotted arrows indicate the flight track (northward flying direction) through the strait having labels with numbered dropsondes (see Fig. 3). Cross-section in the lee (A-B) is shown in Fig. 4.

3. Observations and model simulations

3.1. The Hinlopen Strait and lee-side survey

In Fig. 1, a satellite picture displays the fair-weather conditions prevailing in this case. Some intermittent clouds are seen in the lee of the mountains. The MSLP from the EC +12 h forecast overlays the satellite picture and ASCAT data indicating weak upstream wind conditions (about 10-12 kts at 10 m) and relatively high winds at the south tip of Spitsbergen (up to 30 kts). The aircraft track which we will focus on is indicated by dotted lines in Fig. 2. The wind lidar scan is shown overlaid by dropsonde data in Fig. 3a. In Fig.3b, the model results are shown. The southeastern-most dropsonde (no.1) in Figs. 2 and 3, was released an hour before the others on the previous flight (before refueling). From model trajectory analysis, we find that low-level air in the gap entrance originates from the local area on the southeast side of Nordaustlandet, and the air above 500 m seems to originate from more remote areas upstream. Thus dropsonde no. 1 is representative for undisturbed upstream conditions when considering properties above the 500-m level. The wind speed in the gap was relatively low until the air impinged on to the mountains. It then increased, first and foremost near the surface. From the dropsondes, we see that the jet core is formed some distance from the surface (300-400 m) (sonde 2

and 3). Further into the gap, the jet is located next to the surface extending upwards (to a height of 300-400 m). From the wind lidar data, we find the wind speed reaches a maximum of about 20 ms^{-1} at the lowest level with useful data (400 m a.s.l.), near the gap exit. This is corroborated by the dropsonde information, but this indicates the maximum to be a little lower in altitude (250 m). The model results in Fig.3b show a similar tendency; the jet-core is found below the 500-m level. Isentropes (potential temperature surfaces) are marked by dots in Fig. 3, and the low-level air clearly ascends in the gap entrance, followed by a longer descent toward the exit. This is in line with what Gabersek and Durran (2004) found; acceleration in the gap exit follows from a net descent and wind speed increase.

After the gap leg, the FA20 flew a cross-flow survey immediately behind the largest mountains, see Fig. 2. There were no dropsondes released, but wind lidar information was gathered, and is shown in Fig. 4a. Clear evidence of the jet in the gap and reversed winds in the wake is displayed. Lidar data exists up to a height of about 750 m in the jet-area and wind speeds up to about 15 ms^{-1} are identified. From the water vapor DIAL lidar (not shown), we find there are signal indicating two cloud feature in the lee; one on the right-hand side of the jet (facing downstream) and the second in the wake itself. These cloud signatures are reproduced in Fig. 4a. According to the water vapour lidar, there are also elevated levels of water vapor molecules on the left-hand side of the jet. The right-side feature extends to a height of about 500 m, same as the elevated water vapor levels on the left side. The feature on the left side also appears on the satellite picture in Fig. 1 trailing downstream. The cloud top temperature is about 263-267 K indicating near-neutral conditions. The model simulations reproduced the jet and wake in an accurate manner, see Fig.4b.

In the wake area in the lee of Nordaustlandet, there are return currents (wind direction of $300\text{-}360^{0}$) reaching up to a height of about 1200 m. Cloud-top temperatures (deduced from satellite information) of clouds found in the lee display 260-265 K, and assuming sea-surface temperature of about 273 K, this indicates a near-neutral boundary layer. As previously mentioned, the DIAL-backscatter in the wake area indicates a cloud feature at the height of 1.2 km, at a similar location as the one barely seen on the satellite picture in Fig. 1. In the model, elevated Rh-values in this area reflect potential cloud formation (not shown). From the earlier satellite picture on the 27^{th} of February, we find that the meandering cloud feature in the wake is present the whole day, and as the background flow turned from easterly to more southerly during the morning hours, the cloud features shifts accordingly.

It is likely that the production of positive buoyancy over the relative warm sea surface, promotes

vertical circulation and feed moisture into the air. However, there seems to be pre-existing vertical velocities at the lower levels when the air leaves the terrain and comes out over the ocean. This circulation pattern is enhanced as the buoyancy enters into the circulation. The model results indicate that the meandering cloud features, originates from small-scale terrain at the northern end of Spitsbergen. Figure 5 shows vertical velocities at 950 hPa (found at a height about 440 m a.s.l) level near the Hinlopen Strait exit, and we see that the features originate from terrain structures such as fjords and valleys. We will return to these features later on.

The model simulation reveals pressure anomalies according to theory; as stable air is lifted over the mountains, a positive pressure anomaly appears upstream of the mountains and on the lee side a negative anomaly reflects the descent (e.g. Smith et al., 1997; Barstad and Grønås, 2005). The pressure gradient across the mountains contributes to pulling air through the gap. These anomalies may be weakened or strengthened due to various mechanisms. For instance, any lee-side heating strengthens the low pressure anomaly. The strong heat fluxes found in the model simulation encouraged us to perform another simulation, testing the sensitivity of the gap wind to sea-ice cover. The new model experiment had total sea-ice cover on the whole ocean area north of Spitsbergen. We refer to this as the SI-run. This experiment showed significantly reduced heating from the ocean on the lee-side and the pressure anomaly in the lee was reduced (1-2 hPa) and the maximum wind in the jet was reduced by about 1-2 ms^{-1}. The reduced lee-side heating in the SI-run, leads to a reduced buoyancy and moisture flux into the air and naturally to a much shallower boundary layer. The meandering features on the lee side are more or less absent, at least downstream in the wake area. Furthermore, the vertical velocity streamers extend to a lower height, containing less moisture and thus no air saturates at the top of the boundary layer.

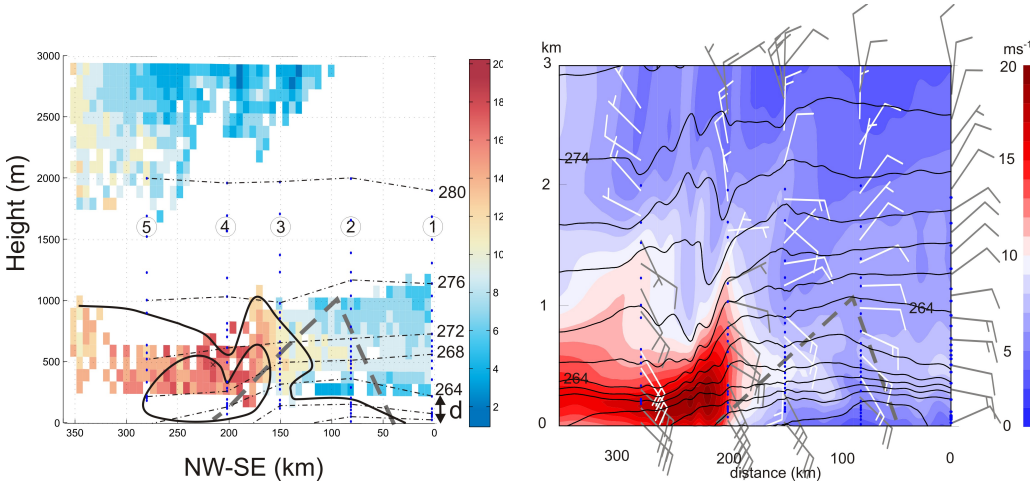

Figure 3. a) Observations from flight leg conducted between 14:00UTC and 14:30UTC displayed in a vertical cross-section through the gap as shown in Fig.1. Wind speed retrieved from wind lidar scan is shown in color. The hand-drawn curves (isotachs) are based on dropsonde information (found at the b-panel), the outer isotach equals 10 ms^{-1} and the inner equals 15 ms^{-1}. The dots show potential temperature every whole degree. The uppermost dot starts at 280 K, and every 4th degree are identified by broken lines. The large-scale terrain in vicinity is indicated by a heavy, broken line. “d” indicate a surface inversion of 9 K / 250 m. **b**) The model simulation (wind speed in color and theta as solid lines) of the same cross-section with dropsonde information overlaid. Dots are similar as in a). A long tick in the wind barb indicates 10 kts.

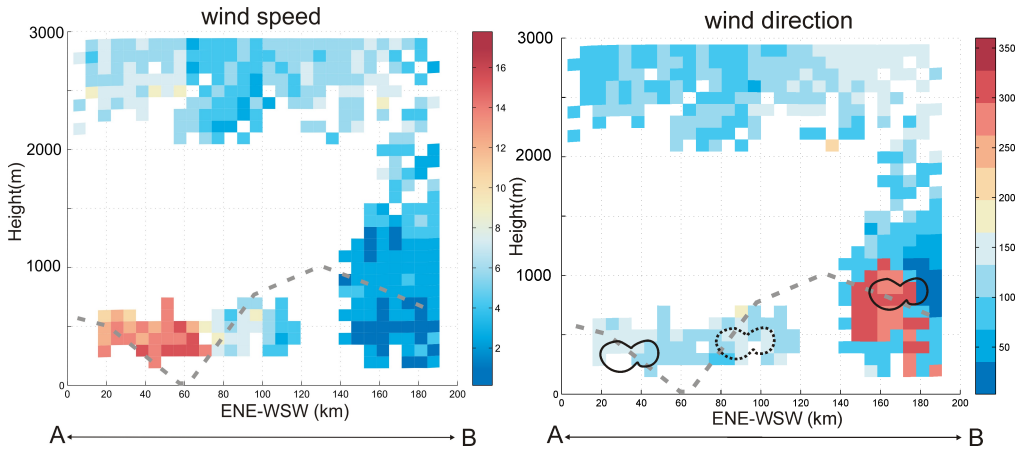

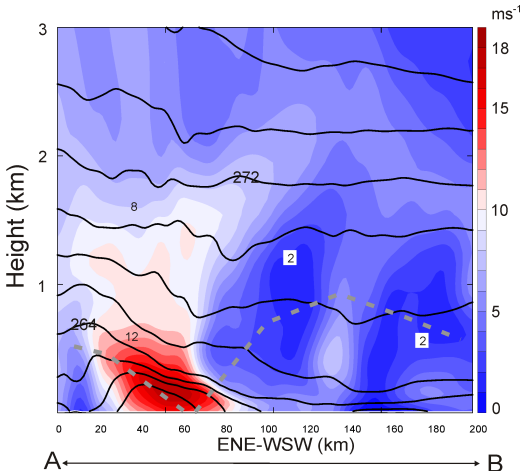

Figure 4. Vertical cross-section (A-B) as indicated in Fig.1 and 2 (same as flight track). Viewing southward. **a**) Wind lidar scan of the wake. Wind speed to the left and direction to the right. The silhouette of the large scale terrain is indicated by the grey, heavy, dashed line. On the right panel, the top of the cloud features observed by the water vapor lidar are indicated as solid thin lines. Area with elevated water vapor content is indicated by a dotted thin line, see text. **b**) Shows the model results for the same cross-section showing wind speed (every ms-1) and theta (every 2K).

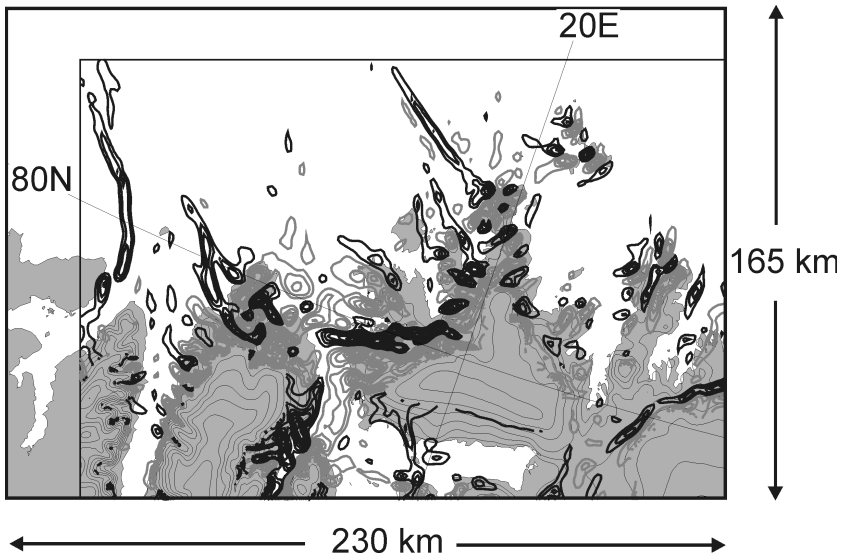

Figure 5. Results from model simulation for the inner domain (frame) valid at 27 February, 12 UTC shown at 950 hPa level. Banners of positive vertical velocities (thin lines with contour intervals equal to 0.1 ms^{-1}) extend out over the sea (black), and the negative velocities more confined to the terrain (gray). The exit of the Hinlopen Strait is in the middle of the figure and the terrain (solid lines, contoured every 100 m).

The simulation of the gap flow shows a weaker surface inversion than observed in dropsonde no.1, Fig. 3a. The observed depth was 250 m and strength 9 K/250 m. The model produced an inversion of depth 150 m with 6 K across. The model shows a tendency to produce a shallow boundary layer below the inversion, Fig. 3b. This may explain why the simulated inversion was too weak.

3.2. Idealized simulations

In easterly winds, meandering cloud features similar to those identified herein are frequently seen over the open water west of Spitsbergen. The easterly winds blow the statically stable air from the ice over or around the terrain continuing out over the open water. From satellite information, the cloud features can be identified as they are advected far downstream from the terrain, see also Skeie and Grønås (2000). Their implication is not established, but it is possible that they may act as triggers to larger scale disturbances such as polar lows. In our SI-run, these cloud features are absent, indicating that positive buoyancy formed above open water, is a vital factor in their maintenance – and may also be in their formation. Our hypothesis is that positive buoyancy above the sea surface is fed into an existing circulation signature formed by the terrain. The added buoyancy and moisture near the surface enhances the circulation and bring air to saturation at the top of the boundary layer. In order to get a better insight of these features, we will undertake another simulation where an ideal flow passes a constructed terrain.

The upstream atmospheric characteristics in our next ideal-flow simulation is similar to those on the upwind side of Svalbard for the time of investigation; a backward shear with height (a linear wind reduction with height) with about 10 ms^{-1} near the ground and 3 ms^{-1} at a height of about 3 km, constant further aloft. In reality the upstream low-level wind varies from 5-10 ms^{-1}. The stability –represented by the Brunt-Vaisala frequency- is set to N=0.01 s^{-1}. The incoming, dry flow is balanced on an f-plane with $f_0=1\cdot10^{-4}$ s^{-1}. The larger scale of the terrain is Witch-of-Agnesii type, but two “ears” separated by a fjord, have been added on the lee side. The formula for the terrain is:

$$H(x,y) = H_0 \exp\left\{-\left[\left(\frac{x}{a}\right)^2 + \left(\frac{y}{b}\right)^2\right]\right\} \cdot F \qquad (1)$$

where the “ears” are

$$F = \begin{cases} \exp(1.5[1-1.2\cos(y\pi/c)]) & \text{if } x \geq 0 \text{ and } |y| < c, \quad \text{and} \\ 1 & \text{otherwise.} \end{cases} \qquad (2)$$

The mountain top height is $H_0 = 1000$ m, the size of large-scale terrain is set via *a*=20 km, *b*=50 km and the distance in y-direction occupied by the half the fjord and one "ear" is *c*=20 km. Figure 6 shows the terrain and the results from the simulation. The centre of the mountain is located at a distance 1/3 of the total domain from the inflow (left) boundary and centered in the cross-flow direction (y-direction). The domain has 300 grid cells in the x-direction, and 140 cells in the y-direction. The vertical dimension has 41 levels. The horizontal grid spacing is set to 3 km. Short wave lengths have been removed from the terrain (filtered out) so that unresolved scales only impose small amounts of energy onto the flow solution.

The simulated flow started momentarily (c.f. Gabersek and Durran, 2004) and the model simulation was stopped at a quasi-steady state at about 10 hours, well before the downward-flowing disturbance from the mountain reached the model boundaries. The temperature at the lower boundary has been set to 270 K, which is comparable with that in the real case. The roughness length is in the order of 0.1mm. The relaxation towards the lower boundary is otherwise the same as in the standard setup.

From the results in Figure 6a, we clearly see that a streamer with strong vertical velocity moves out from the left slope of the left "ear". The vertical velocity in the streamer in Figure 6 is more than 0.1 ms^{-1} so that it is comparable in strength with the vertical velocities at the windward slope. When looking at the Ertel-PV for layers close to the ground, a tongue of a positive PV anomaly is clearly associated with the streamer with high vertical velocity. The anomaly stretches downwind for a distance less than the extension of the mountain. In a simulation similar to this except with a terrain having no small-scale "ears" (F=1 in 1), a similar PV-tongue is found. This is shown in Figure 6b. This PV-tongue is somewhat weaker and wider. From this, we infer that the small-scale terrain focuses the vertical velocity banners which the large-scale mountain has caused. Smith (2001) showed that PV forms as a result of dissipation (e.g. gravity wave breaking) in the flow, and Schneider et al. (2003) launched a concept where PV interior to the flow may be introduced as a result of either internal dissipation or by "pealing off" surface PV. A fundamental concept in PV-thinking is the conservation of PV. This requires that the identity of an air package is maintained. In strong mixing conditions, this is obviously violated. Another argument against PV-thinking is that PV is not defined at the fluids boundaries (at the ground). Disregarding the concerns mentioned above, the presences of the PV anomalies in the lee have an impact on the flow. In our simulations, however, we find very little differences in PV downstream of the mountain.

The simulations indicate concentrated banners of vertical velocities streaming downstream from fjord mounts - similar to those found in Ohigashi and Moore (2009). In their case study at the tip of Greenland, however, the vertical banners had more a signal of a bow-wave (Smith, 1980) which will be standing against the flow. The banners in this investigation drift more downwind seemingly fed with buoyancy from the ocean surface, arguing for another origin mechanism.

Smith (1989) showed how the non-dimensional mountain height ($\hat{H} = H_0 N / U$) controls the flow passing a mountain. Breaking gravity waves are associated with non-dimensional mountains heights around unity. Backward vertical wind shear with height, encourage breaking. In our case, $\hat{H}$ is difficult to determine due to the decreasing wind speed with height. It has values from 1 to about 5, depending on the altitude. Under these conditions, it is expected that large-amplitude wave breaking may occur. In both the ideal and in the real case simulation, we find overturning of isentropes and a tendency for breaking. We conducted a simulation with uniform flow, 10 ms^{-1}, which gave not signal of breaking. We thus argue that the backed wind shear is a necessity for breaking in our case. Rotation has been regarded as having a hampering effect on breaking, Olafsson and Bougeault (1997) and Barstad and Grønås (2005), however, in the presence of backed wind shear, it does not seem like rotation halts breaking. We looked at the vertical wind shear (500 hPa-1000 hPa) for extended winter months (DJFM) in the Era Interim dataset (Berrisford at al., 2009), and found that backed wind shear happens at 64 % of the days, whereas in summer (JJAS), it happens 46 % of days. This indicates that it is first of all a winter phenomenon.

The results from our observations and simulations indicated similar strengths in the gap jet as those measured and simulated by Sandvik and Furevik (2000). Our observations also revealed some information on the vertical structure of the gap jet. We see that the maximum wind speed is found well above the surface, just at the exit of the gap. It is not expected that ship measurements - like those in Sandvik and Furevik (2000) - will identify the maximum winds in gaps.

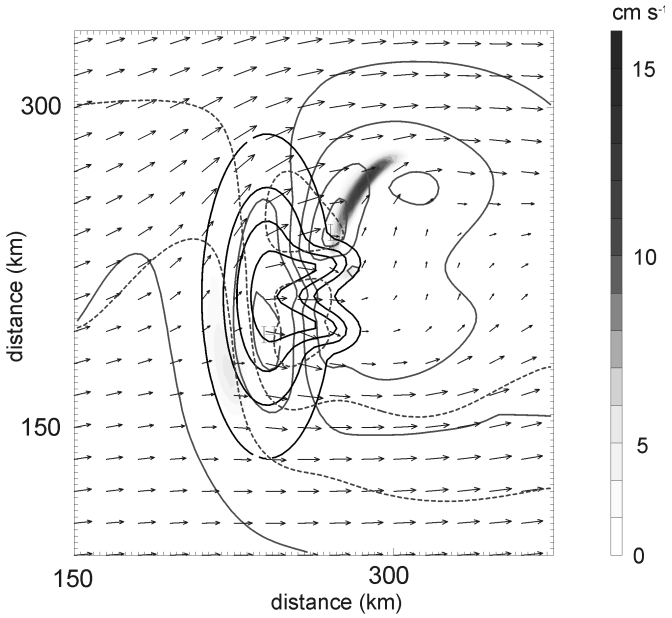

FIGURE 6. a) Characteristics of the flow over an ideal mountain of ~ 1 km height. Solid, black contours, drawn at an interval of 250 m, indicate the topography. A streamer of strong vertical velocity, at a height of 0.5 km, is indicated in black. The association of the streamer with the small scale 'ear' of the mountain is notable. Thin solid lines shows PV with an interval of 0.1 PVU on the 271 K isentropic surface (found at about 500-m height). Broken contours represent the mean sea level pressure, contoured for every 0.5 hPa. Also shown are wind vectors at a height of 0.5 km. Maximum wind speed was found to be ~ 11 ms^{-1}.

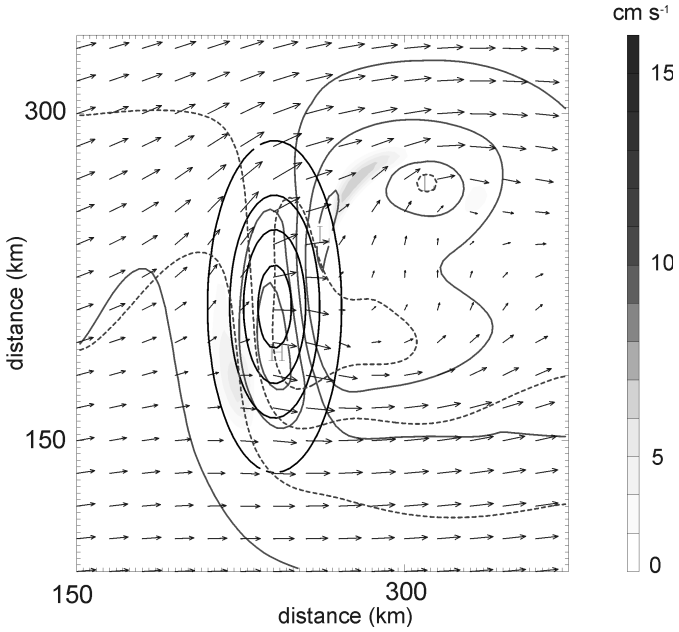

FIGURE 6b: Same as fig. 6a, but for a mountain with no small-scale 'ears'.

4. Summary and conclusions

The paper displays observations of an episode where a slow easterly incoming flow was severely disturbed by the terrain of Svalbard archipelago, resulting in strong local winds. The observations came mainly from the DLR-Falcon (FA20) aircraft which was equipped with wind and water vapour lidars and had dropsonde capabilities. The observations show that the weak upstream winds (5 ms^{-1}) changed into a strong gap flow (20 ms^{-1}) in the Hinlopen Strait. Dropsonde observations and lidar scans documented the gap flow and model simulations with 3 nested domains (9 – 3 - 1 km) reproduce the gap flow in a comforting way. In the lee of the terrain, a wake extended vertically to similar height as the tallest mountain, and this was documented by the wind lidar measurements. Furthermore, small-scale cloud features were identified by the lidar scans and satellite imageries. From model simulations of the wake area, it was argued that these features owe their existence to small-scale terrain disturbances setting up vertical circulations, and that they were maintained by the buoyancy production over the relatively warm ocean further downstream. Moisture fed into the air next to the ocean surface contributed to the moisture content and lead to saturation near the boundary layer top. Based on satellite pictures, these features were seen to trail far downstream – also for easterly winds crossing the archipelago. The implication of these features is unknown, particularly their influence as triggers of disturbances such as polar lows. The investigation also found that backed wind shear with height contributing to wave breaking which led to vertical velocity streamers focused by small-scale terrain. The implication of the rather frequent, backed wind shear with height and associated wave breaking is not well understood.

Acknowledgment

This is the Bjerknes Report no. A313. This research was supported by the Norwegian Research Council's International Polar Year programme through the IPY-THORPEX (175992) and the ArcChange projects. The data acquisition assistance by DLR (lidar and drop sonde) is appreciated. The authors appreciate the Digital Analysis tool (Diana) supported by met.no and fruitful discussions with Prof. Dale Durran. Anna Fitch assisted in editing the manuscript and Prof. Sigbjørn Grønås help with Fig. 3 and provided valuable comments.

References

Armi L. and Mayr G., J., 2007 Continuously stratified flows across an Alpine crest with a pass: Shallow and deep fohn. *Q.J.R. Meteorol. Soc.*, **133**, 459-477

Barstad I., Grønås, S., 2005 Southwesterly flows over southern Norway—mesoscale sensitivity to large-scale wind direction and speed. *Tellus* **57A**,136–152

Barstad I., Grønås S., 2006 Dynamical structures for southwesterly airflow over southern Norway—the role of dissipation. *Tellus*, 58A, 2–18

Barstad I., Kristjansson J.E., Hov Ø., Shapiro M., Irvine E., Dörnbrack A., Probst F., Olafsson H., Storvold R., and Saetra Ø., 2008 The main observational campaign of the IPY-THORPEX-Norway project. Technical report (**R29**), *Bjerknes Centre for Climate Research, University of Bergen, Norway.*

Barstad I., Sorteberg, A., Flatøy, F. Déqué M., 2009 Precipitation, Temperature and Wind in Norway – dynamical downscaling of ERA40. *Clim. Dyn.* 33, 769-776.

Berrisford P, Dee D., Fielding K., Fuentes M., Kallberg P., Kobayashi S. and Uppala S., 2009 The Era-Interim archive. *ERA-report series 1. ECMWF*

Bougeault P , Binder P., Buzzi A., Dirks R., Houze R., Kuettner J., Smith R.B., Steinacker R. and Volkert H., 2001 The MAP Special Observing Period *Bulletin of the American Meteorological Society*, **82**, 433-462

Dudhia, J. 1996 A multi-layer soil temperature model for MM5, Preprint from the Sixth PSU/NCAR Mesoscale Model Users' Workshop

Janjic, Z. I., 1996 The surface layer in the NCEP Eta Model, Eleventh Conference on Numerical Weather Prediction, Norfolk, VA, 19–23 August; Amer. Meteor. Soc., Boston, MA, 354–355

Janjic, Z. I., 2002 Nonsingular Implementation of the Mellor–Yamada Level 2.5 Scheme in the NCEP Meso model, NCEP Office Note, No. 437, 61 pp.

Jiang Q.F., Smith R. B. and Doyle J., 2003 The nature of the mistral: Observations and modelling of two MAP events. *Q. J. R. Meteorol. Soc*, **129**, 857-875

Gabersek S. and Durran D. R. 2004 Gap flows through idealized topography. Part I: Forcing by large-scale winds in the nonrotating limit. *J. Atmos. Sci.* **61**, 2846-2862

Grubisic, V., Smith R. B. and Schär C., 1995 The effect of bottom friction on shallow-water flow past an isolated obstacle. *J. Atmos. Sci.*, **52**, 1985-2005

Hong, S.-Y., Noh Y. and Dudhia, J. 2006 A new vertical diffusion package with an explicit treatment of entrainment processes. *Mon. Wea. Rev.*, **134**, 2318–2341

Kain, J. S., and Fritsch J. M. 1990 A one-dimensional entraining/ detraining plume model and its application in convective parameterization, *J. Atmos. Sci.*, **47**, 2784–2802

Kain, J. S., and Fritsch J. M., 1993 Convective parameterization for mesoscale models: The Kain-Fritcsh scheme, The representation of cumulus convection in numerical models, K. A. Emanuel and D.J. Raymond, Eds., *Amer. Meteor. Soc.*, 246 pp.

Mayr G. J., Armi, Gohm L. A., Zangl G., Durran D. R., Flamant C., Gabersek S., Mobbs S., Ross A. and Weissmann M. 2007 Gap flows: Results from the Mesoscale Alpine Programme. *Q. J. R. Meteorol. Soc.*, **133**, 881-896

Monin, A.S. and Obukhov A. M. 1954 Basic laws of turbulent mixing in the surface layer of the atmosphere. Contrib. *Geophys. Inst. Acad. Sci.*, USSR, (151), 163–187 (in Russian).

Ohigashi O. and G. W. K. Moore, 2009 Fine structures of a Greenland reverse tip jet: a numerical simulation. **67A**, 512-526.

Olafsson H. and Bougeault P. 1997 The effect of rotation and surface friction on orographic drag. *J.Atmos. Sci.* **54**,193-210.

Pan F. F. and Smith R. B. 1999 Gap winds and wakes: SAR observations and numerical simulations. *J Atmos. Sci.* **56**, 905-923

Sandvik A. D. and Furevik B. R., 2000: Case study of a coastal jet at Spitsbergen - Comparison of

SAR- and model-estimated wind. *MWR*, **130**, 1040-1051

Schär, C. and Smith R. B., 1993a Shallow-water passed isolated topography. Part I: Vorticity production and wake formation. *J. Atmos. Sci*. **50**, 1373-1400

Schär, C. and Smith R. B., 1993b Shallow-water passed isolated topography. Part II: Transition ot vortex shedding. *J. Atmos. Sci.*, **50**, 1401-1412

Schär C., Sprenger M., Luthi D., Jiang Q. F., Smith, R. M. and Benoit R. 2003 Structure and dynamics of an Alpine potential-vorticity banner. *Q. J. R. Meteorol. Soc.*, **129B**, 825-855

Schneider T., Held I. M. and Garner S. T., 2003 Boundary effects in potential vorticity dynamics. *J.Atmos.Sci.*, **60**, 1024-1040

Skamarock, W. C., Klemp J. B., Dudhia J., Gill D. O., Barker D. M., Wang W., and Powers J. G., 2005 A description of the Advanced Research WRF Version 2. NCAR Tech Notes-468+STR.

Skeie, P. and Grønås S. 2000 Strongly stratified easterly flows across Spitsbergen. *Tellus*, **52A**, 473-486

Smith, R. B. 1980 Linear theory of stratified hydrostatic flow past an isolated mountain. Tellus, **32**, 348-364.

Smith, R. B., Gleason A.C. and Gluhosky P. A. 1997 The wake of St. Vincent. *J. Atm. Sci.*, **54**, 606-623

Smith, R. B. 1989. Comment on “Low Froude number flow past three- dimensional obstacles. Part I: Baroclinically generated lee vortices” by P. K. Smolarkiewicz and R. Rotunno. *J. Atmos. Sci.* **46**, 3611–3613

Smith, R. B. 2001 Stratified flow over topography. In *Environmental Stratified Flows*, R. Grimshaw, ed., Topics in Environmental Fluid Mechanics, EFMS 3, Boston: Kluwer, 121–159

Smolarkiewicz, P. K. and Rotunno, R. 1989 Low Froude number three-dimensional obstacles. Part I: Baroclinically generated lee vortices. *J. Atmos. Sci.* **46**, 1154–1164

Weissmann, M., R. Busen, A. Dörnbrack, S. Rahm, and O. Reitebuch, 2005. Targeted observations with an airborne wind LIDAR. *J. Atm. Ocean. Technol.*, **22**, 1706-1719

Paper II

3.2 Impacts of the ice-cover and sea-surface temperature on a polar low over the Nordic Seas: A numerical case study

List of authors
Muralidhar Adakudlu and Idar Barstad
Quarterly Journal of Royal Meteorological Society. 2011. **Accepted**.

II

Quarterly Journal of the Royal Meteorological Society *Q. J. R. Meteorol. Soc.* **01: 1–16 (2010)**

Impacts of the ice-cover and sea-surface temperature on a polar low over the Nordic seas: A numerical case study

Muralidhar Adakudlu* and Idar Barstad

Bjerknes Centre for Climate Research, Allégaten-55, Bergen, Norway

*Correspondence to: Muralidhar Adakudlu, Uni Bjerknes Centre, Allégaten-55, NO-5007 Bergen, Norway.
E-mail:Muralidhar.Adakudlu@uni.no

Extreme mesoscale weather in the Arctic region consists mainly of cases with shallow fronts that often form in the vicinity of the ice-edge and intense storms called polar lows. This paper describes high resolution numerical simulations of a severe weather event occurred on 1 March 2008 over the Barents Sea. The event was recorded during the IPY-THORPEX field experiments carried out during February and March, 2008. The numerical simulations indicated the formation of a low pressure system over the Barents Sea on 29 February, 2008 due to baroclinic instability. On 1 March, the surface low moved onto the sea-ice around Spitsbergen and decayed later on. The conditions that prevailed before the dissipation of the surface low were favourable for the formation of a polar low. Two experiments were performed to test the possibilities of triggering a polar low through certain modifications to the surface conditions. In the first experiment, the sea-ice around Spitsbergen was removed. No polar low developed in this case since the static stability was too high. In the second experiment, an attempt to reduce the static stability was made by raising the sea-surface temperature by 5 K. The surface low persisted over the Barents Sea area due to the increased surface heating and led to a strong outbreak of the Arctic air over to the Norwegian Sea on 2 March. The Arctic air outbreak formed a sharp baroclinic zone which was absent in the control simulation. A secondary mesoscale low was triggered near the baroclinic zone over the Norwegian Sea which grew into an intense polar low with the surface winds reaching hurricane force. Formation of the polar low was due to baroclinic instability, whereas convective instability was important during the growth of the low. Copyright © 2010 Royal Meteorological Society

Key Words: Polar low; Arctic Front; static stability; surface fluxes; baroclinic instability; conditional instability of the second kind

Received 20 September 2010; Revised ; Accepted

Citation: . . .

1. Introduction

Polar lows (PL) are violent storms that happen to be one of the most destructive mesoscale weather systems over the North Atlantic Ocean (e.g., Sanders, 1955; Harrold and Browning, 1969; Rasmussen, 1979; Rabbe, 1987; Grønås and Kvamstø, 1995). The fact that the disturbances involved in the formation of PLs are shallow and confined to the boundary layer explains the small scale characteristics of these storms (Mansfield, 1974; Wiin-Nielson, 1989). Accurate forecasting of PLs has been a challenging problem since they are highly sensitive to small-scale processes associated with the boundary layer.

Earlier, PLs were believed to develop due to thermal instability in polar air outbreaks (Dannevig, 1954; Businger and Reed, 1989b). This theory was supported by numerous satellite images that showed the occurrence of convective spiraliform clouds, sometimes with a clear eye at the

center, in many PL developments. However, this theory did not effectively explain the origin and maintenance of the organised cumulus circulation observed around the cyclonic vortex. Økland(1977) and Rasmussen (1977, 1979), assuming a reservoir for convective available potential energy (CAPE), used the theory of the conditional instability of the second kind (CISK) to explain the nature of the organised circulation around the vortex. The existence of the reservoir of CAPE was challenged by Emanuel and Rotunno (1989) who proposed 'wind induced surface heat exchange (WISHE)' mechanism, where the maintenance of the cyclonic vortex was attributed to sensible heat fluxes from the ocean surface.

The necessity of deep, organised convection for the development of PLs was questioned by Harrold and Browning (1969) in a case study of a PL. This PL was characterised by a slantwise convection along a narrow tongue rather than deep cumulus convection, hinting at a baroclinic growth. In the same study, Harrold and Browning discussed a few other PLs that formed in the presence of a low-level temperature gradient concluding that PLs could also be developed due to baroclinic instability. Mansfield (1974) extended the observational study by Harrold and Browning (1969) with a numerical approach. Mansfield applied the normal mode theory for the two PL cases mentioned by Harrold and Browning and showed that the growth rate, wavelength and the phase speed of the PLs are very close to the predictions of the baroclinic theory.

Baroclinic PLs are distinguished from convective-driven PLs by the shape of the cloud patterns associated with the vortex. The latter are characterised by spiraliform cloud bands with convective cells whereas the former are identified by comma-shaped stratiform clouds. Although convection does play a role in the development of comma clouds, it is confined to a narrow tongue and the dominating factor is the barolinicity (Reed and Blier, 1986a).

The role of barotropic instability in the development of PLs has also been the subject of some studies (e.g., Duncan, 1977; Reed, 1979; Mullen, 1979). They all suggested that the barotropic instability has a minor contribution to the genesis of PLs compared to that of barotropic instability and convective instability. However, Rasmussen (1983) and Nagata (1993) suggested that barotropic instability could be the mechanism for the development of meso-beta vortices along boundary layer fronts.

In the case of convective-driven PLs, the cyclonic development was credited to deep convection enhanced by low-level convergence and Ekman pumping. Changes observed at upper-levels during the growth of the cyclone were explained on the basis of the lower-level circulation and surface heating (Rasmussen and Turner, 2003). Concerning the PLs induced by baroclinic instability, the cyclogenesis was attributed to upper-level perturbations superimposed on low-level perturbations. After Hoskins et al. (1985) elaborated the application of isentropic potential vorticity in the diagnosis of the upper-level forcing in the development of synoptic-scale cyclones, the approach has been used in analysing PL developments (Sunde et al., 1994; Røsting et al., 2003; Røsting and Kristjansson, 2006).

Several findings in the past have shown that PLs are highly sensitive to surface conditions, such as the sea-surface temperature and sea-ice distribution (Roch et al., 1991; Albright et al., 1995; Heinemann, 1998). The study by Roch et al. (1991), of a PL formation during 8 - 9 December 1988 in eastern Hudson Bay, reveals that the variation of ice-cover could significantly influence the surface pressure and wind distribution associated with the cyclone. This study was extended by Albright et al., (1995) in order to test the significance of SST and surface fluxes on the PL. In an experiment where SST was raised by 8 K, the strength of the PL increased significantly and wind speed of hurricane force was achieved.

The work presented in this paper is based on numerical simulation of a severe weather situation observed on 1 March, 2008 over the Barents Sea during the IPY-THORPEX field campaign (for a review of the campaign, see Barstad et al., 2008). Unlike the cases described in Roch et al. (1991) and Albright et al. (1995), no PL formed in the case under investigation here, although the conditions observed were favourable for the genesis of a PL. High static stability, due to the presence of sea-ice, could possibly have suppressed the PL development. The objective of the paper is to test if the depression over the Barents Sea can lead into the formation of a PL when the ice-cover and the sea-surface temperature are subjected to certain modifications.

The next section describes the prevailing flow over the Norwegian and the Barents Seas during 29 February$-$1 March, 2008. The experimental set-up for the control and the sensitivity simulations is described in section 3, followed by the results in section 4. Summary and conclusions are given in section 5.

2. Evolution of the flow during 29 February $-$ 1 March 2008

During the early hours of 29 February 2008, north-northeasterly surface winds of strength ~ 12$-$15 ms^{-1} caused a strong outbreak of the Arctic air over the Barents Sea. The Arctic air outbreak is portrayed in Figure 1 showing a NOAA-IR image taken at 1200 UTC, 29 February 2008. Scatterometer wind fields that overlay the NOAA image reflect the strength of the surface wind associated with the outbreak. The outbreak created an Arctic front, which is a shallow zone that separates the cold Arctic airmass from the warm North Atlantic airmass. The Arctic front can be identified in the figure as the leading edge of the Arctic air outbreak. Dense cloud streets behind the Arctic front indicate the cold air advection from the ice-cap. The Arctic front marks the formation of a sharp lower-level baroclinic zone over the Barents Sea.

The frontal circulation was accompanied by a closed isobaric flow as shown by the ECMWF mean sea level pressure contours in the figure. An analysis of the evolution of the surface low pressure system during the next 12$-$18 h indicated a propagation of the surface low onto the ice-edge (see section 4.1 for a detailed explanation). The surface low was found to deepen before propagating across the ice-edge. After crossing over the ice-edge at 0600 UTC, 1 March, the surface low started filling up.

3. Experimental set-up

The Weather Research and Forecasting model (Wang et al., 2008) has been used for the simulations. The horizontal grid length is 9 km and the model has 51 vertical levels up to 50 hPa. The roughness length over the water points varies according to the Charnock relation (Charnock, 1955). Over the ice-cover, the roughness length is fixed at a value

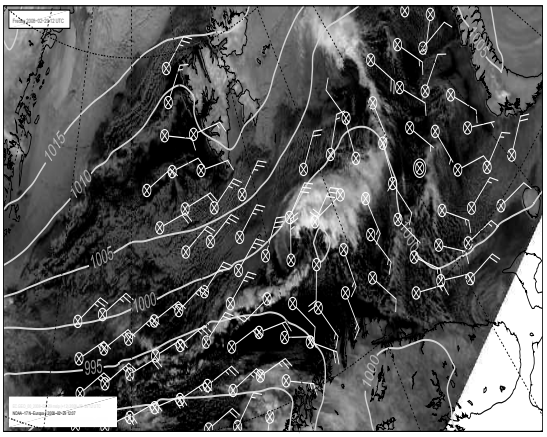

Figure 1. A NOAA-IR image of the Arctic front overlaid by Scatterometer near-surface winds (full barb is equivalent to 5 ms^{-1}) and ECMWF analysis of surface pressure (solid gray contours at every 5 hPa) showing the characteristics of the flow at 1200 UTC, 29 February 2008.

of 1 mm. Computation of surface fluxes of heat, moisture and momentum are based on Monin-Obukhov similarity theory using the stability functions from Paulson (1970), Dyer and Hicks (1970) and Webb (1970). Vertical transport and mixing in the boundary layer are accounted for by using YSU-PBL scheme (Hong and Lim, 2006). Sub-grid scale convective processes and cloud formation are parametrised using the Kain-Fritsch scheme (Kain, 2004) and the microphysical cloud properties are determined through the WSM-6-class scheme (Hong et al., 2004; Dudhia et al., 2008).

In order to validate the model, simulated fields of near-surface winds and mean sea level pressure were compared respectively with the satellite observations and ECMWF analysis. Figure 2 displays the mean sea level pressure and 10 m wind fields as forecasted by the WRF model at 1200 UTC, 29 February 2008. A comparison of Figure 2 and Figure 1 indicates that the 12 h model forecast is close to the observations. Further, predicted vertical profiles of wind, temperature and relative humidity were consistent with the profiles recorded by the DLR-FALCON dropsonde instrument on 1 March 2008 (not shown). This confirms the ability of the WRF model to simulate the flow during 29 February−3 March realistically and its application for the sensitivity experiments.

The initial conditions for the sea-surface temperature (SST) and other prognostic variables were obtained from the ECMWF analysis. Lateral boundaries were updated in the model every 6 h. The model was integrated from 0000 UTC on 29 February to 1800 UTC on 3 March 2008 for all experiments. The experiments were categorised into a *control (CTL)* run and sensitivity runs. The CTL run is a realistic simulation of the conditions between 29 February and 3 March, 2008. Figure 3a illustrates important surface conditions for the CTL run. The sensitivity experiments comprise of two simulations as listed below;

(i) *no-ice (NI)*: the sea-ice around Spitsbergen was removed and the SST was set to 271.5 K in the perturbed area (see Figure 3b);
(ii) *SST5*: the NI case was rerun by increasing the SST at the water points by 5 K (not shown).

These experiments are based on the assumption that the removal of the sea-ice triggers an upward transport of heat, moisture and momentum through surface fluxes. The upward fluxes would in turn result in the reduction of the static stability.

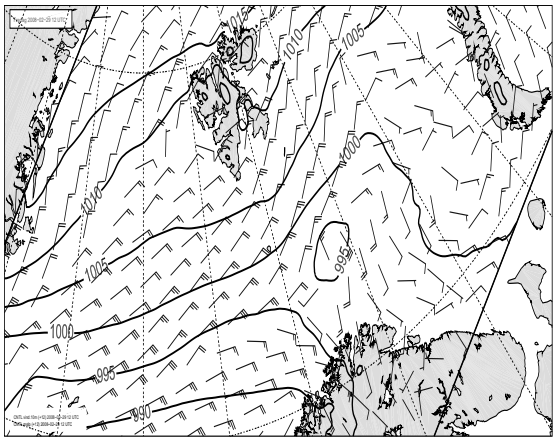

Figure 2. WRF model forecasts (+12 h) of mean sea level pressure (solid contours at every 5 hPa) and 10 m wind (full barb is equivalent to 5 ms^{-1}) valid at 1200 UTC, 29 February 2008.

4. Results

4.1. CTL simulation

Figure 4 illustrates the propagation of the surface low during 29 February−1 March, 2008 as simulated by the model. As can be seen in the figure, the upper-level flow was characterised by a deep vortex at 500 hPa level, located east of Spitsbergen over the sea-ice. A weak trough, associated with the surface low, was discernible over the oceanic side of the 500 hPa vortex. The 500 hPa vortex moved north-westwards, steering the surface low onto the sea-ice on 1 March. The surface low intensified during the time it was situated over the ice-free, relatively warm oceanic surface. Peak intensity was achieved at 0000 UTC, 1 March and was maintained approximately for the next 6 h.

A notable feature of the developments shown in Figure 4 is the apparent influence of the 500 hPa flow on the surface low. The structure of the lower-level baroclinicity during the intensification of the surface low is shown in Figure 5. The density of isolines of equivalent potential temperature at the 925 hPa level is considered here as a measure of the strength of the lower-level baroclinicity. Note the significant strengthening of the lower-level baroclinicity during the intensification. The intensification was accompanied by a decrease in the distance of separation between the 500 hPa vortex and the surface low (MSLP fields have been omitted in the figure for clarity). As the peak intensity is reached at 0000 UTC, 1 March (Figure 5b), the thermal structure in the lower troposphere tends to acquire the shape of a typical occlusion. All the above features are strikingly similar to that of the baroclinic cyclones classified as Type-B systems by Petterson and Smebye (1971). As the surface low crossed the ice-edge and dissipated, the lower-level baroclinicity weakened (not shown).

Possibilities of the convective instability having influenced the motion of the vortex can not be ruled out.

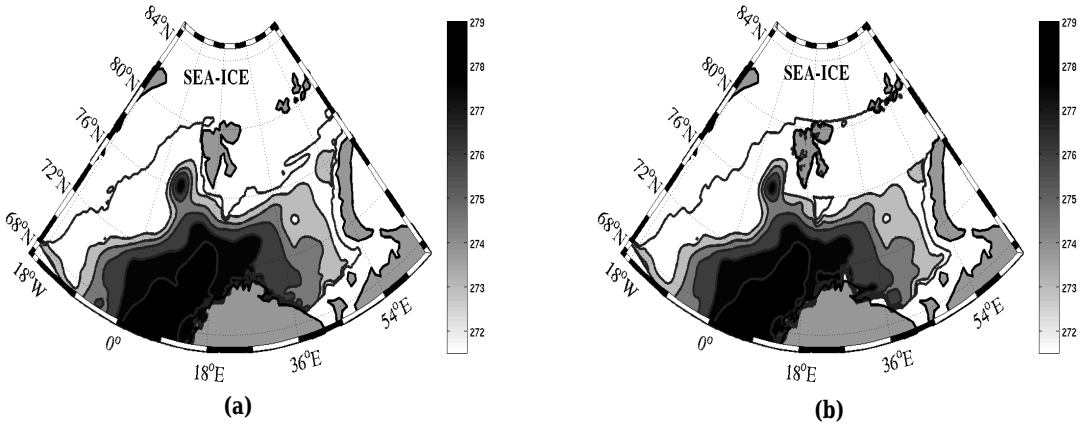

Figure 3. Extent of the sea-ice and magnitude of the SST for (a) the CTL and (b) the NI simulations. The colourbar is valid at the water points only.

Estimation of the degree to which the convective processes might have influenced the developments can be carried out by an analysis of the vertical motion at the steering level (850 hPa in this case), using a simplified form of quasigeostrophic omega equation (Nordeng, 1990) which is given by

$$\nabla^2 S\omega + f^2 \frac{\partial^2 \omega}{\partial p^2} = f \frac{\partial v}{\partial p}.\nabla(f+\zeta) - \nabla^2 H \qquad (1)$$

where H represents the contribution to the vertical motion (ω) from diabatic effects, S refers to static stability and ζ to relative vorticity. $\partial v/\partial p$ denotes the thermal wind. f stands for the Coriolis parameter. The terms on the right-hand side of the above equation represent the ω-forcing due to the advection of relative vorticity with the thermal wind and that due to diabatic effects respectively.

Nordeng (1990) utilised the above relation to diagnose two PLs with similar initial developments but different characteristics during the mature phase. He noticed that, in one of the two developments the vertical motion was forced by the advection of relative vorticity only. But in the case of the second PL, diabatic processes played a significant role that led to a prolonged phase of the PL. Nordeng computed the ω-forcing due to vorticity advection as the ratio of the number of intersection points between the contours of 925−700 hPa thickness and relative vorticity at 850 hPa within the area of strongest upward velocity to the number of grid points in the same area.

We adapted the same approach to diagnose the evolution of ω during 29 February−1 March, 2008. Table-I describes the life-cycle of the surface low between 29 February and 1 March, 2008, in terms of MSLP, maximum relative vorticity and ω associated with the vortex at 850 hPa and adiabatic ω-forcing. The ω-forcing was computed in the same manner as by Nordeng. The table clearly demonstrates the deepening phase of the surface low until 0000 UTC, 1 March and the decaying phase after 1200 UTC, 1 March. Values in the last column indicate that the strength of the ω-forcing decreased gradually after 1200 UTC, 29 February, forcing a similar pattern in ω. Since the adiabatic ω-forcing is directly proportional to the vorticity gradient according to (1), the fall in the ω-forcing can be attributed to a weakening of the relative vorticity gradient. Figure 6 portrays the evolution of relative vorticity at the 850 hPa level on 1 March, 2008. The weakening of the vorticity gradient from 0000 UTC to 0600 UTC is identifiable by comparing Figures 6a and 6b, which confirms the above-mentioned fall in the ω-forcing. Ascending motion ($\omega <$ 0) was discernible on the eastern flank of the surface low, implying that convection was confined to a narrow air column, resembling a baroclinic growth. Moreover, the magnitudes of CAPE hardly exceeded 400 Jkg^{-1} during the life-cycle of the surface vortex (not shown). The moderate values of CAPE required to trigger deep convection and CISK-driven developments being in the range ~ 400−600 Jkg^{-1} (Rasmussen and Turner, 2003; pp 340), the values of CAPE obtained for the 29 February−1 March flow are too low. It is therefore apparent that the motions developed during 29 February−1 March were mostly dominated by baroclinic processes and the convective instability did not have a significant role in the developments.

4.1.1. Conditions favourable for PL development

Two pre-cursors have been considered important in PL forecasting by forecasters; the temperature at the 500 hPa trough and the near-surface wind speed (personal communications with Gunnar Noer, met.no). For a perturbation to grow into a PL, temperature at the 500 hPa level must be less than -40^0C (or SST $-$ T500 $> 45^0$C) and the lower-level wind speed must be greater than 27 knots. Figure 7 shows the simulated temperature at the 500 hPa level at 0000 UTC, 1 March. It can be seen that the temperature at the 500 hPa trough was ~ -44^0C. The near-surface wind speed associated with the surface low exceeded 30 knots at the corresponding time (not shown). Thus, the necessary conditions for the formation of a PL

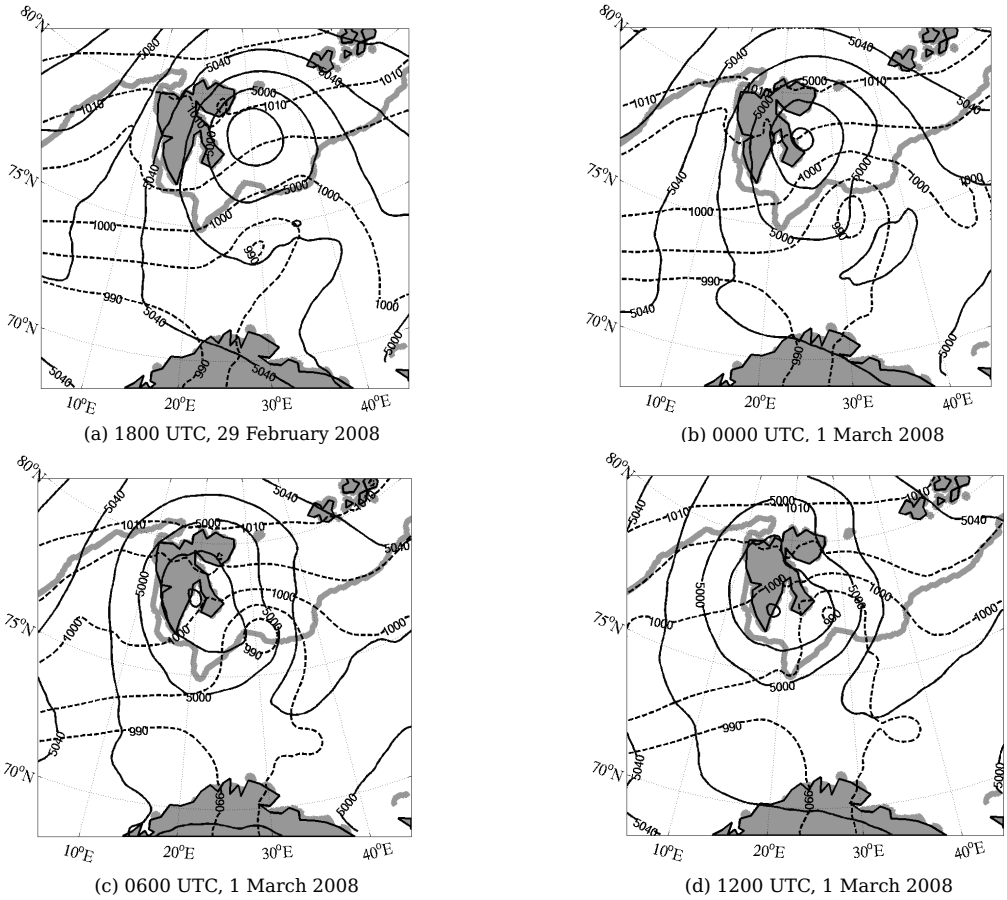

(a) 1800 UTC, 29 February 2008

(b) 0000 UTC, 1 March 2008

(c) 0600 UTC, 1 March 2008

(d) 1200 UTC, 1 March 2008

Figure 4. Simulated evolution of the flow from 29 February to 1 March 2008. Solid contours represent geopotential height at the 500 hPa level (at 20 m interval), and the broken contours represent MSLP (at 5 hPa interval). Thick gray line represents the ice-edge.

seem to be fulfilled as the flow attained the maximum intensity at 0000 UTC, 1 March. However, as described before, no PL development was identified. The possibilities of forcing the formation of a PL were tested through two sensitivity experiments (see section 3 for the description of the sensitivity experiments). The following section presents the results of the sensitivity experiments.

4.2. Sensitivity experiments

4.2.1. The NI simulation

The NI perturbation starts to exert its influence upon the flow after 0600 UTC, 1 March which marks the time when the low pressure system at the surface existed near the ice-edge in the CTL case. Figure 8 shows the flow pattern at 1800 UTC, 1 March 2008 for the NI experiment in comparison with that of the CTL run. The surface low is clearly identifiable in the NI case at 1800 UTC, whereas it is dissipated in the CTL case at this time. Further, the co-existence of the surface low and the 500 hPa vortex along the same vertical axis in the NI case is to be noted. The intensity of the flow remained roughly the same between 0000 UTC and 1800 UTC in the NI case signifying a prolonged phase of the flow at its peak intensity.

Figure 9 portrays the lower-level baroclinicity patterns for both the CTL and the NI conditions when the peak intensity was attained. The figure implies a stronger warm air advection on the eastern flank of the surface low in the NI case (Figure 9a), which can be attributed to the removal of the ice. Figure 10 displays the vertical sections along the lines A-B shown in Figure 9. As evident from Figure 10, the removal of the sea-ice had led to a replacement of the stable boundary layer by an unstable boundary layer. A noteworthy feature is that the inversion that was present in the CTL case is no longer present in the NI case. As a result, the low-level jet which was constrained to the top of the inversion in the CTL case reaches the surface in the NI case leading to an increase in the near-surface wind speed by ~ $3-4$ ms^{-1} (Figure 10a). However, the flow over the unperturbed area (eastern half of the line AB) as well as at the upper-levels remained unchanged. The relatively stronger warm advection at lower-levels in the NI case suppressed the decay of the surface low which resulted in a prolonged phase of the vortex at its peak intensity.

Table I. The life-cycle of the surface low during 29 February−1 March 2008 in the CTL run. The last lines are empty because the low was negligibly weak and was present over the Spitsbergen terrain. The last column is the ratio of the number of intersection points between the 850 hPa relative vorticity contours and thickness (between 925−700 hPa) contours in the area of strongest ω to the number of grid points in the same area.

Time	MSLP (hPa)	Maximum relative vorticity at 850 hPa (x 10^{-4} s^{-1})	Maximum ω at 850 hPa (Pa s^{-1})	Adiabatic ω-forcing at 850 hPa
1200 UTC, 29 February	991	~ 11.9	~ - 14.8	~ 14/14 = 1
1800 UTC, 29 February	989	~ 12.7	~ - 12.3	~ 18/21 = 0.9
0000 UTC, 1 March	986	~ 14.8	~ - 10.2	~ 14/17 = 0.8
0600 UTC, 1 March	986	~ 7.8	~ - 7.7	~ 11/26 = 0.4
1200 UTC, 1 March	988	–	–	–
1800 UTC, 1 March	993	–	–	–

The baroclinic features observed in the CTL case were observed in the NI case as well. The features are;

(i) the reduction in the distance of separation between the upper- and lower-level vortices during the intensification of the flow,
(ii) strengthening of the lower-level baroclinicity, and
(iii) a final structure resembling that of the classical occlusion.

These similarities between the CTL and the NI cases imply that the nature of the growth in the NI case is likely to be baroclinic. Further, an analysis of the evolution of ω for the NI case on 1 March (not shown) on the basis of (1) revealed a similar pattern to that obtained in the case of the CTL simulation. In simple words, the ω-forcing was largely due to adiabatic processes. Thus, like the CTL simulation, the growth mechanism in the NI simulation was baroclinic instability with no significant influences from convective processes. The only distinct feature between the CTL and the NI simulations was a prolonged phase of the surface low in the latter case. The cyclonic circulation in the NI case appears to be weakened after 1800 UTC, 1 March as depicted by the structure of the surface low during the early hours on 2 March, shown in Figure 11. The possibilities for the suppression of the PL development, even when the sea-ice was absent, are explored in the following section using a potential vorticity perspective.

Isentropic potential vorticity (referred to as PV hereafter) fields have proven to be useful in the diagnosis of the upper-level forcing during cyclone developments (for a detailed description of PV, refer to Hoskins et al. 1985), owing mainly to two properties; the conservation of PV in an adiabatic flow and the invertibility principle. For the sake of clarity of the discussions, we rewrite the important relations from Hoskins. The invertibility principle for a frictionless, adiabatic and axisymmetric flow in isentropic coordinates (r, θ) is given by

$$\frac{\partial}{\partial r}\left(\frac{1}{r}\frac{\partial(rv)}{\partial r}\right)+g^{-1}\xi_\theta\frac{\partial}{\partial\theta}\left(\frac{f}{R}\frac{\partial v}{\partial\theta}\right)=\sigma\frac{\partial\xi_\theta}{\partial r} \qquad (2)$$

where v is the horizontal wind field and ξ_θ is the potential vorticity. r is the radial distance from the center of the vortex and θ refers to the potential temperature. g and f have their customary meaning. σ is the density in $xy\theta$ space. R is defined as

$$R(p)=\left(\frac{d\Pi(p)}{dp}\right) \qquad (3)$$

where $\Pi(p)$ is called the Exner function and is given by

$$\Pi(p)=c_p\left(\frac{p}{p_0}\right)^{\kappa} \qquad (4)$$

Equation (2) implies that a particular anomaly in the PV $\xi(r,\theta)$ induces a similar anomaly in the wind field $v(r,\theta)$ or vice-versa. The vertical extent D through which a particular wind anomaly can be induced by the PV anomaly (for the

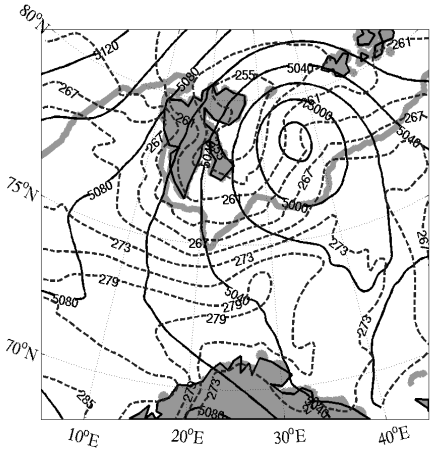

(a) 1200 UTC, 29 February 2008

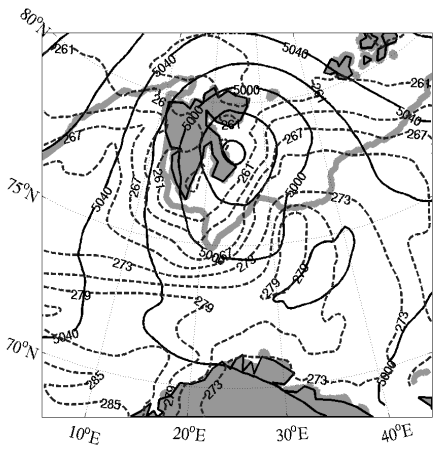

(b) 0000 UTC, 1 March 2008

Figure 5. Evolution of the lower-level baroclinicity during the intensification phase of the surface vortex in the CTL run. Fields shown are 500 hPa geopotential height (solid contours at 20 m interval) and 925 hPa equivalent potential temperature (dashed contours at 3 K interval). Ice-edge is indicated by the thick gray line.

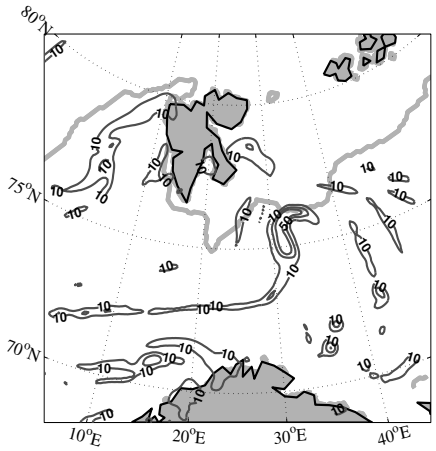

(a) 0000 UTC, 1 March 2008

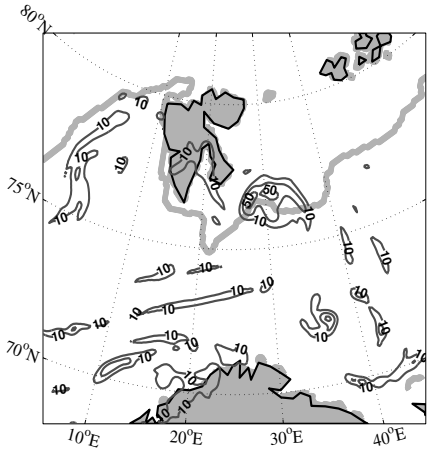

(b) 0600 UTC, 1 March 2008

Figure 6. Evolution of relative vorticity (at 20x10^{-5} s^{-1} interval) at the 850 hPa level on 1 March 2008. The thick gray line represents the ice-edge.

derivation, see Rasmussen and Turner, 2003 in page 365) is given by

$$D \approx \frac{\sqrt{f(f+\zeta_\theta)}L}{N} \tag{5}$$

where ζ_θ is the isentropic relative vorticity, L is the horizontal scale of the PV anomaly and N is the Brunt-Väisälä frequency. (5) is termed as Rossby penetration depth and gives an approximation for the vertical scale of downward penetration of an upper-level PV anomaly.

PLs that are driven by baroclinic instability are often characterised by an upper-level forcing, in the form of shortwave troughs or positive PV anomalies, embedded in the large scale flow (Petterson and Smebye, 1971). The cyclogenesis is enhanced when the upper-level PV anomaly penetrates down to the lower-levels and couples with lower-level perturbations.

We analysed the PV fields associated with the developments in the NI experiment so as to understand the reasons for the possible suppression of a PL. A graphical view of the horizontal and vertical structures of the PV

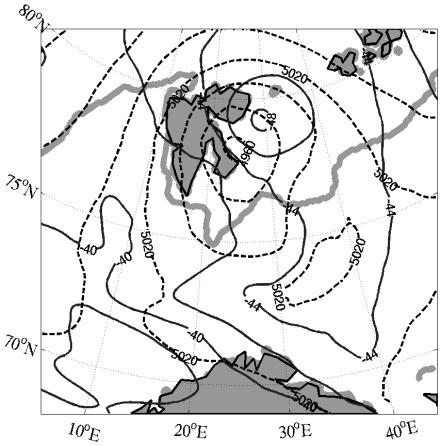

Figure 7. Simulated temperature field (solid contours at 2 ^{0}C intervals) and the geopotential height (dashed contours at 20 m intervals) at the 500 hPa level at 0000 UTC, 1 March 2008.

anomaly on the 290 K isentrope level prior to the dissipation of the surface low is shown in Figure 12. The magnitude of

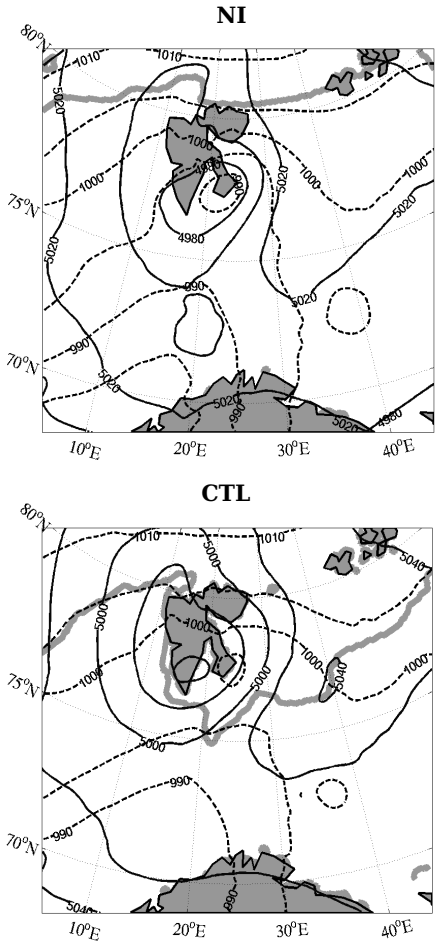

Figure 8. Circulation patterns in the NI and the CTL simulations at 1800 UTC, 1 March 2008. Geopotential height at the 500 hPa level (solid lines at 20 m interval) and MSLP (broken lines at 5 hPa interval) are shown.

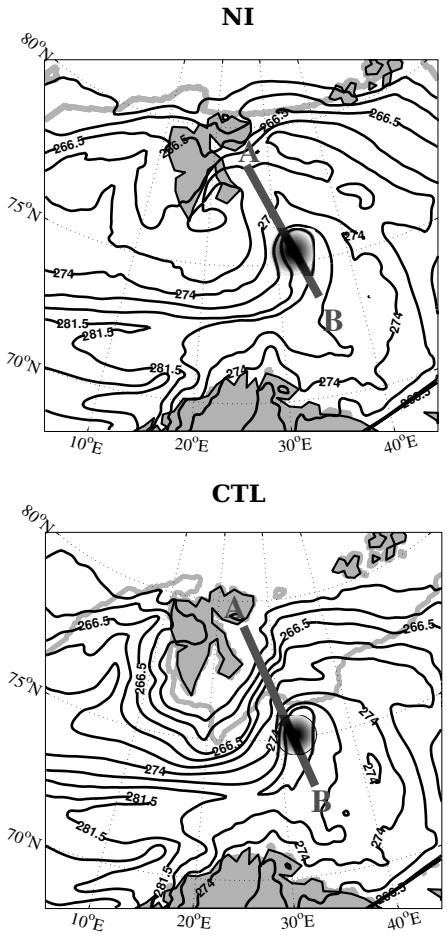

Figure 9. Lower-level baroclinicity as identified at 0000 UTC, 1 March 2008 for the NI and the CTL simulations. The contours represent isolines of equivalent potential temperature at 925 hPa (at 2.5K intervals). The position of the surface low is shaded.

the PV had reached ~ 4 PVU as can be seen in Figure 12a. But the anomaly was confined to the layers above ~ 600 hPa, as depicted by the vertical section across the PV anomaly (Figure 12b).

A quantitative approximation of the penetration depth of the upper-level PV anomaly can be carried out on the basis of (5). As it turns out from Figure 12b, the horizontal scale of the anomaly can be considered to be ~ 100 km. The relative vorticity associated with the upper-level trough on the 290 K isentrope surface was of the order ~ $1.4f$ (the value of f was assumed to be ~ 10^{-4}s^{-1}). Figure 13 shows the vertical profile of the static stability parameter (N) above the surface low and according to the figure, the mean value of N in the troposphere could be taken as ~ 0.0085 s^{-1}. Applying these values of L, N and ζ_θ to (5), we get the Rossby penetration depth as ~ 1.3 km. With such a distance, the upper-level PV anomaly penetrating down to the lower-levels is unlikely. The vertical cross section through the PV field (Figure 12b) clearly reflects this situation. The dissipation of the surface low after 1800 UTC, 1 March could thus be regarded as a direct consequence of the 'non-penetration' of the upper-level forcing to lower-levels. The reason for this could either be a small L, or a low ζ_θ, or high N or a combination of all these factors. One could force the upper-air anomaly to interact with lower-level disturbances by modifying either or all of these parameters. Since it is more simple to alter N, we performed the SST5 experiment wherein the sea-surface temperatures were raised by 5 K at the water points in order to reduce the static stability in the atmosphere. The following section focuses on the results from the SST5 simulation.

4.2.2. The SST5 simulation

Figure 14 shows the simulated surface pressure overlaid by the upper-level flow for the SST5 and the CTL experiments. The flow in the SST5 case exhibited certain striking differences from that in the CTL experiments. The important differences are;

(i) an increase in the intensity of the surface low over the Barents Sea by ~ 10 hPa (980 hPa, as compared with 990 hPa in the CTL case) at 0600 UTC, 1 March (Figure 14a and 14b) and a corresponding increase in the near-surface wind speed (not shown).
(ii) formation of a secondary mesoscale low at the sea-level over the Norwegian sea in association with a

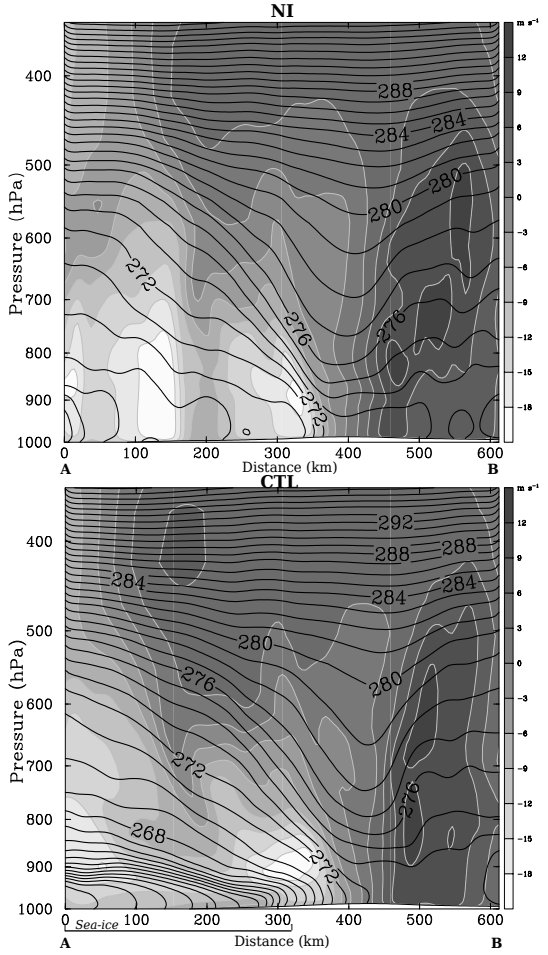

Figure 10. Vertical cross sections along the lines A-B from Figure 9. Solid, black contours represent isentropes (at 1 K interval) and shaded contours indicate wind speed normal to the cross section (negative values indicate the motion out of the cross section and positive values indicate that into the cross section).

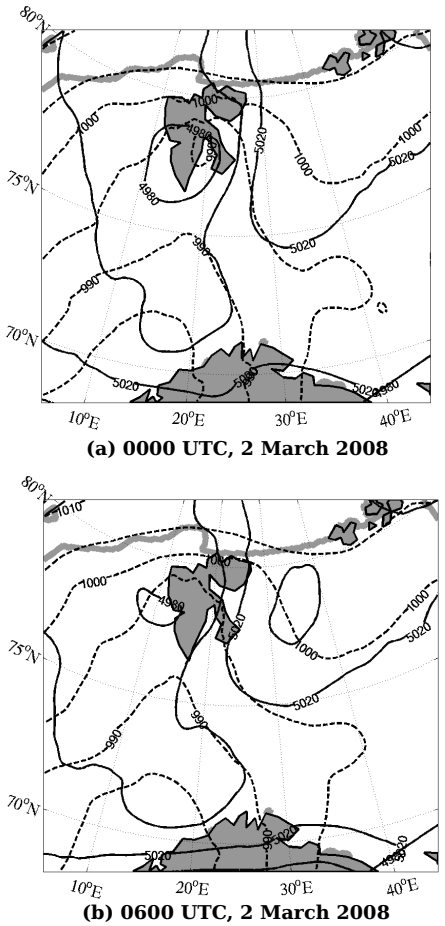

Figure 11. Progress of the surface low on 2 March, 2008 in the NI case. Contour details are same as in Figure 8. A gradual dissipation of the system is evident.

clearly defined trough at 500 hPa level at 0600 UTC, 2 March (marked as 'SL' in Figure 14c), and

(iii) development of an intense PL over the Norwegian Sea 24 h later (Figure 14e).

The surface low which had decayed after 1800 UTC, 1 March in the CTL (and the NI) case persisted over the Barents Sea area in the SST5 case until the secondary low formed over the Norwegian Sea (Figure 14c and d). Figure 15 shows the circulation associated with the Barents Sea low in the SST5 simulation. Formation of the secondary low appears to be a direct outcome of the existence of the Barents Sea low near Spitsbergen. The Barents Sea low steers the Arctic airmass from the ice-cap located further north over to the warm Norwegian Sea, leading to a strong cold air outbreak (Figure 15a). Due to the cold air advection, a baroclinic zone forms over the Norwegian Sea at 0600 UTC, 2 March (Figure 15b). The secondary low was triggered when a trough associated with the 500 hPa vortex forms over the baroclinic zone. The formation of the 500 hPa trough was an outcome of the strong cold air outbreak, since a region of lower-level cold advection has to be associated with a trough in the upper-level flow according to the geopotential tendency equation (see Holton, 2004; pp 157). The Barents Sea vortex propagated south-eastwards after 0600 UTC, 2 March and merged with the secondary low (not shown).

It is important to note that the Barents Sea low neither developed as a PL nor decayed, but persisted over south of Spitsbergen, in the SST5 simulation. This was a necessary condition for the development of the PL over the Norwegian Sea. To confirm this, a test run was performed (not presented in the paper) wherein the sea-surface temperature was raised after 0000 UTC, 2 March. The conditions in the model prior to this time were exactly those in the CTL run at the same time. No PL developed in the test run which implies that the primary reason for the PL development in the SST5 case was the strong cold air advection caused by the Barents Sea low.

Growth mechanism of the PL in the SST5 case: The secondary low over the Norwegian Sea grew into a PL on 2 March most likely because of the stronger convection due to increased surface heating. The upper-level trough intensified into a deep vortex during the evolution of the

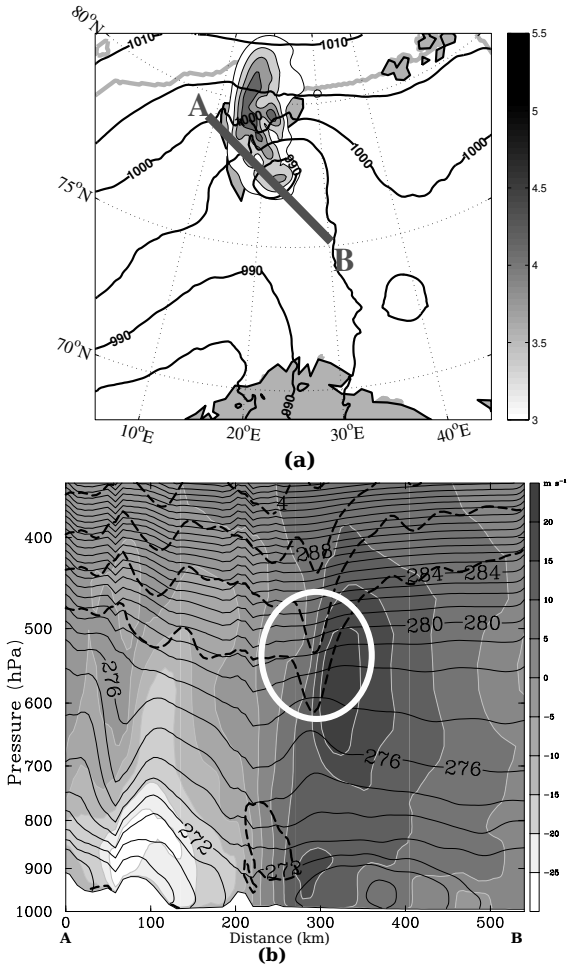

Figure 12. Horizontal and vertical structures of the PV on 290 K isentrope surface at 1800 UTC, 1 March 2008 for the NI case. (a) MSLP (solid contours, at 5 hPa interval) and PV. Area with PV values greater than 3 PVU (1 PVU = 10^{-6}m^{2}s^{-1}Kkg^{-1}) is coloured.(b) isentropes (solid, black contours at 1 K interval), PV (thick, broken contours at 1 PVU interval.) and wind speed normal to the cross section (shaded. Positive values represent the motion into the cross-section and negative contours denote the opposite). The circled area in (b) indicates the positive anomaly in the upper-level PV field.

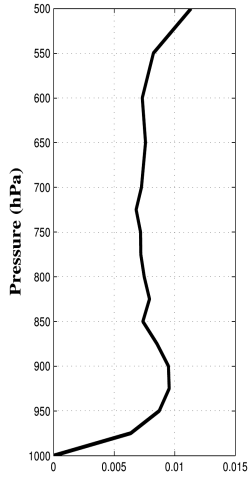

Figure 13. Simulated profile of Brunt-Väisälä frequency (s^{-1}) for the NI experiment above the center of the surface low shown in Figure 12a. The profile is taken at 1800 UTC, 1 March 2008.

PL on 3 March (see Figure 14e). The sea-level pressure at the center of the PL and the surface wind speed had reached ~ 970 hPa and ~ 30 ms^{-1} at 0600 UTC, 3 March respectively. Another notable feature was the intensification of the lower-level front during the development. These features are exactly those that are the characteristics of typical baroclinic cyclones (cf. the features listed in section 4.1). The forcing mechanism for the PL development thus seems to be of a baroclinic nature. However, the surface fluxes tend to be stronger, as the SST is warmer by 5 K in the SST5 simulation. Apparently, the magnitude of the surface fluxes was in the range ~ 1200−1500 Wm^{-2} during the development (cf. ~ 600−800 Wm^{-2} in the CTL and NI cases). Such a phenomenal strengthening of the fluxes would enhance the vertical transport of heat and moisture into the vortex resulting in the increase of the vertical velocity. The heat and moisture transport into the vortex may trigger cumulonimbus convection. The chances of diabatic heating taking over the adiabatic forcing could be expected to increase, as the possibility of the cumulus convection is now higher.

Again, we made use of (1) to test the existence of diabatic forcing during the formation and growth of the PL. Recall that a similar analysis of ω-forcing during 29 February−1 March for the CTL and NI cases showed that baroclinic instability was the dominant mechanism. The situation seems to have changed in the case of the SST5 experiment. Table-II presents the magnitudes of important factors associated with the PL between 2−3 March. Note that the adiabatic ω-forcing was present only at the initial stages of the development. After 1800 UTC, 2 March, although the adiabatic ω-forcing was missing, ω and relative vorticity remained strong as evident from the table. This suggests that the maintenance of vertical motion was due to a diabatic forcing rather than an adiabatic one. We identified condensational heating of an order ~ 25 Kh^{-1} in the region of strong vertical motion during the period 1200 UTC, 2 March and 18 UTC, 3 March. The chances of CISK becoming important are highly likely under the conditions of strong condensational heating. In order for CISK to be significant, CAPE values must either be in the range ~ 400−600 Jkg^{-1} or higher (Rasmussen and Turner, 2003; pp-340). We found that the magnitude of CAPE was in the range ~ 600−900 Jkg^{-1} during 2−3 March (not shown). This can be attributed to the twofold increase in the magnitude of the surface fluxes in the SST5 case. Further, the atmosphere was found to be conditionally unstable up to ~ 500 hPa during 2−3 March (not shown) signifying a deep cumulonimbus convection during the growth of the PL. Hypothetically, the latent heat released in the cumulonimbus clouds forms a circulation cell with upper-level divergence and lower-level convergence. The convergence of moisture in the boundary layer strengthens the vertical motion which in turn would increase the vorticity associated with the vortex through vortex stretching. This is reflected by the strong values of ω and relative vorticity seen on 3 March (see table-II). The vertical motion being strengthened in this manner, cumulus convection was enhanced and a positive feedback loop between the cloud field and the vortex was established, which resulted in the intensification of the PL on 3 March.

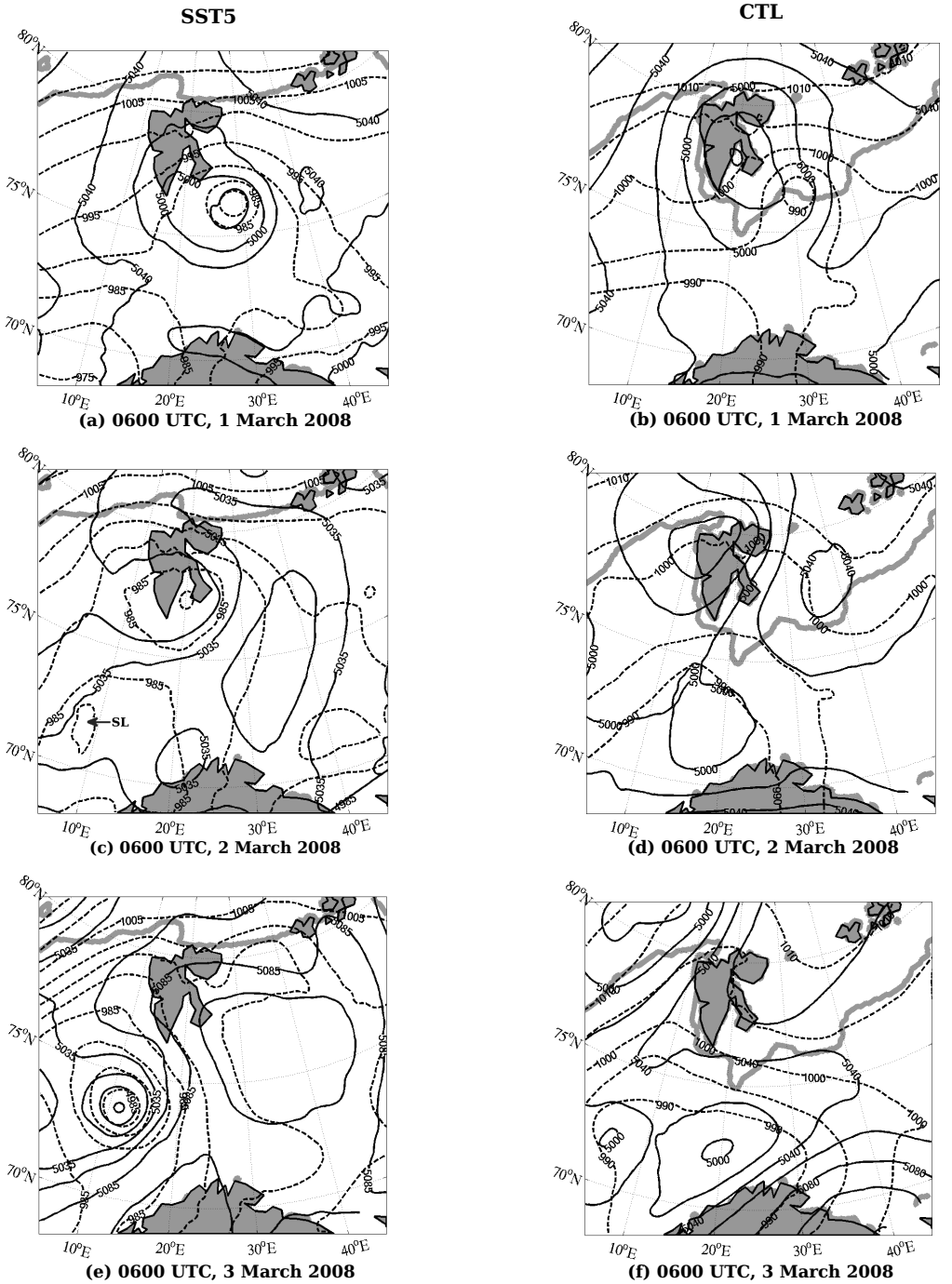

Figure 14. Surface and 500 hPa flow characteristics for the SST5 and CTL experiments. Dashed contours represent MSLP (at 5 hPa interval) and solid contours represent 500 hPa geopotential height (at 20 m interval). The mark 'SL' in (c) means 'secondary low'.

Given the above conditions, it is sensible to consider that CISK was indeed important for the growth of the PL, although the triggering mechanism was of a baroclinic nature. The baroclinic instability can be considered to have provided the necessary initial disturbance during the early hours on 2 March.

To summarise the growth mechanism of the PL, baroclinic instability seems to have played an important role in the formation of the low. Significant values of CAPE being present during the growth of the low, CISK took over the baroclinic forcing on 3 March.

General characteristics of the PL: The PL that grew on 3 March due to the SST perturbations had two distinct

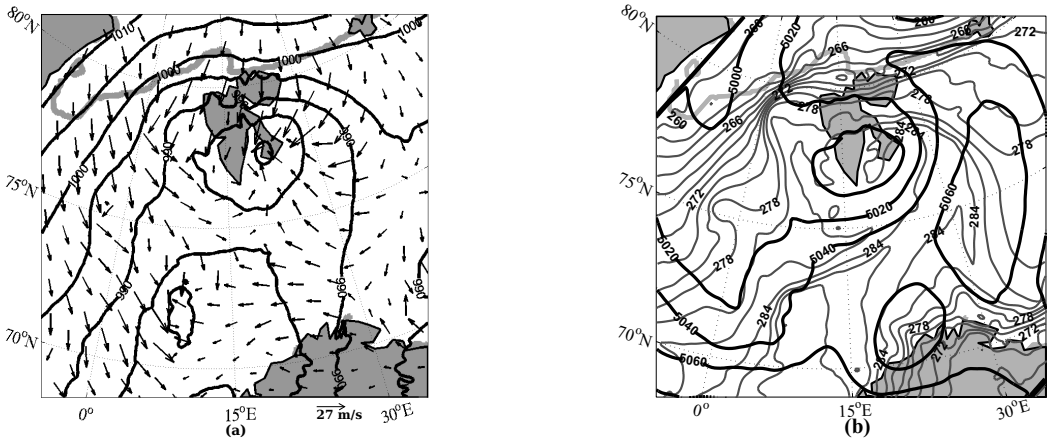

Figure 15. The formation of the secondary low at 0600 UTC, 2 March in SST5 simulation. (a) Mean sea level pressure (solid contours at 5 hPa interval) and 10 m wind vectors, and (b) equivalent potential temperature at the 925 hPa level (solid gray contours at 2 K interval) and geopotential height at the 500 hPa level (solid black contours at 20 m interval). Thick, light gray contour near Spitsbergen indicates the ice-edge.

phases; a development phase and a mature phase. The development phase was observed from 0600 UTC, 2 March to 0000 UTC, 3 March and the mature phase from 0000 UTC, 3 March to 1800 UTC, 3 March. In this section, we shall describe the important features of the PL in each of the above phases.

Development phase: Intensification of the 500 hPa trough and the low pressure area at the surface are the important characteristics observed in the development phase. Figures 16 and 17 clearly demonstrate these characteristics. During the development phase, the cyclonic vortex was positioned approximately at the same location (Figures 16a and 17a). The surface low (the secondary low over the Norwegian Sea) deepens by ~ 10 hPa (from 980 hPa to 970 hPa) and the 500 hPa trough turns into a deep vortex during this phase, indicating a rapid intensification of the cyclonic vortex. As can be seen in the vertical sections across the surface low (Figures 16b and 17b), a PV anomaly is induced at the lower-levels as the secondary low formed at 0600 UTC, 2 March. When the peak intensity was attained at 0000 UTC, 3 March, both the upper- and lower-level PV anomalies intensify and show a tendency for coupling. An increase in the near-surface wind speed from ~ 8 ms^{-1} to ~ 30 ms^{-1} (on the south-western flank of the low) is also discernible in the vertical plots. The mature phase begins when the cyclonic vortex reaches its peak intensity i.e., at 0000 UTC, 3 March. It is reasonable to assert that the cyclonic vortex had turned into a PL around this time.

We carried out a quantitative analysis of the Rossby penetration depth (relation (5)) of the upper-level PV anomaly prior to the formation of the PL, ie., at 1800 UTC, 2 March. Table-III gives an overview of the magnitudes of the parameters of (5), i.e., the horizontal scale of the upper-level PV anomaly (L), the relative vorticity at 290 K isentrope level (ζ_θ), the static stability parameter (N), and the Rossby penetration depth (D) for SST5 case. In addition, the table also gives the magnitudes of the above parameters for the CTL and the NI case. The values in the cases of the CTL and the NI simulations correspond to the Barents Sea low respectively at 0000 UTC and 1800 UTC, 1 March. Around these times, the Barents Sea low was at its peak intensity before the dissipation took place in those cases. For the SST5 case, the values presented in the table correspond to the developing secondary low over the Norwegian Sea at 1800 UTC, 2 March, which marks the time prior to the formation of the PL. The table reveals that the Rossby penetration depth obtained in the cases of CTL and NI simulations was of the order ~ 1 km before the vortex decayed. However, in the SST5 simulation, a penetration depth of the order ~ 5 km was obtained at 1800 UTC, 2 March followed by the formation of the PL. This implies that the dynamical reason for the PL genesis in the SST5 case was the vertical coupling of the upper-level PV anomaly which was absent in the CTL and the NI simulations.

It is apparent from the table that the vertical coupling was achieved in the SST5 case due to a combination of high L, strong ζ_θ, and low N with respect to that in the CTL and the NI cases. However, the major contribution for the deeper penetration D of the upper-level forcing seems to be from the high ζ_θ in the SST5 simulation. Such a strengthening in the upper-level relative vorticity could be attributed to the intensification of the upper-level trough (see Figure 14c) into a cyclonic flow around 1800 UTC on 2 March. As mentioned before, the formation of the upper-level trough was due to the strong cold air outbreak in the SST5 simulation. As the cold air was advected over to the warm Norwegian Sea, strong upward fluxes caused a decrease in the static stability which further favoured a deeper penetration of the upper-level forcing. The cyclogenesis was in this way enhanced and a vertical coupling between the upper- and lower-level features was achieved followed by the formation of the PL at 0000 UTC, 3 March over the Norwegian Sea. Concerning the CTL and the NI runs, although an upper-level trough was seen in association with the Barents Sea low, there was no intensification of the trough which resulted in low values of relative vorticity. Further, the static stability in these two cases being relatively higher than that in the SST5 case, the penetration depth of the upper-level anomaly was low which forced the suppression of the surface low.

Table II. Evolution of the vertical motion and relative vorticity during the genesis and growth of the PL during 2−3 March 2008 in the SST5 simulation. The values in the last column were determined in the same manner as for the CTL simulation in Table-I.

Time	MSLP (hPa)	Maximum relative vorticity at 850 hPa (x 10^{-4} s^{-1})	Maximum ω at 850 hPa (Pa s^{-1})	Adiabatic ω-forcing at 850 hPa
0000 UTC, 2 March	985	~ 12.6	~ - 14.8	–
0600 UTC, 2 March	978	~ 17.3	~ - 21.3	~ 4/3 = 0.9
1200 UTC, 2 March	977	~ 17.8	~ - 17.5	~ 2/2 = 1
1800 UTC, 2 March	972	~ 20.1	~ - 14.5	–
0000 UTC, 3 March	968	~ 16.6	~ - 12.1	–
0600 UTC, 3 March	965	~ 14.4	~ - 11.8	–
1200 UTC, 3 March	965	~ 18.2	~ - 15.8	–
1800 UTC, 3 March	967	~ 16.0	~ - 15.2	–

Mature phase: The striking difference between the development phase and the mature phase of the PL was that in the former, the PL was situated at the same location. There was rapid deepening of the surface vortex and increase in the surface wind speed in the development phase. In the mature phase, the PL was seen propagating north-westwards after it was formed at 0000 UTC, 3 March. Figure 18 portrays the horizontal and the vertical structure of the PL in the mature phase. From a comparison between Figures 17a and 18a, the distance covered by the PL appears to be ~ 500 km in a time span of 18 h. Apparently, the surface wind speed and the strength of the vortex was roughly constant during this time span (see Figures 17b and 18b). These vertical plots also indicate a strong coupling between the upper- and lower-level PV anomalies. The PV-coupling favoured the growth of the PL on 3 March.

5. Summary and conclusions

The numerical simulations of a severe Arctic event recorded on 1 March 2008 during the IPY-THORPEX field campaign over the Norwegian and the Barents Sea area have been described. The control (CTL) simulation was in good agreement with the DLR-FALCON observations recorded during the campaign. The simulation indicated a low pressure area being developed in the Barents Sea early on 29 February 2008 through baroclinic instability. The conditions associated with this low pressure system were favourable for the formation of a polar low (PL). However, the depression moved over the ice-covered area near Spitsbergen after 0600 UTC, 1 March and decayed later on, due to the strong static stability over the sea-ice. Two experiments were performed with the objective of exploring if the depression that decayed in the CTL run can lead to the development of a PL. The experiments are; i) the no-ice (NI) experiment in which the sea-ice around Spitsbergen was removed and the surface temperature was raised to the freezing level of sea-ice, and ii) the SST5 experiment wherein the sea-surface temperatures at the water points were raised by 5 K above the freezing level.

The surface low persisted for a longer duration (~ 12 h) in the NI simulation, essentially due to the removal of the sea-ice, before being dissipated after 1800 UTC, 1 March. The influence of the NI perturbation was confined only to the boundary layer over the ice-free area. Since the upper-level flow was not influenced by the removal of sea-ice, sufficient penetration of the upper-level PV anomaly to lower-levels was not achieved, resulting in a gradual dissipation of the system. When the NI simulation was rerun with an increased sea-surface temperature (i.e., the SST5 simulation), a secondary cyclone formed at 0600 UTC on 2 March on the Norwegian Sea. The primary reason for the formation of the secondary low was baroclinic instability in the frontal zone created by a strong Arctic air outbreak from the ice-cap. The Arctic outbreak was triggered by the disturbance existing over the Barents Sea near Spitsbergen. The secondary low intensified into a PL later on. The formation of the PL and its growth could be attributed to a reduction in the static stability and a considerable intensification of the upper-level relative vorticity that

Table III. Magnitudes of the parameters of the relation (5) for the control and the sensitivity experiments. The time levels correspond to the time at which the peak intensity was achieved in the case of CTL and NI simulations. In the case of SST5 simulation, it corresponds to the time prior to the formation of the PL. The value of the Coriolis parameter (f) is ~ 1×10^{-4} s^{-1}.

Exp.	Time	L (km)	ζ_θ (s^{-1})	N (s^{-1})	D (km)
CTL	0000 UTC 1 March	~ 90	~ 0.6ƒ	~ 0.0087	~ 0.8
NI	1800 UTC 1 March	~ 100	~ 1.4ƒ	~ 0.0085	~ 1.3
SST5	1800 UTC 2 March	~160	~ 5ƒ	~ 0.007	~ 5.1

caused a coupling between the upper- and lower-level features. An analysis of the evolution of the vertical motion during the development of the PL indicated that the triggering mechanism was most likely of a baroclinic nature. CISK gradually took over the baroclinic instability during the growth of the PL.

The dissolution of an adverse weather situation in the CTL simulation and the same situation leading to the formation of an intense PL in the SST5 simulation reflect the impacts of surface parameters on the extreme cases in the Arctic. An important finding of this paper is the sensitivity of upper-level features to the surface conditions. Neither the CTL nor the NI simulation show a penetration of the upper-level forcing to the lower-levels whereas the SST5 simulation does indicate a strong vertical coupling. However, this result is not sufficient to claim that increased surface heating alone can cause a downward penetration of upper-level features. Low static stability and/or strong baroclinicity may also lead to such situations. Hence, a detailed analysis of the relative significance of different physical factors in the genesis of PLs becomes important. Such an assessment was not a part of this study. Given the complexity of the real atmosphere, sophisticated tools would be required to address such issues. However, high-resolution idealised experiments, specifically aimed at PLs, may provide a relatively simple platform for the assessment of individual processes involved in the genesis of PLs.

Acknowledgements

This is publication no. XXXX from the Bjerknes Centre for Climate Research. The research was funded by the Norwegian Research Council's Arc-Change project which is a part of the International Polar Year (IPY) programme. We are grateful to Dr. Nils Gunnar Kvamstø and Dr. Jü rgen Bader for the useful discussions and constructive comments.

References

Albright MD, Reed RJ and Ovens DW. 1995. Origin and structure of a numerically simulated polar low over Hudson Bay. *Tellus* **47A**: 834-848

Barstad I, Kristjansson JE, Hov Ø, Shapiro M, Irvine E, Dörnbrack A, Probst F, Ólafsson H, Storvold R, Sætra Ø. 2008. The main observational campaign of the IPY-THORPEX-NORWAY project. *Technical report R29*. Bjerknes Centre for Climate Research. (`http://www.uib.no/People/ngfib/R29.pdf`)

Businger S, Reed RJ. 1989b. Polar lows. In Polar and Arctic Lows, ed. P.F. Twitchell, E. Rasmussen and K.L. Davidson. pp. 3-45. A Deepak, Hampton, VA

Charnock H. 1955. Wind stress over a water surface. *Quart. J. Roy. Met. Soc*. **81**: 630-640.

Dannevig P. 1954. *Meteorologi for Flygere (in Norwegian)*. Aschehoug, Oslo

Dudhia J, Hong SY and Lim KS. 2008. A new method for representing mixed-phase particle fall speeds in bulk microphysics parametrisation. *J. Met. Soc. Japan*. in press.

Duncan CN. 1977. A numerical investigation of polar lows. *Quart. J. Roy. Met. Soc*. **103**: 255-68.

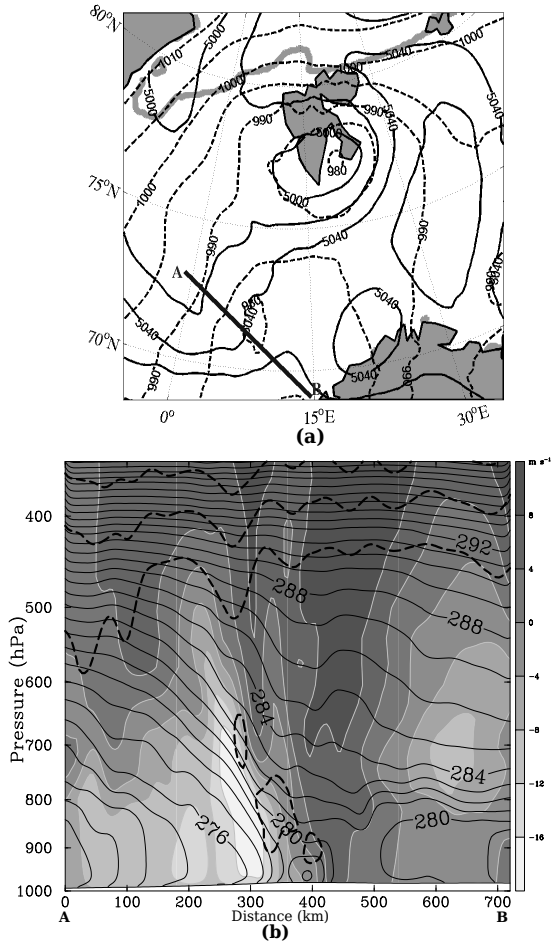

Figure 16. Horizontal and vertical cross sections of the secondary low at 0600 UTC, 2 March 2008. Contour details of (a) and (b) are same as in Figures 14 and 12b respectively.

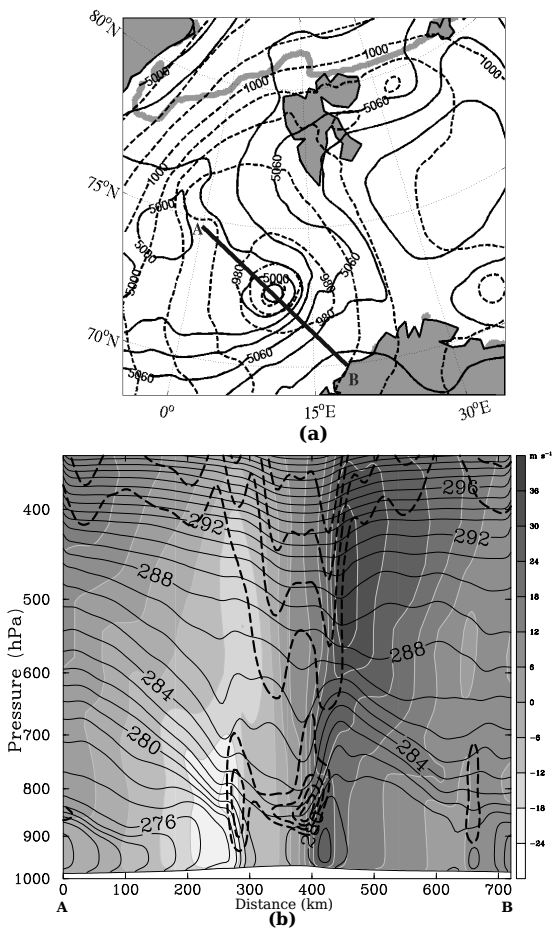

Figure 17. Same as Figure 16, but at 0000 UTC, 3 March.

Dyer AJ and Hicks BB. 1970. Flux-gradient relationships in the constant flux layer. *Quart. J. Roy. Met. Soc*. **96**: 715-721.

Emanuel KA and Rotunno R. 1989. Polar lows as arctic hurricanes. *Tellus* **41A**: 1-17.

Grønås S and Kvamstø NG. 1995. Numerical simulations of the synoptic conditions and development of Arctic outbreak polar lows. *Tellus* **47A**: 797-814.

Harrold TW and Browning KA. 1969. The polar lows as a baroclinic disturbance. *Quart. J. Roy. Met. Soc*. **95**: 710-23.

Heinemann G. 1998. A mesoscale model-based study of the dynamics of a wintertime polar low in the Weddel Sea region of the Antarctic during the Winter Weddel Sea Program field phase 1986. *J. Geophys. Res*, **103**, 5983-6000.

Holton JR. 2004. An Introduction to Dynamic Meteorology.(4^{th} edn). Elsevier Academic press.

Hong SY, Dudhia J and Chen SH. 2004. A Revised Approach to Ice Microphysical Processes for the Bulk Parametrisation of Clouds and Precipitation. *Mon. Wea. Rev*. **132**: 103-120.

Hong SY and Lim JOJ. 2006. The WRF Single-Moment 6-Class Microphysics Scheme (WSM6). *J. Korean Meteor. Soc*. **42**: 129-151.

Hoskins BJ, McIntyre ME and Robertson AW. 1985. On the use and significance of isentropic potential vorticity maps. *Quart. J. Roy. Met. Soc*. **111**: 877-946.

Kain JS. 2004. The Kain-Fritsch convective parametrisation: An update. *J. Appl. Meteor*. **43**: 170-181.

Mansfield DA. 1974. Polar lows: the development of baroclinic disturbances in cold air outbreaks. *Quart. J. Roy. Met. Soc*. **100**: 541-54.

Mullen SL. 1979. An investigation of small synoptic cyclones in polar air streams. *Mon. Wea. Rev*. **107**: 1636-47.

Nagata M. 1993. Meso-alpha-scale vortices developing along the Japan Sea polar airmass convergence zone cloud band: Numerical simulation. *J. Met. Soc. Jap*. **71**: 43-57.

Nordeng TE. 1990. A model based diagnostics study of the development and maintenance of two polar lows. *Tellus **42A***. 92-108.

Økland H. 1977. On the intensification of small scale cyclones formed in very cold airmasses heated over the ocean. *Institute report series NO. 26*. Institutt for Geofysikk, Universitet, Oslo.

Paulson CA. 1970. The mathematical representation of wind speed and temperature profiles in the unstable atmospheric surface layer. *J. Appl. Meteor*. **9**: 857-861.

Petterson S and Smebye SJ. 1971. On the development of extratropical cyclones. *Quart. J. Roy. Met. Soc*. **97**: 457-82.

Rabbe A. 1987. A polar low over the Norwegian Sea, 29 February - 1 March 1984. *Tellus* **39A**: 326-33.

Rasmussen E. 1977. The polar low as a CISK phenomena. *University of Copenhagen, Institute for Theoretical Meteorology, Copenhagen*.

Rasmussen E. 1979. The polar low as an extratropical CISK disturbance. *Quart. J. Roy. Met. Soc*. **105**: 531-49.

Rasmussen E. 1983. A review of meso-scale disturbances in cold air masses. In Mesoscale Meteorology - Theories, Observations and Models, ed. D. K. Lilly and T. Gal-Chen, pp. 247-83. D Reidel,

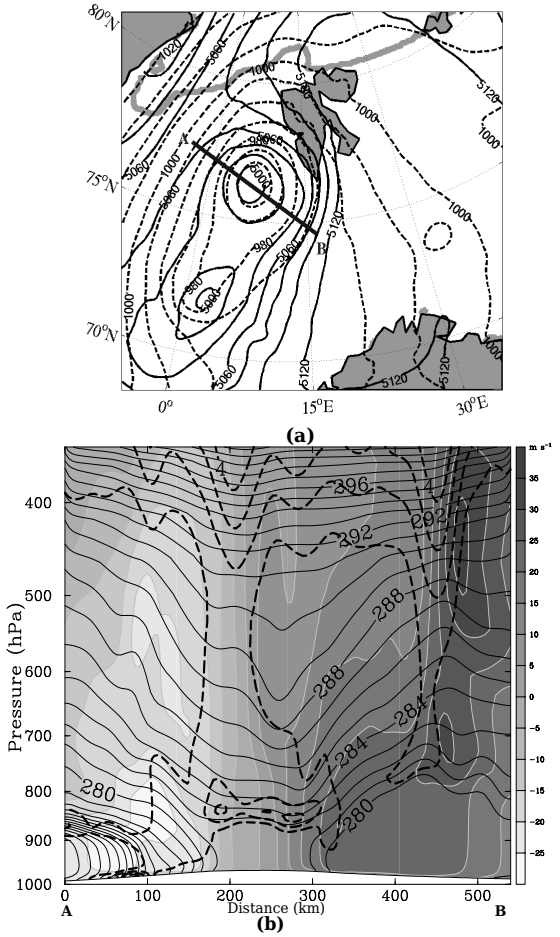

Figure 18. Same as Figure 17, but at 1800 UTC, 3 March.

Boston.

Rasmussen E and Turner J. 2003. Polar lows - Mesoscale weather systems in polar regions. (1^{st} edn). Cambridge University press

Reed RJ. 1979. Cyclogenesis in polar airstreams. *Mon. Wea. Rev.* **107**: 38-52.

Reed RJ and Blier W. 1986a. A case study of a comma cloud development in the Eastern Pacific. *Mon. Wea. Rev*. **114**: 1681-95.

Roch M, Benoit R and Parker N. 1991. Sensitivity experiments for polar low forecasting with the CMC mesoscale finite-element model. *Atmos.-Ocean.*. **29**: 381-419.

Røsting B, Kristjansson JE and Sunde J. 2003. The sensitivity of numerical simulations to initial modifications of potential vorticity - a case-study. *Quart. J. Roy. Met. Soc*. **129**: 2697-2718.

Røsting B and Kristjansson JE. 2006. Improving simulations of severe winter storms by initial modification of potential vorticity in sensitive regions. *Quart. J. Roy. Met. Soc*. **132**: 2625-2652.

Rummukainen M, Bergström S, Persson G, Rodhe J. and Tjernström M. 2004. The Swedish regional climate modelling programme, SWECLIM; A review. Ambio, **33**: 176-182.

Sanders F. 1955. An investigation of the structure and dynamics of an intense surface frontal zone. *J. of Meteorology*. **12**: 542-552.

Sardie JM and Warner TT. 1985. A numerical study of the development mechanism of polar lows. *Tellus* **37A**: 460-77.

Sunde J, Røsting B, Breivik LA, Midtbø KH and Ulstad C. 1994. Operational monitoring and forecasting of mesoscale weather phenomena in ocean regions surrounding *Norway. Met. Apps*. **1**: 237-45.

Wang W, Barker D, Bruyere C, Duda M, Dudhia J, Gill D, Michalakes J, and Rizvi S. 2008. WRF Version 3 Modeling System User's Guide. (`http://www.mmm.ucar.edu/wrf/users/docs/arw_v3.pdf`)

Webb EK. 1970. Profile relationships: The log-linear range, and extension to strong stability. *Quart. J. Roy. Met. Soc*. **96**: 67-90.

Wiin-Nielsen. 1989. On the precursors of polar lows. In *Polar and Arctic lows*. ed. P. F. Twitchell, E. Rasmussen and K. L. Davidson. pp. 85-107. A Deepak, Hampton, VA.

Paper III

3.3 Impacts of different initial conditions on the growth of polar lows: Idealised baroclinic channel experiments

List of authors
Muralidhar Adakudlu
Quarterly Journal of Royal Meteorological Society. 2011. **In review**.

III

Quarterly Journal of the Royal Meteorological Society *Q. J. R. Meteorol. Soc.* **01: 1–20 (2011)**

Impacts of different initial conditions on the growth of polar lows: idealised baroclinic channel experiments

Muralidhar Adakudlu*
Uni Bjerknes Centre, Allégaten-70, University of Bergen, Bergen, Norway

Development of polar lows is simulated in an ideal baroclinic channel with the objective of studying the sensitivity of polar lows to different initial conditions. The basic state in the channel has a baroclinic jet at the tropopause level superposed by a finite amplitude perturbation in the form of potential vorticity anomalies. This upper-level perturbation induces baroclinic instability in the channel thereby leading to the genesis of polar lows. The polar lows evolve through a development phase and a mature phase during their growth. The development phase is characterised by strong vertical motion and a rapid intensification of the polar lows whereas the magnitude of the vertical motion drops and the growth slows down in the mature phase. The vertical motion is simultaneously forced by the adiabatic and diabatic ω-forcing terms in the quasi-geostrophic ω-equation. The degree of baroclinicity, static stability, surface heating and the scale of the upper-level anomaly were each modified separately in a series of sensitivity experiments to investigate the relative influence of these parameters on the features of a polar low developed under the control conditions. It is shown that, while the pattern of vertical motion associated with the polar low is most sensitive to the amount of baroclinicity and surface heating, the growth rate of the polar low is most sensitive to the static stability inherent in the initial conditions. The scale of the upper-level anomaly seems to have profound impacts on the scale and structure of the polar low. In all the sensitivity experiments, the formation of the polar low gets delayed and its intensity, in terms of the surface pressure, reduced due to the modified initial conditions. The reduced intensity suppresses the tendency for a vertical coupling of upper- and lower-level features of the polar low. Copyright © 2011 Royal Meteorological Society

Key Words: Polar low; baroclinic instability; static stability; ideal baroclinic channel; potential vorticity coupling

Received ; Revised ; Accepted

Citation: . . .

1. Introduction

Polar lows (PL) are intense storms of mesoscale structure that form over high latitudes poleward of the main polar front in cold seasons. These storms are among the most hazardous weather events over the North Atlantic and the Arctic region. The primary cause for the development of PLs is the strong air-sea interaction triggered during the outbreak of cold airmass from the Arctic ice-cap over to the relatively warm ocean basins. PLs owe their mesoscale nature to the shallowness of the cold airmasses (~ $1-2$ km in depth) advecting from the ice-cover (Mansfield, 1974; Wiin-Nielsen, 1989). Due to the small temporal and spatial scale and the adverse weather associated with PLs, accurate forecasting of these storms has been a major challenge.

On the physical mechanism governing the formation and growth of PLs, several theories have been formulated. Initially, PLs were believed to form through thermal instability within polar airmasses advecting over a warm

sea (Meteorological Office, 1962). However, in a case study of a PL, Harrold and Browning (1969), observed a stable ascent of air along a narrow tongue rather than deep, cumulus convection. Convection along narrow air columns symbolizes the conversion of potential energy available in shallow baroclinic zones into kinetic energy with which baroclinic instability grows. In the same study, Harrold and Browning gave examples of a few other cases wherein PL development was associated with low-level baroclinic zones and concluded that PLs are baroclinic disturbances. Mansfield (1974) supported this view in his theoretical work which essentially was an extension of the Harrold and Browning case. He used the model of Eady (1949) to obtain the values for phase speed, wavelength and the growth rate associated with the PL of Harrold and Browning (1969). The study showed that the theoretical values were comparable with the observed values which prompted Manfield to suggest that baroclinic instability can explain the structure and energetics of PLs. Duncan (1977, 1978), Reed and Duncan (1987) also justified the application of baroclinic instability theory to explain the development of PLs in their numerical studies of various PL cases.

PLs that develop through pure baroclinic instability are understood to be of two types; i) systems that develop under normal, forward-shear conditions (Harrold and Browning, 1969; Mansfield, 1974; Duncan, 1977), and ii) systems that develop under the so called 'reverse-shear' conditions (Duncan, 1978; Haugen, 1986; Reed and Duncan, 1987). The reverse-shear conditions are typified by the lower-troposheric thermal wind and the mean wind blowing in opposite directions to each other, whereas the thermal wind and the mean wind blow in the same direction under the forward-shear conditions. In other words, while the mean wind speed decreases with height in a reverse-shear flow, it increases with height in a forward-shear flow. The main dynamical difference between the two conditions is that an upper-level positive voticity advection (PVA) is required for a PL to develop under the forward-shear conditions, but it is not a requirement for the formation of a PL under the reverse-shear conditions (Businger and Reed, 1989). The similarity between the two conditions is that a comma cloud develops in conjunction with the PL development under both the conditions.

The baroclinic instability theory was able to explain the formation of 'comma' shaped clouds, identified in the imagery from various polar orbiting weather satellites, during PL developments. However, the theory could not effectively account for the deep, cumulus convection organised in spiral bands that features many PLs. Rasmussen (1979) and Økland (1977) used the theory of conditional instability of the second kind (CISK, see Charney and Eliassen, 1964; Ooyama, 1964) to explain the nature of the organised circulation around the vortex. To be significant, CISK mechanism requires high values of convective available potential energy (CAPE) which is likely to occur during strong Arctic air outbreaks over relatively warm sea surfaces (Rasmussen, 1979). It was understood lately that PLs may also develop through a combination of both baroclinic instability and CISK processes (e.g., Reed, 1979; Sardie and Warner, 1983, 1985; Albright et al., 1995).

In a review article of PLs, Businger and Reed (1989) provided three classifications for these systems, namely, i) short-wave/jet-streak type, ii) Arctic-front type, and iii) cold-low type. These classifications were based mainly on the synoptic conditions associated with the PL developments. From a physical perspective, the above categories were distinct in the degree and distribution of baroclinicity, static stability and the surface fluxes of latent and sensible heat. The short-wave/jet-streak systems are characterised by a positive potential vorticity anomaly at upper-levels, moderate baroclinicity and modest surface fluxes. On the other hand, the Arctic front systems are typified by strong surface fluxes and strong and shallow baroclinicity whereas the cold-low type PLs are identified by weak baroclinicity, strong surface fluxes and deep convection. This implies that the structure and dynamics of PLs are highly sensitive to the magnitudes of various physical factors and that several processes may operate simultaneously during the life cycle of a PL.

To understand the influence of different physical factors on PLs, several sensitivity experiments have been carried out in the past (e.g., Sardie and Warner, 1983, 1985; Roch et al., 1991; Albright et al., 1995; Pagowski and Moore, 2001). These case studies revealed the importance of an ice-free, open water surface, heat and moisture fluxes from the surface, and condensational heating for the development of PLs. However, the interaction between different physical factors is highly non-linear in the real atmosphere and may vary from case to case depending on, for example, the geographical location and other conditions.

Sensitivity experiments in an idealised atmosphere have proven useful in order to account for the relative importance of individual physical processes in the development of PLs. Using a three-dimensional nonhydrostatic model, Yanase and Niino (2007) investigated the way individual processes influence PLs. The basic state for the study was characterised by an axi-symmetric vortex at the surface with a finite radius and an uniform vertical shear of the zonal wind. The experiments of Yanase and Niino revealed that the structure of the PL was highly sensitive to the degree of baroclinicity present in the troposphere. An inclusion of condensational heating and surface fluxes resulted in an enhancement of the growth rate of the PL. The work effectively demonstrated the impacts of different physical conditions on the growth rate, energetics and structure of PLs. However, the influence of upper-level forcing on the characteristics of PLs was not accounted for in the study.

Given the fact that many PLs are triggered when an upper-level trough advects over lower-level frontal zones, it is important to understand how the strength and the structure of a PL is affected by the structure of the potential vorticity anomaly associated with the upper-level trough. This may have direct implications to the issue of PL forecasting in the sense that it might be possible to qualitatively predict the features of a PL if the distribution of upper-level potential vorticity is known. Moreover, many PLs are characterised by a downward penetration of the upper-level perturbation causing a coupling between upper-level and lower-level features. Such a vertical coupling leads to cyclone intensification. The coupling process mainly depends on the magnitude of static stability, baroclinicity and surface heating. The relative influence of these physical parameters is not well understood.

This paper addresses the issue of the formation and growth of PLs forced by a finite amplitude perturbation at upper-levels in an ideal baroclinic channel. Only the forward-shear PL developmentts shall be considered

here. The purpose of the study is two-fold. First, to analyse the influence of the structure of the upper-level potential vorticity anomaly on the characteristics of a PL. Second, to understand the relative influence of three key factors that play decissive role in the growth of a PL, namely, static stability, baroclinicity and surface heating. The existing literature dealing with the evolution of baroclinic disturbances in an ideal atmosphere (e.g., Farrel, 1982, 1985; Rotunno et al., 1994; Wernli et al., 1999) focussed largely on synoptic scale systems. The experiments described in this paper were carried out at a model resolution of 10 km so that the processes important for mesoscale disturbances can be simulated realistically.

Model configuration and set-up of the basic state, including the details of the sensitivity experiments, is described in the next section. The results are discussed in section 3 followed by the summary and conclusions in section 4.

2. Experimental set-up

Weather Research and Forecasting model (Wang et al., 2008) is used for the simulations in an idealised baroclinic channel. Horizontal grid length is 10 km and the model has 36 vertical levels ranging from 1000 hPa up to ~ 80 hPa. Periodic boundary conditions have been applied at the zonal boundaries whereas the meridional boundaries are symmetric. The simulation domain covers an area of ~ 6000 x 5000 km.

Computation of surface fluxes of heat, moisture and momentum are based on Monin-Obukhov similarity theory using the stability functions from Paulson (1970), Dyer and Hicks (1970) and Webb (1970). Vertical transport and mixing in the boundary layer are accounted for by using YSU-PBL scheme (Hong et al., 2006). Sub-grid scale convective processes and cloud formation are parametrized using the Kain-Fritsch scheme (Kain, 2004) and microphysical cloud properties are determined through the WSM-6-class scheme (Hong et al., 2004; Dudhia et al., 2008).

The basic state deployed for the simulations is taken from Wernli et al. (1999). The original state in Wernli's case was of a horizontal resolution ~ 75 km. In the present study, the resolution has been increased to 10 km in order to make the set-up suitable for addressing the development of PLs. The channel has a two-dimensional baroclinic jet-like feature superposed by a finite amplitude initial perturbation at the tropopause level. The tropopause is situated at a level of ~ 6.5 km (~ 380 hPa) above the surface which is normally the case during PL developments in real atmosphere. Figure 1 portrays a horizontal cross section of the baroclinic jet at the tropopause level superposed by a positive potential vorticity anomaly of ~ 2 PVU. Aslo shown in the figure is the meridional temperature gradient at the surface in terms of potential temperature isolines.

The upper-level perturbation is specified in terms of a positive anomaly in the quasi-geostrophic potential vorticity (PV) field. The anomaly is in Cartesian space (x,y,z) and is determined by applying a PV inversion tool of Fehlmann (1997). The upper-level PV anomaly is prescribed in the following form:

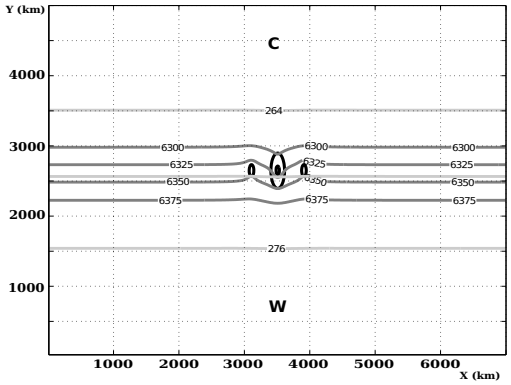

Figure 1. A horizontal section of the basic state showing the potential vorticity perturbation superposed at the tropopause level (~ 6.5 km). Black contours indicate potential vorticity at the tropopause level. Magnitude of the cenrtal most contour is 2 PVU, encircled by the contour of 1 PVU. The contours on either side of the 1 PVU contour have a magnitude of -0.2 PVU (1 PVU = 10^{-6} ms^{-1}Kkg^{-1}). Light gray contours represent isentropes at the surface (at 6 K interval) with warm area in the southern half and cold in the northern and dark gray contours represent the geopotential height at the tropopause level (at 25 m interval). The grid distance is in kilometers.

$$
\begin{aligned}
q'(x,y,z) = \Bigg\{ & A_c exp\left[-\left(\frac{x}{L_x}\right)^2\right] \\
& + A_l exp\left[-\left(\frac{x+d}{L_x}\right)^2\right]\Bigg\} \\
& + A_r exp\left[-\left(\frac{x-d}{L_x}\right)^2\right]\Bigg\} \\
& \times \Bigg\{ exp\left[-\left(\frac{y}{L_y}\right)^2\right] \\
& \times exp\left[-\left(\frac{z-z_0}{L_z}\right)^2\right]\Bigg\} \qquad (1)
\end{aligned}
$$

Where A_c, A_l and A_r represent the magnitudes of the center, left and right anomalies respectively. The center anomaly is positioned at $(0, 0, z_0)$ and the left and the right anomalies are shifted in the zonal direction on the either side of the central anomaly by a distance d (km). In this paper, d equals 400 km in all the experiments. z_0 is the height of the tropopause. L_x and L_y are the horizontal scales of the anomaly in the zonal and meridional direction respectively. L_z denotes the vertical decay scale of the anomaly which equals ~ 8 km in all the experiments.

Table-I lists the sensitivity experiments that comprise of a number of tests with different initial conditions. The abbreviation *CTL* stands for the *control* simulation. The experiments termed *PV1* and *PV2* denote the sensitivity experiments with modified horizontal scale of the upper-level PV anomaly. The rest of the experiments focus on the relative influence of static stability 'N' (*N1*), baroclinicity 'B' (*B1*), and surface potential temperature 'θ_s' (θ1) of the basic state on the formation and growth of a PL. Magnitudes of N, B and θ_s prescribed for the *CTL* simulation are such that the conditions in the baroclinic channel are favourable for the formation of a PL (Sardie and Warner, 1983; Yanase and Niino, 2007). In all the experiments, the simulations

Table I. List of the sensitivity experiments

Exp.	A_c (pvu)	A_l (pvu)	A_r (pvu)	L_X (km)	L_Y (km)	N (x 10^{-2} s^{-1})	B (x 10^{-3} s^{-1})	θ_s (K)
CTL	~ 2	~ -1	~ -1	800	700	0.9	~ 5	270
PV1	~ 2	~ -1	~ -1	800	250	0.9	~ 5	270
PV2	~ 2	~ -1	~ -1	200	700	0.9	~ 5	270
N1	~ 2	~ -1	~ -1	800	700	1	~ 5	270
θ1	~ 2	~ -1	~ -1	800	700	0.9	~ 5	260
B1	~ 2	~ -1	~ -1	800	700	0.9	~ 2.5	270

were stopped when the PL attains a steady state in terms of the surface pressure anomaly and the near-surface wind speed. Note that the steady state is achieved at different forecast times in different experiments.

Since the development of PLs may be influenced simultaneously by multiple physical processes such as baroclinic instability and convective instability, an unambiguous definition for a PL does not exist. PLs have been defined based on the relative importance of the forcing mechanism (Rasmussen and Turner, 2003; pp 10). A general definition that covers most of the existing definitions is given in Rasmussen and Turner (2003), pp 12. Within the framework of the experimental set-up described above, this paper uses a slightly modified version of the definition of Rasmussen and Turner to identify PLs, as given below:

"A polar low is a small, but fairly intense maritime cyclone that forms in the vicinity of a deep baroclinic zone. The horizontal scale of the polar low is approximately between 200 and 1000 kilometres and surface winds near or above gale force."

3. Results

3.1. The control simulation

The evolution of the flow in the baroclinic channel for the CTL case is shown in Figure 2. Cyclogenesis begins in the channel at 60 h, with the formation of a wave in the surface pressure field downstream of the center of the domain (not shown), where the upper-level PV anomaly was situated. 24 h later, the surface wave intensifies into two PLs that are separated by a distance of ~ 1500 km (Figure 2a). PL-1 appears to be stronger than PL-2, possibly due to its proximity to the initial upper-level PV anomaly (~ 2500 km downstream compared to ~ 4000 km that of PL-2). The formation of these PLs was marked by an increase in the near-surface wind speed from ~ 6 ms^{-1} to ~ 21 ms^{-1} in the case of PL-1, and to ~ 15 ms^{-1} in the case of PL-2 during the 24 h duration. The surface pressure anomaly corresponding to the PLs was found to be ~ -7 hPa for the first and ~ -5 hPa for the second when they formed. During the course of next 36 h, these PLs intensify further with the associated near-surface wind speed exceeding ~ 35 ms^{-1} and surface pressure anomaly deepening up to ~ -25 hPa for both the lows.

Two more PLs, namely PL-3 and PL-4, form in the channel at 96 h and 108 h forecasts respectively. Out of these, PL-3 develops as an upstream cyclone (~ 1000 km upstream of PL-1) and PL-4 forms ~ 1000 km downstream of PL-2, possibly as an imprint of the latter disturbance (for a detailed discussion of upstream cyclones, see Wernli et al., 1999). The horizontal scales of PL-3 and PL-4 are smaller and their intensity (in terms of surface pressure) weaker than that of PL-1 and PL-2 as evident in Figure 2.

The left panel of Figure 2 shows the flow patterns at the 500 hPa level and the surface level during the growth of the PLs in the channel. Shaded regions depict the potential vorticity at the 290 K isentrope. It can be seen that each PL is associated with a corresponding positive anomaly in the potential vorticity situated at the forward side of the 500 hPa trough, signifying an upper-level forcing for the growth of individual PLs. Shown on the right panel are the 1000−500 hPa thickness contours alongwith the surface pressure field. The thickness contours depict the pattern of thermal advection in the troposphere, resembling a typical baroclinic development, during the evolution of the PLs. The development was associated with ascending motion to the east of the surface low and descending motion to the west (not shown), which signifies the baroclinic energy conversion. The shaded patches on the same panel indicate the cloud features connected to the PL development. The cloudiness is indicated in terms of relative humidity at the 850 hPa level. At 120 h, the cloudiness looks to be sharper, well pronounced and of a comma-shaped in the case of PL-1 and PL-2 (Figure 2h). The cloud clusters attached to PL-3 and PL-4 do not show a clear structure until the 120 h forecast. Nonetheless, these cloud clusters can be expected to intensify and grow as comma-clouds by taking into account the baroclinic nature of the developments in the channel. Since PL-3 and PL-4 are relatively weaker than PL-1 and PL-2, and the latter two PLs are very similar in their structure and intensity, the focus shall only be on PL-2 in the sections to follow. Unless or otherwise specified, the terminology PL will refer to PL-2 hereafter.

A crucial dynamical and diagnostic field related to weather disturbances is the vertical motion (ω) associated with the system. In practice, ω is estimated through the $omega\ equation$ as per the quasi-geostrophic omega

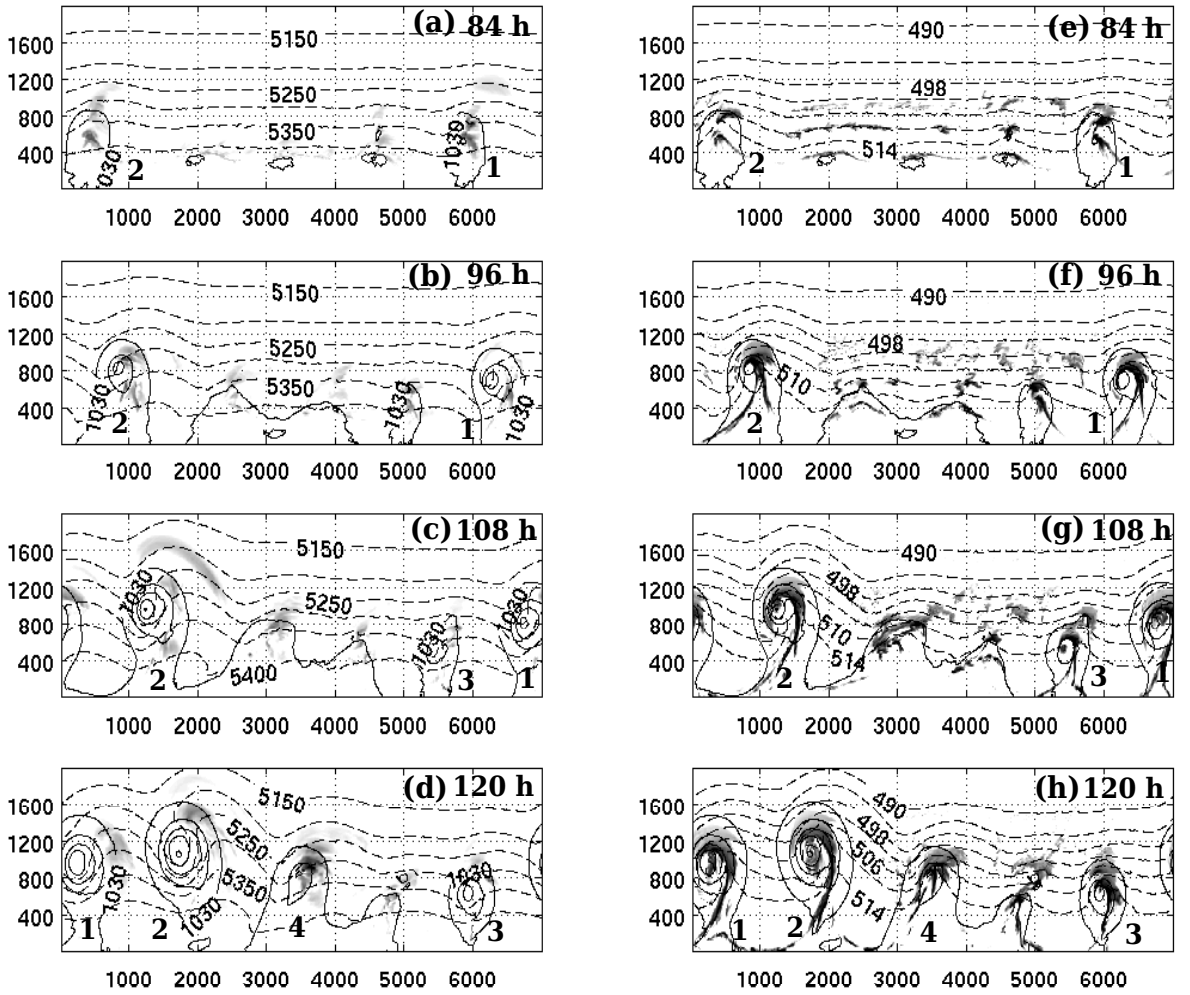

Figure 2. Flow characteristics for the CTL case at different time levels of the development. Plots on the left panel show surface pressure (solid contours at 6 hPa interval), 500 hPa geopotential height (dashed contours at 50 m interval) and potential vorticity at 290 K isentrope level (PVU values greater than 2 are shaded, with the darkest area representig values around 4 PVU). The right panel shows surface pressure (black contours at 6 hPa interval), 1000−500 hPa thickness (dashed contours at 4×10 m interval), relative humidity at 850 hPa level (areas greater than 80% are shaded, with the darkest shades representing 100% relative humidity). X- and Y-axes of the plots indicate respectively the west-east and south-north grids in kilometers.

equation (Holton, 2004; pp 164) which is given by

$$\left\{\nabla^2 + \frac{f^2}{\sigma}\frac{\partial^2}{\partial p^2}\right\}\omega = \frac{f}{\sigma}\left\{\frac{\partial v}{\partial p}.\nabla(f+\zeta)\right\} - \nabla^2 H \quad (2)$$

where H represents the contribution to ω from diabatic effects, σ refers to static stability paramter and ζ denotes relative vorticity. $\partial v/\partial p$ signifies the thermal wind. f is the Coriolis parameter. The terms on the right-hand side of the above equation represent the ω-forcing due to the advection of relative vorticity with the thermal wind (adiabatic forcing) and that due to diabatic effects respectively. The advantage of assessing ω from the above relation is that it allows to determine the relative role of the diabatic and adiabatic processes during the growth of a weather disturbance. Such an analysis is especially important as far as polar lows are concerned since the structure and dynamics of polar lows might differ depending on which process dominates during the growth. In one of such studies, Nordeng (1990) utilised the above relation to diagnose two polar lows with similar initial developments but different characteristics during the mature phase. He noticed that, in one of the two developments ω was forced by the advection of relative vorticity only. But in the case of the second polar low, diabatic processes played a significant role that led to a prolonged phase of the polar low. The major part of the analysis of the PL being discussed in the present paper was focussed on the evolution of ω and ω-forcing according to the above equation since the background conditions that were tested (Table-I) might modify the magnitudes of the adiabatic and diabatic ω-forcing.

Table-II shows the evolution of ω associated with the PL. The last two columns of the table indicate respectively the magnitudes of the adiabatic and diabatic ω-forcing. The magnitude of the condensational heating in the clouds formed during the development of the PL has been considered to be representative of the diabatic ω-forcing here. It is apparent from the table that both the adiabatic and diabatic ω-forcings are maximum until 96 h. At 102 h, the magnitudes of both the forcing terms drop suddenly and remain approximately steady afterwards. Such a pattern of the ω-forcing leads to a strong ω until

Table II. Evolution of the vertical motion (ω) and ω-forcing during the growth of the PL. The adiabatic and diabatic forcing terms in the last two columns are respectively the first and second terms on the right-hand side of the relation (2).

Time	Surface pressure anomaly (hPa)	Maximum ω at 850 hPa (Pa s^{-1})	Adiabatic ω-forcing (s^{-2})	Diabatic ω-forcing (Kh^{-1})
78 h	~ -3	~ -24	~ 9 x 10^{-7}	~ 16
84 h	~ -5	~ -22	~ 1 x 10^{-6}	~ 19
90 h	~ -10	~ -27	~ 1.5 x 10^{-6}	~ 15
96 h	~ -18	~ -21	~ 1 x 10^{-6}	~ 17.5
102 h	~ -21	~ -11	~ 3 x 10^{-7}	~ 8
108 h	~ -24	~ -10	~ 3 x 10^{-7}	~ 6.7
114 h	~ -26	~ -11	~ 4 x 10^{-7}	~ 8.2
120 h	~ -26	~ -11	~ 3 x 10^{-7}	~ 7

96 h and a low ω afterwards. The duration in which ω was strong is considered as the development phase of the PL and the duration where ω was relatively low is considered the mature phase in this paper.

The evolution of the 500 hPa flow and the surface flow associated with the PL during both the phases is illustrated in Figure 3. The upper-level flow is characterised by a wave with its trough positioned over the western flank of the PL, i.e., the area of cold air advection in the lower troposphere during the development phase, implying a westward tilt of the PL axis in the vertical. An important characteristic of the PL development is the reduction of the horizontal distance of separation between the 500 hPa trough and the surface vortex as the PL intensified. This occurs throughout the development phase (84 to 96 h) and continues during the initial stage of the mature phase which begins after 96 h (Figures 3a to c). In the later stages of the mature phase, the 500 hPa trough turns into a vortex and is positioned exactly above the surface cyclone at 120 h (Figure 3d). This means that the initial westward tilt of the PL axis gradually decreased during the development phase with the PL having no vertical tilt in the mature phase. Due to the reasons to be described later, it seems that the coexistence of the 500 hPa vortex and the surface vortex along a same vertical axis (with no westward tilt) is most likely the factor that might have reduced the growth rate of the PL in the mature phase.

Potential vorticity anomalies associated with upper-level troughs often tend to penetrate downwards and couple with the lower-level cyclonic features thereby providing an upper-level forcing for the growth of a cyclone. This dynamical phenomena can be better explained through an isentropic potential vorticity (PV hereafter) approach. The application of PV fields in the diagnosis of upper-level forcing in cyclogenesis in extratropical latitudes has been described in detail by Hoskins et al. (1985). Important relations from Hoskins et al. is given in the appendix of this paper. Figure 4 shows the vertical cross sections taken along the lines AB from Figure 3b and 3d (that represent the end of the development phase and the time a steady state was reached in the mature phase). The vertical cross sections run through the PL from southwest to northeast covering the region of cold air advection in the southwest, the center of the PL in the middle, and the region of warm air advection in the northeast. Towards the end of the development phase, the upper-level positive PV anomaly which was associated with the upper-level trough shows a tendency for a penetration towards lower-levels as illustrated by the 0.5 PVU contour shown in Figure 4a. In the mature phase, positive anomalies are induced also at the lower-levels (Figure 4b) which enhances the possibilities of a vertical coupling between the upper- and lower-level cyclonic vortices. Most likely, such a tendency for a vertical coupling is the dynamical factor that caused the slow growth of the PL in the mature phase by countering the affects of the decreasing ω.

Concerning the other features reflected by the vertical cross sections, the important one is the vertical westward tilt of the PL axis in the development phase (Figure 4a) and the absence of the same in the mature phase (Figure 4b). The figures also display the vertical structure of ω with the maximum values concentrated below the forward side of the upper-level trough which happens to be the region of positive vorticity advection at upper-levels (Holton, 2004; pp 152). This area is located above the center of the PL in the development phase but shifts slightly towards the right in the mature phase, with a corresponding shift in the area of maximum ω, due to the co-location of upper- and lower-level vortices.

3.2. Sensitivity experiments

The sensitivity experiments address the impacts of the scale of the upper-level PV anomaly, static stability, baroclinicity and surface heating on certain physical and dynamical features of the PL. Physical features include the structure and intensity of the PL and the dynamical features that were analysed comprise of the evolution of ω, the vertical PV coupling, the growth rate and phase speed of the PL.

3.2.1. Scale and structure of the upper-level PV anomaly

In the real atmosphere, polar lows have been identified with different scales, different structures, different life times and different intensities. In order to investigate the role of the scale and structure of upper-level PV anomalies in inducing such a variety in polar lows (or to study the role

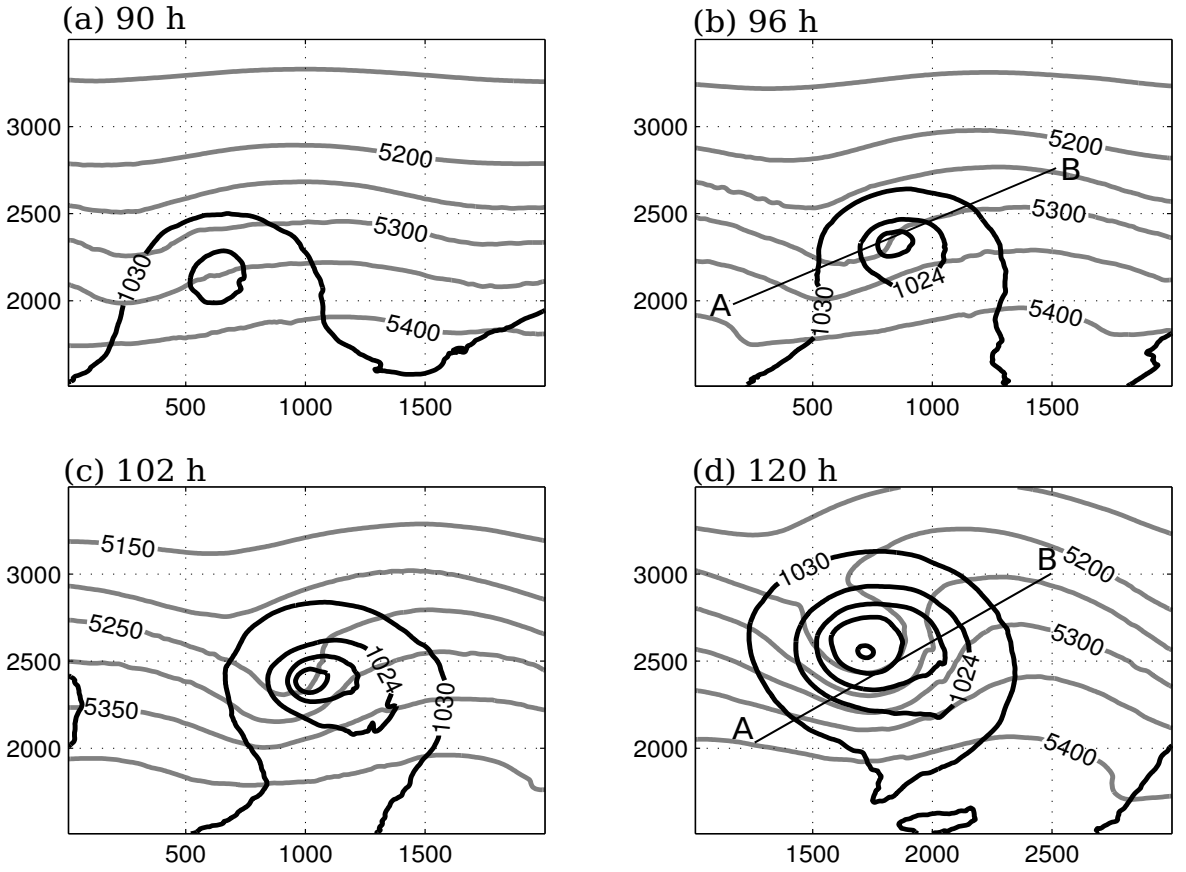

Figure 3. Characteristics of the upper-level and surface flow of PL2 in the CTL case at different time intervals of the development. Gray contours represent the 500 hPa geopotential height at 50 m interval and black contours represent the surface pressure at 6 hPa interval.

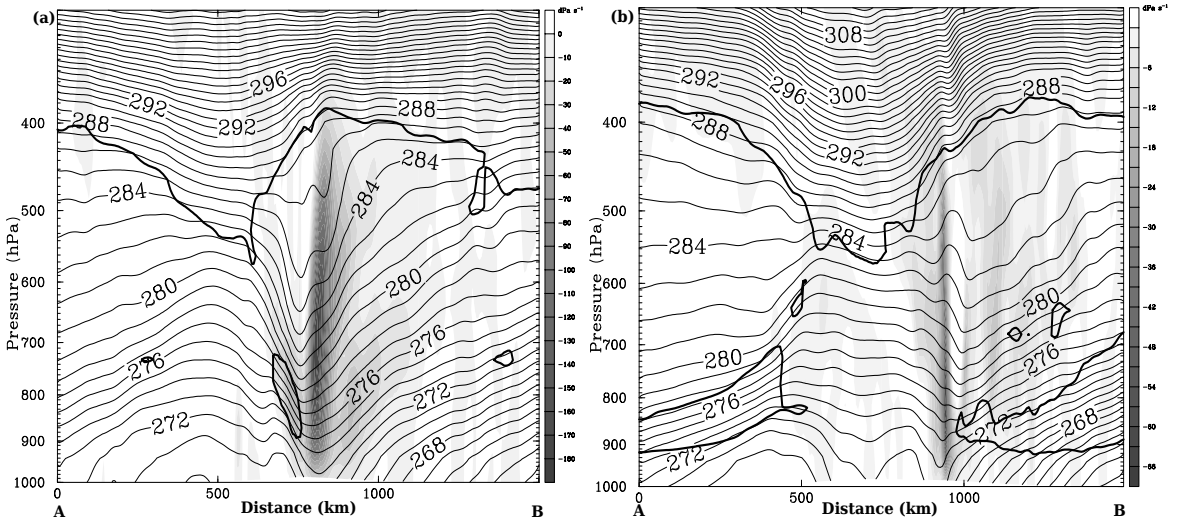

Figure 4. Vertical cross section through the PL in the CTL case at (a) 96 h and (b) 120 h along the A-B line of Figures 3b and 3d. Thick, black contours indicate the 0.5 PVU potential vorticity contour and thin, black contours represent isentropes at 1 K interval. Vertical motion (ω) is shaded.

of upper-level PV anomalies in modifying the physical and dynamical aspects of polar lows), two sensitivity experiments have been performed in this paper viz., PV1 and PV2 (see Table-I). In the former, the meridional extent of the anomaly was reduced to 250 km (cf. 700 km in the CTL case) whereas in the latter the zonal extent was reduced to 200 km (cf. 800 km in the CTL case).

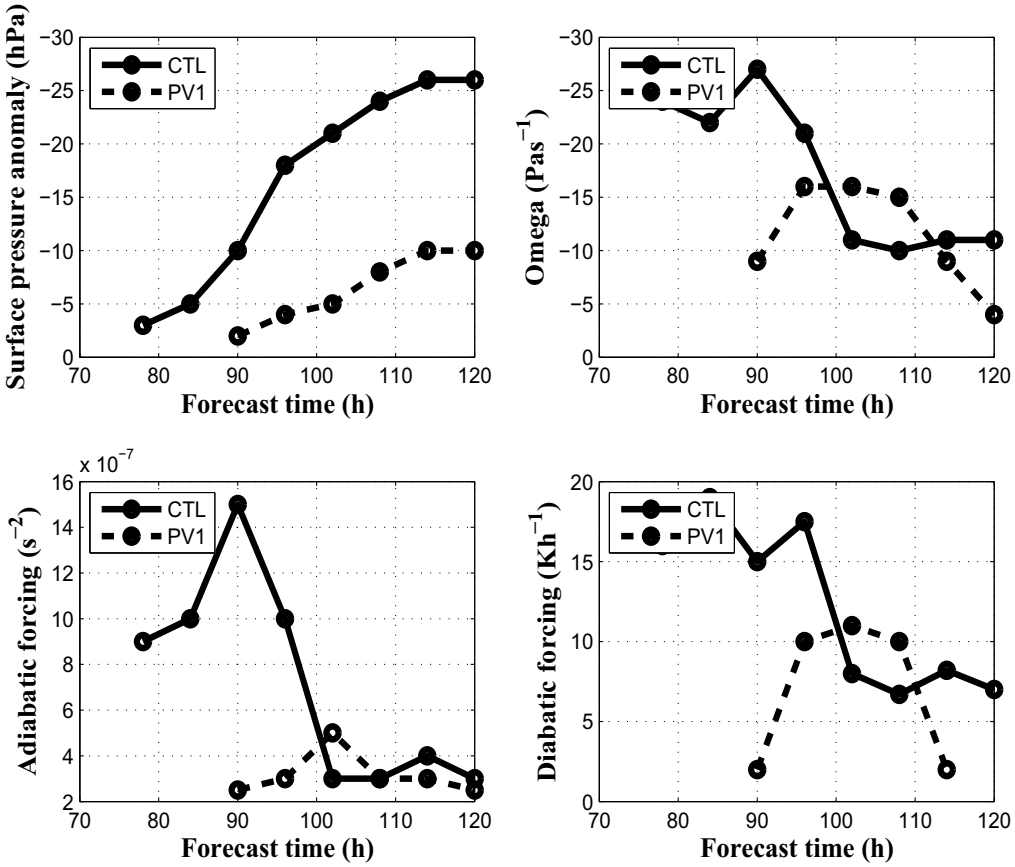

Figure 5. The evolution of surface pressure anomaly and the parameters of equation (2) for PV1 and CTL simulations.

In the PV1 case, the reduction of the meridional scale of the upper-level anomaly weakens the horizontal temperature gradient at the surface (not shown) which in turn reduces the vertical wind shear as per the thermal wind relation. Figure 5 shows the growth curves for the surface pressure, ω, and the ω-forcing during the growth of the PL in this experiment. The surface pressure curves for the CTL and the PV1 cases indicate that the formation of the PL delays by 12 h in the PV1 case. In addition, the intensity of the PL is much weaker in the latter case. This is obviously the outcome of the weaker vertical wind shear caused by the reduced meridional scale of the upper-level PV anomaly. Both adiabatic and diabatic ω-forcings attain peak values at 102 h in the PV1 case and accordingly, ω too has its peak value at 102 h which marks the end of the development phase. Note that the end of the development phase occured in the CTL case at 96 h. In the PV1 case, the magnitude of the adiabatic ω-forcing is much weaker than the CTL case which is a direct consequence of the relatively weaker vertical wind shear in the PV1 case. An interesting feature of the growth of the PL in the PV1 case is that the major contribution for the evolution of ω seems to be from the diabatic forcing since the adiabatic forcing is too weak. Particularly in the mature phase (which begins after 102 h), the fall in the magnitude of ω is due to the corresponding fall in the diabatic forcing as the adiabatic ω forcing is moreorless constant.

Figure 6 shows the evolution of the upper- and lower-level flow during the growth of the PL in the PV1 simulation. There is a weak upper-level trough with a westward tilt at the beginning of the PL growth. The trough intensifies during the development phase with a reduction in the vertical tilt of the PL axis. The important difference in the PV1 case with respect to the CTL case is that the upper-level trough has a wavelength of ~ 1500 km in the former whereas it was around 1000 km in the latter. The longer wavelength of the upper-level trough in the PV1 case forces a structural change in the PL. While the vortex was nearly circular in the CTL case, it has a west-east elongation in PV1 case as indicated by the surface pressure pattern of the PL (Figure 6). However, the scale of the PL remains the same as in the CTL run (~ 1000 km) because the zonal scale of the PV anomaly is the same in the two cases.

Figure 7 shows the vertical cross sections across the PL along the lines AB from Figure 6 that respectively represent the last stage of the development phase and the time when a steady state was reached in the mature phase. There are no indications of a downward propagation of the upper-level forcing in the development phase. However, in the mature phase the upper-level forcing shows signs of advancement towards the lower-levels. But the signal appears to be much

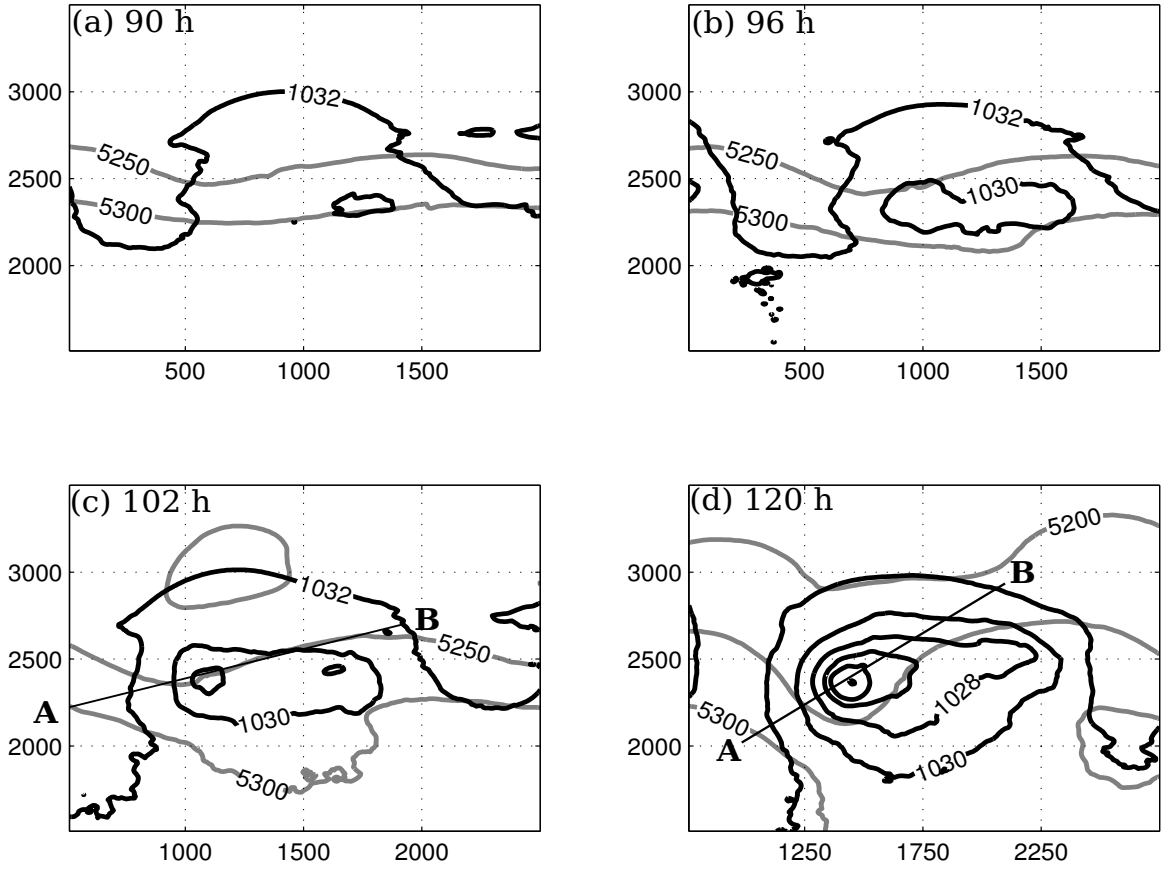

Figure 6. Same as in Figure 3, but for the PV1 case. The surface pressure contours are drawn at 2 hPa interval here.

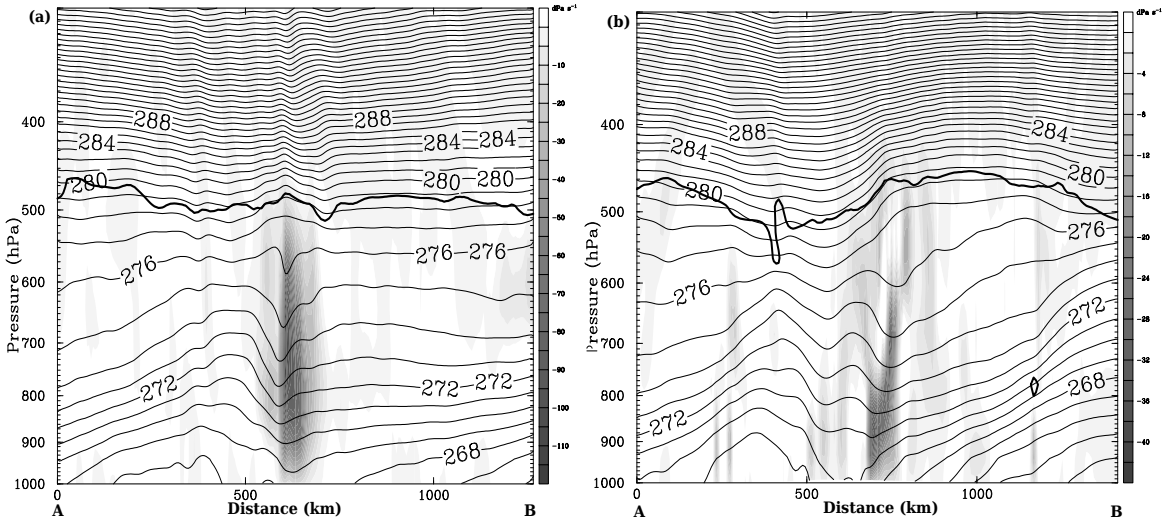

Figure 7. Same as Figure 4, but for the PV1 case.

weaker than that identified for the CTL case, which is notable considering that only the meridional scale of the upper-level anomaly was reduced in the PV1 experiment with the amplitude and other physical factors unchanged. The upper-level anomaly showing less penetration depth in the vertical plots explains why the PL was less intense in the PV1 simulation.

In the PV2 simulation, where the zonal scale of the upper-level anomaly was reduced to 200 km from its value of 800 km in the CTL case, the PL formation takes place at 84 h. Figure 8 displays the development of surface

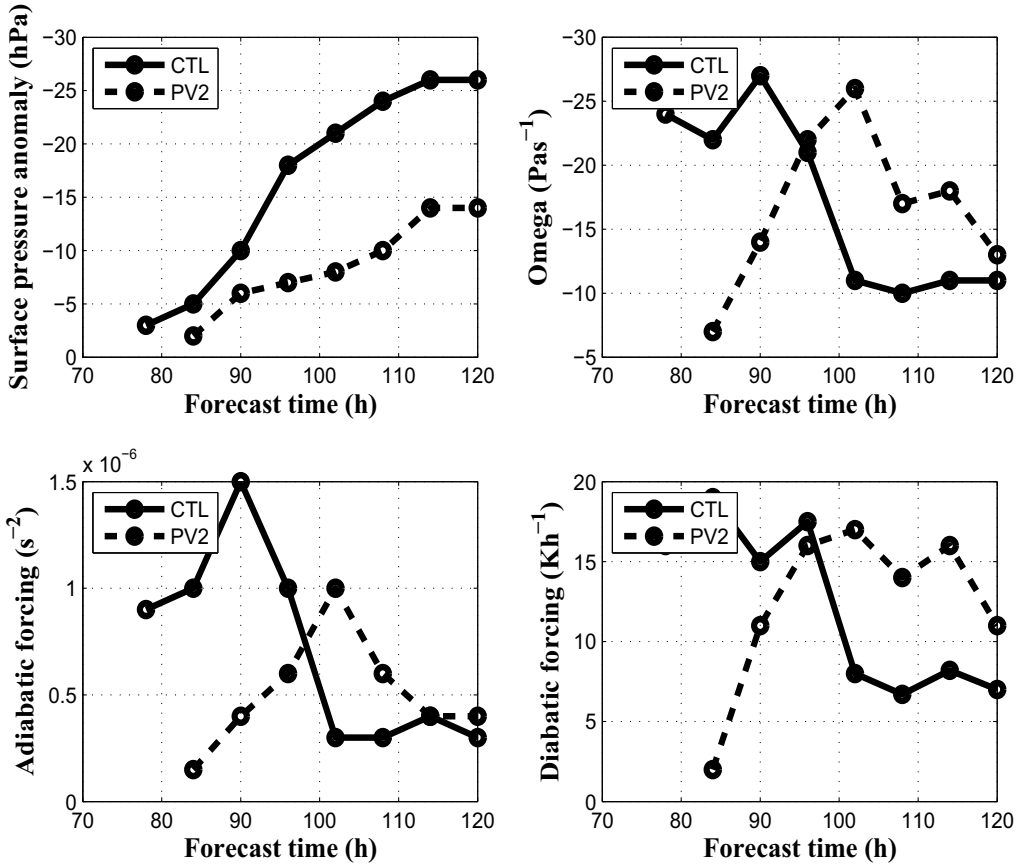

Figure 8. The evolution of surface pressure anomaly and the parameters of equation (2) for PV2 and CTL simulations.

pressure, ω and ω-forcings during the growth of the PL for this simulation. The development phase has a duration of 18 h, starting at 84 h and ending at 102 h with the mature phase occurring after 102 h. Magnitudes of ω and ω-forcing rise rapidly during the development phase, decrease rather slowly during the mature phase. A striking feature reflected by the figure is that both the ω-forcings, especially the diabatic one, tend to be stronger in the mature phase of the PV2 simulation than the mature phase of the CTL simulation. This results in ω being stronger in the PV2 case than the CTL case during the mature phase. The reasons for such a situation are explained below.

Figure 9 shows the horizontal structure of the 500 hPa and the surface flow associated with the PL at the end of the development phase and in the mature phase for the PV2 simulation. The scale of the PL in this case reduces to ~ 500 km (cf. ~ 1000 km in the CTL case), due to the reduction in the zonal scale of the PV anomaly, as evident from the figure. The upper-level flow is much weaker than that in the CTL case. The trough intensifies as the PL grows, with the vertical westward tilt of the PL decreasing with time. However, the tilt is still present in the mature phase (Figure 9b), in contrast to that in the CTL and the PV1 cases. This has important implications to the pattern of differential thermal advection in the lower-troposphere. Hypothetically, a westward tilt is necessary for the maintanence of lower-tropospheric thermal advection, which in turn is important for the growth of a baroclinic wave, according to the geopotential tendency equation (Holton, 2004; pp 159). Table-III displays the magnitudes of the advection of the thickness between 925 and 850 hPa levels, which represents the lower-tropospheric thermal advection, for the CTL, PV1 and PV2 cases during both the phases of the PL growth. Only the values of the thickness over the area of warm air advection is presented in the table since it is this area that corresponds to ascending motion. Note that the magnitude of the advection of 925−850 hPa thickness increases rapidly and attains the peak value nearly at the end of the development phase or at the beginning of the mature phase and decreases slowly later in the mature phase for the CTL and the PV1 cases. The time when the magnitude of the thermal advection reaches the peak value marks the time when the upper-level vortex was positioned exactly over the surface vortex i.e., with no vertical tilt of the PL axis. The values for the PV2 cases suggest an increase of the strength of the thermal advection even in the mature phase, implying that the tilt was persistent in the PV2 case which is reflected in the horizontal cross section of the PL in the mature phase (Figure 9b). It is thus reasonable to believe that the presence of the westward tilt of the PL axis in the mature phase is most likely the factor that forced ω-forcings (and ω) to be stronger in the PV2 case than that in

Table III. Magnitudes of the advection of 850−925 hPa thickness (s^{-1}) at different stages of growth for the CTL, PV1 and the PV2 cases.

Time	CTL	PV1	PV2
78 h	~ 0.002	-	-
84 h	~ 0.003	-	~ 0.001
90 h	~ 0.006	~ 0.009	~ 0.0015
96 h	~ 0.010	~ 0.002	~ 0.0025
102 h	~ 0.010	~ 0.0025	~ 0.004
108 h	~ 0.008	~ 0.003	~ 0.005
114 h	~ 0.008	~ 0.003	~ 0.006
120 h	~ 0.006	~ 0.002	~ 0.006

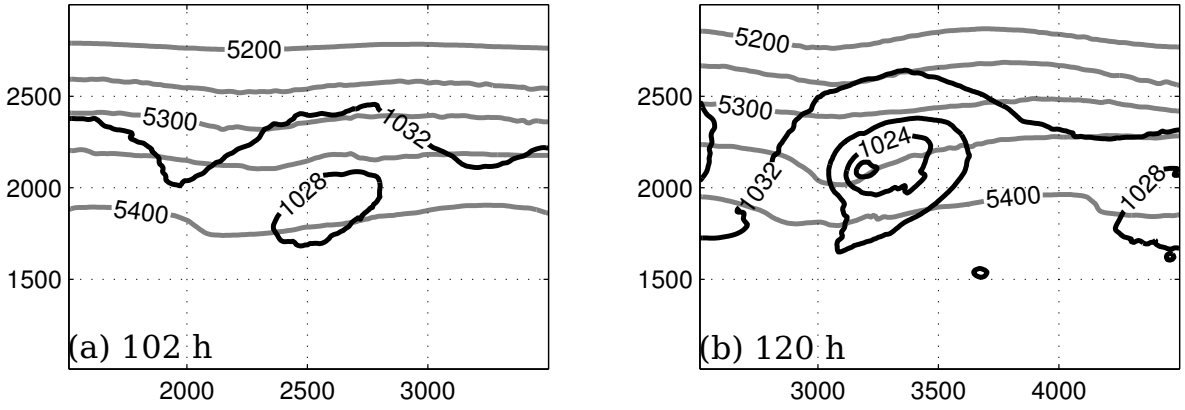

Figure 9. Upper-level and surface flow characteristics of the PL at (a) 102 h and (b) 120 h forecasts in the PV2 case. Gray contours represent 500 hPa geopotential height isolines at 50 m interval and black contours represent the surface pressure at 4 hPa interval.

the CTL case (wherein the vertical tilt was absent) in the mature phase.

Concerning the vertical PV coupling, PV2 simulation was very much similar to the PV1 case i.e., the upper-level PV anomaly showed signs of a penetration towards lower-levels only in the mature phase (not shown). The tendency was much weaker than that in the CTL case, which implies that the reduction in the scales of the upper-level PV anomaly in the PV1 and PV2 cases had negative impacts on the vertical coupling which in turn lowered the intensity of the PL.

The changes in the structure and scale of the PL in the PV1 and PV2 simulations with respect to the CTL simulation are to be noted. When the scale of the PV anomaly was reduced along the meridional axis (PV1 case), the PL showed a west-east elongation with its scale remaining unchanged with respect to that in the CTL case. When the scale of the PV anomaly was reduced along the zonal axis (PV2 case) the scale of the PL was reduced significantly with not much structural changes. In short, the scale, structure and intensity of the PL seems to be proportional to the scale of the upper-level PV anomaly.

3.2.2. Static stability

Static stability is one of the major physical factors that play an important role in the life cycle of PLs. From equation (A2) in the appendix, it is clear that an area with low static stability favours a vertical coupling of the upper-level anomaly with the lower-level features even if the horizontal scale of the anomaly is small, thereby causing or enhancing cyclogenesis at lower-levels. In the experiment N1, the static stability in the channel is increased from 0.009 s^{-1} (CTL case) to 0.01 s^{-1} (see Table-I). Static stability of similar (or higher) magnitudes can normally be seen over the ice-covered regions of the Arctic. The rest of the factors in the N1 experiment are same as that in the CTL run.

The evolution of surface pressure, ω, and the ω-forcings during the growth of the PL in the N1 experiment is shown in Figure 10 alongwith the same details for the CTL simulation. In the N1 experiment, the PL formation delays by ~ 18 h with respect to that in the CTL run. The magnitudes of both the ω-forcings increase as the PL grows, reach the peak values at around 120 h and start to decline later on thereby forcing a similar pattern in ω. This suggests that the development phase of the PL in the N1 case occurs between 96 h and 120 h, followed by the mature phase afterwards. Note that the development phase of the PL in the N1 case corresponds to the time when the PL in the CTL case is going through its mature phase. Because of this, ω in the N1 case is stronger than that in the CTL case throughout the growth of the PL (in the N1 case). The gap in the magnitude of ω (and ω-forcing) between the N1 and the CTL cases is maximum at 120 h which marks the onset of

mature phase in the N1 case. After 120 h, the gap gradually narrows down and at around 144 h both the N1 and the CTL simulations have roughly the same values of ω and ω-forcings.

Figure 11 shows the horizontal sections of the PL in the N1 experiment in the development phase and mature phase. In the development phase, the 500 hPa trough is not as prominent as it was in the CTL simulation which means that the PL in the N1 case is shallower than its CTL counterpart (Figure 3b). However, the PL deepens in the mature phase as the upper-level trough turns into a vortex. The vertical structures of the PL in the N1 case in the development phase and mature phase are shown in Figure 12. The tendency for a downward penetration of the upper-level PV anomaly is negligibly weak in the development phase (Figure 12a), since the upper-level trough at this time was very weak. However, the tendency builds up slightly in the mature phase, but is weaker than that in the CTL case. As implied by Figure 12b, the vertical penetration depth of the upper-level anomaly when the simulation was stopped becomes ~ 1 km (cf. ~ 1.6 km for the CTL case).

The reduction of the downward penetration depth of the upper-level PV anomaly in the N1 experiment was an expected result since it is well known that high static stability is not favourable for a deep penetration of the upper-level anomaly as implied by relation (A2) in the appendix. But, considering the fact that the static stability was increased in the N1 experiment only by a factor of 0.001 s^{-1} from the CTL simulation, the above mentioned change in the vertical penetration depth becomes quite substantial. In addition, it is interesting to note that a slight increase in the static stability could delay the formation of the PL by ~ 12 h and could lengthen the development and mature phase of the PL.

3.2.3. *Surface heating*

Sensitivity of polar lows to surface heating has been an important issue in several case studies in the past. For example, Albright et al. (1995) performed certain experiments on a polar low that formed over Hudson Bay during 8−9 December 1988. In one of the experiments, the SST was raised by 8 K which led to a significant strengthening of the polar low with the associated wind speed exceeding hurricane force. Strong surface heating influences a polar low by strengthening the upward surface fluxes that in turn would lower the stability in the atmospheric layers. In addition to the strength, the dynamics of a polar low too could be highly sensitive to the surface heating in the sense that increased surface heating might lead to deep and organised convection during marine cold air outbreaks over warm ocean basins, thereby favouring CISK-type mechanisms in the cold airmasses. As a consequence, diabatic processes may become significant and provide a corresponding forcing for the vertical motion associated with a polar low as shown by Adakudlu and Barstad (2011). In the $\theta 1$ experiment of the present paper, the potential temperature at the first model level in the initial state was decreased by 10 K from its value in the CTL experiment (Table-I). Although a general weakening in the strength of the PL is expected from this experiment, it would be interesting to know how the ω-forcing is modified by the surface cooling.

Figure 13 shows a comparison of the evolution of the surface pressure, ω and ω-forcing during the growth of the PL between the $\theta 1$ and the CTL simulations. Formation of the PL in the $\theta 1$ takes place 6 h later than that in CTL case, i.e., at 84 h. The growth rate of the PL in the $\theta 1$ case appears to be much weaker when compared to the CTL case as indicated by the surface pressure curves of these two cases in the figure. ω, in the $\theta 1$ experiment, tends to be maximum at 120 h implying the end of the development phase of the PL. The striking difference between the CTL and the $\theta 1$ cases is in the degree of diabatic ω-forcing during the PL growth. While the diabatic forcing was as important for ω as the adiabatic one in the CTL case, ω is influenced only by the adiabatic forcing in the $\theta 1$ case. The diabatic forcing was negligibly weak with values near 1 Kh^{-1} during both the phases of the PL in the $\theta 1$ case and hence is not shown in the figure. In addition, the magnitude of the adiabatic ω-forcing too is much lower in the $\theta 1$ case than the CTL case during the development phase. Note that the peak value of ω in the $\theta 1$ case is of a similar order as its minimum value in the CTL case. This implies that surface cooling may suppress both the adiabatic and diabatic ω-forcings, with a stronger effect on the diabatic forcing, during the development of a polar low.

Gross characteristics of the upper-level and the surface flow associated with the PL in the development and the mature phase in the $\theta 1$ simulation are illustrated in Figure 14. The scale of the PL, in both the phases, seems to be smaller than that in the CTL case (~ 600−700km in the $\theta 1$ case versus ~ 1000 km in the CTL case). The exact reason for this is not clear. Nonetheless, the chances are that the lack of diabatic forcings might have caused such a reduction in the scale of the PL. Comparing Figure 14 with Figures 3b and 3d, it follows that there is a delay of about a day for the PL in the $\theta 1$ case to reach the end of the development phase and the steady state in the mature phase.

A reduction in the downward penetration depth of the upper-level PV anomaly can be expected in the $\theta 1$ experiment since the surface cooling has led to a weakening in the intensity of the PL which is directly associated with the downward penetration depth. Figure 15 displays the vertical cross sections across the AB lines of Figures 14a and 14b. A weak tendency for a vertical coupling occurs towards the end of the development phase (Figure 15a), which does not grow much in the mature phase. The penetration depth of the upper-level anomaly in the mature phase is of the order ~ 800 m, which is nearly half the value obtained for the CTL experiment at the corresponding time.

The results from the $\theta 1$ experiment have shown that the physical mechanisms driving a polar low are very sensitive to the surface heating. If the static stability, baroclinicity and upper-level forcing are favourable for the formation of a polar low, the colder is the surface, the more is the likelihood of the polar low being of a pure baroclinic nature.

3.2.4. *Baroclinicity*

Baroclinicity is one of the most important factors that control the structure and dynamics of a polar low. From the experiments of Yanase and Niino (2007), it becomes clear that the energy budget and the structure of a polar low are highly proportional to the baroclinicity inherent in the flow at the initial state. But their experiments do not state how does an upper-level forcing react to the changes in the initial baroclinicity. Further, the sensitivity of the adiabatic and diabatic forcing parameters to the magnitude of the baroclinicity is not well understood from

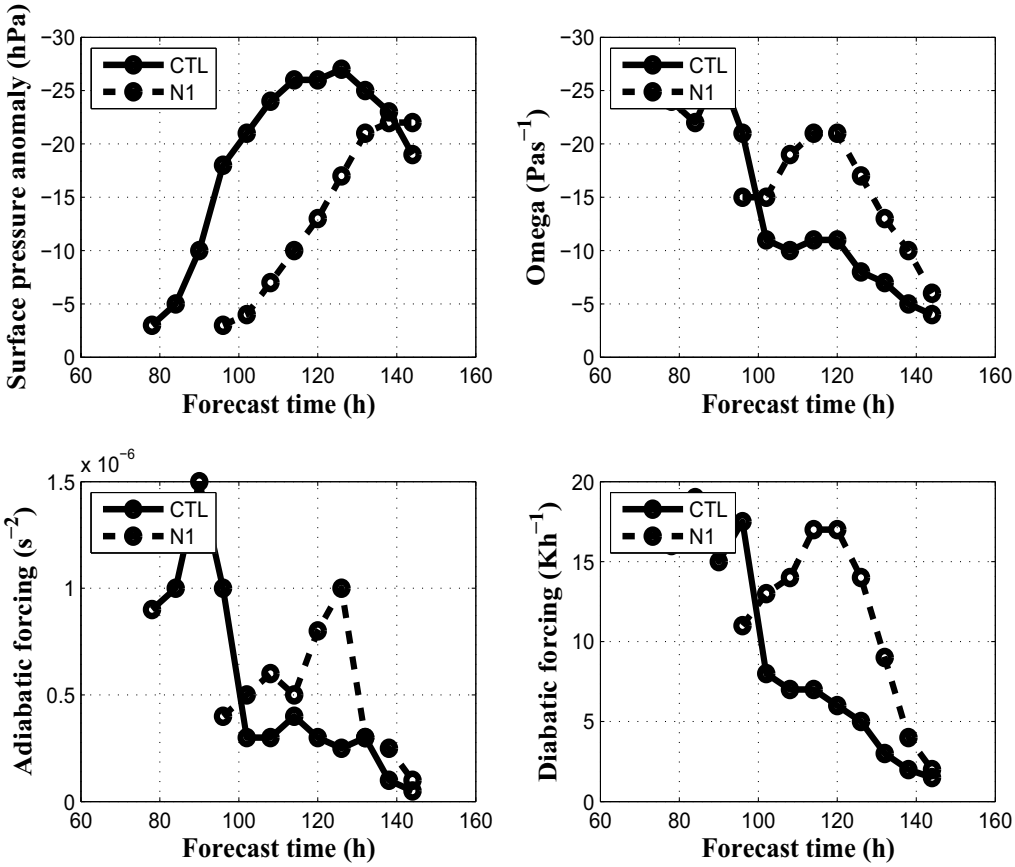

Figure 10. The evolution of surface pressure anomaly and the parameters of equation (2) for N1 and CTL simulations.

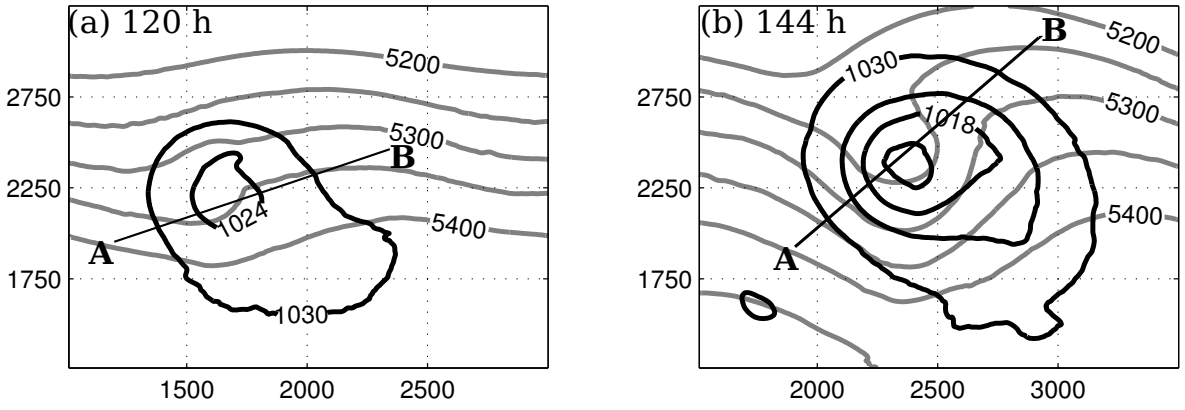

Figure 11. Same as in Figure 3, but now for the N1 experiment.

the study of Yanase and Niino. The present section attempts to investigate the impacts of the magnitude of baroclinicity mainly on the upper-level forcing and the evolution of the diabatic and adiabatic ω-forcings during the growth of the PL. For this study, the baroclinicity of the basic flow was reduced roughly by a factor of two from the conditions in the CTL simulation (Table-I).

In the case of B1 experiment, there is a substantial delay in the formation of the PL which occurs at 120 h. The evolution of ω and the ω-forcing and the surface pressure anomaly during the growth of the PL for this case is shown in Figure 16. The magnitudes of the surface pressure anomaly observed during the growth of the PL indicate that the strength of the PL has fallen significantly in the B1

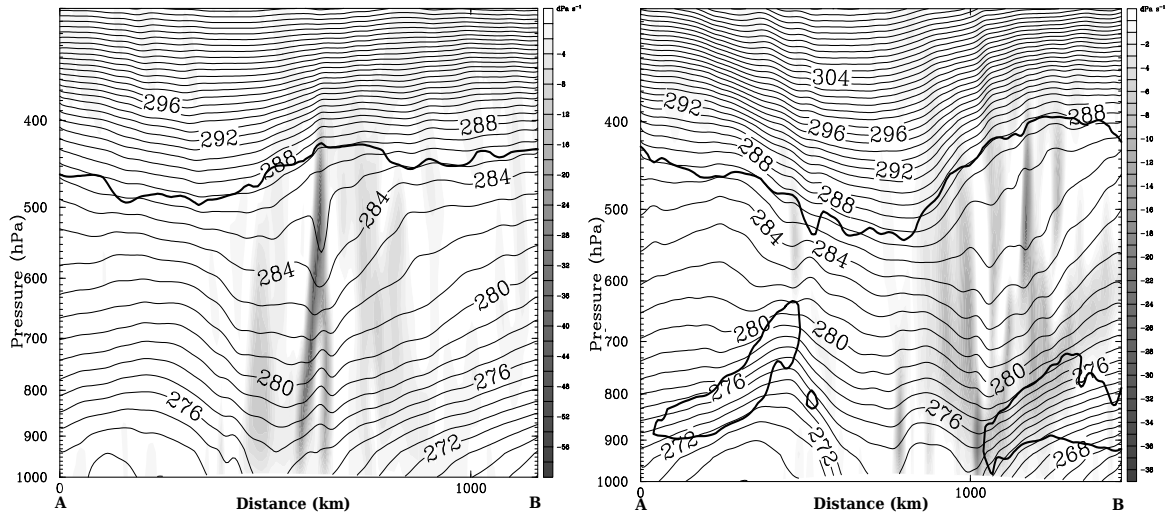

Figure 12. Vertical cross section across the PL along the lines A-B of Figure 11. Contour details are the same as in Figure 4.

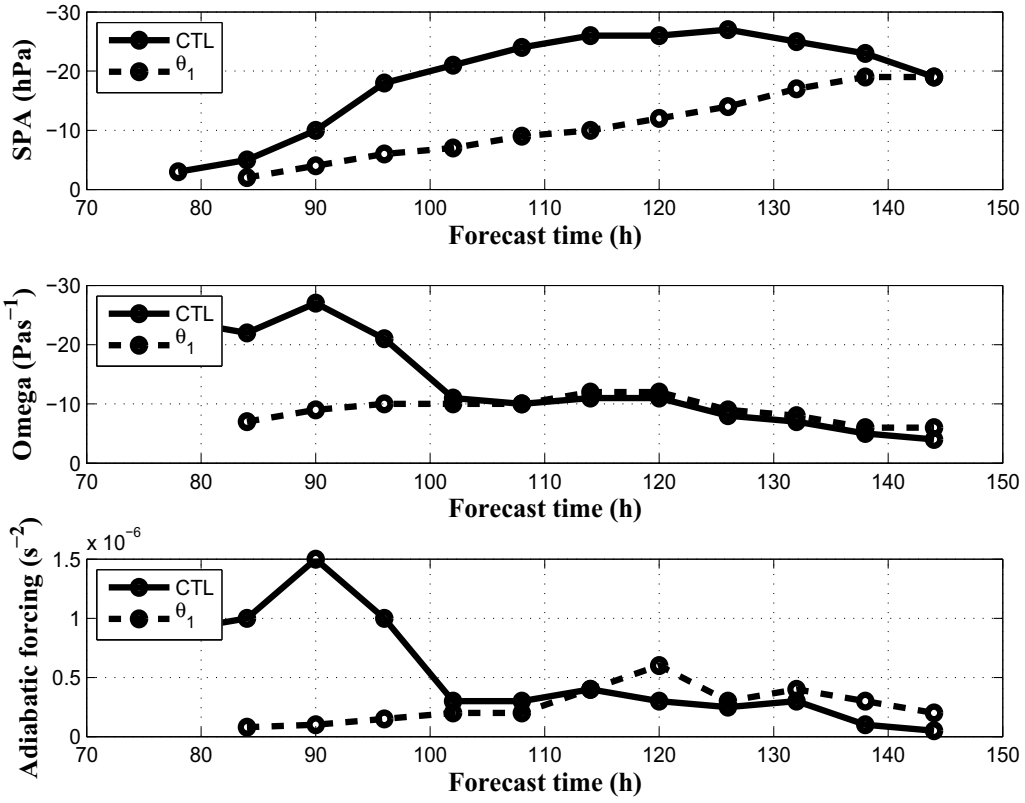

Figure 13. The evolution of surface pressure anomaly and the parameters of equation (2) for $\theta 1$ and CTL simulations (SPA stands for surface pressure anomaly).

simulation in comparison with the CTL simulation. Also, the degree of the adiabatic ω-forcing in the development phase of the B1 simulation is considerably lower than that in the development phase of the CTL simulation, which is a direct consequence of the reduction in the initial baroclinicity in the B1 simulation. This is an expected

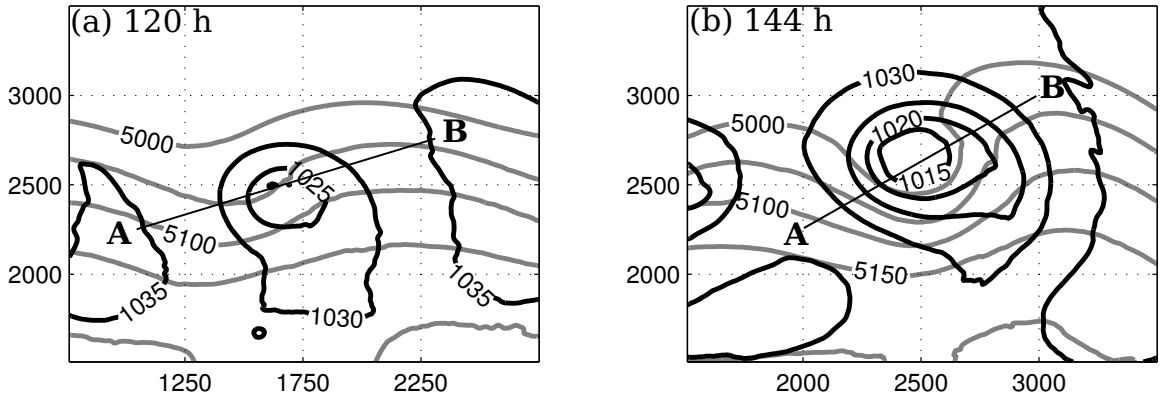

Figure 14. Horizontal cross sections across the PL in the $\theta 1$ experiment showing the 500 hPa flow (gray contours at 50 m interval) and the surface pressure (black contours at 5 hPa interval).

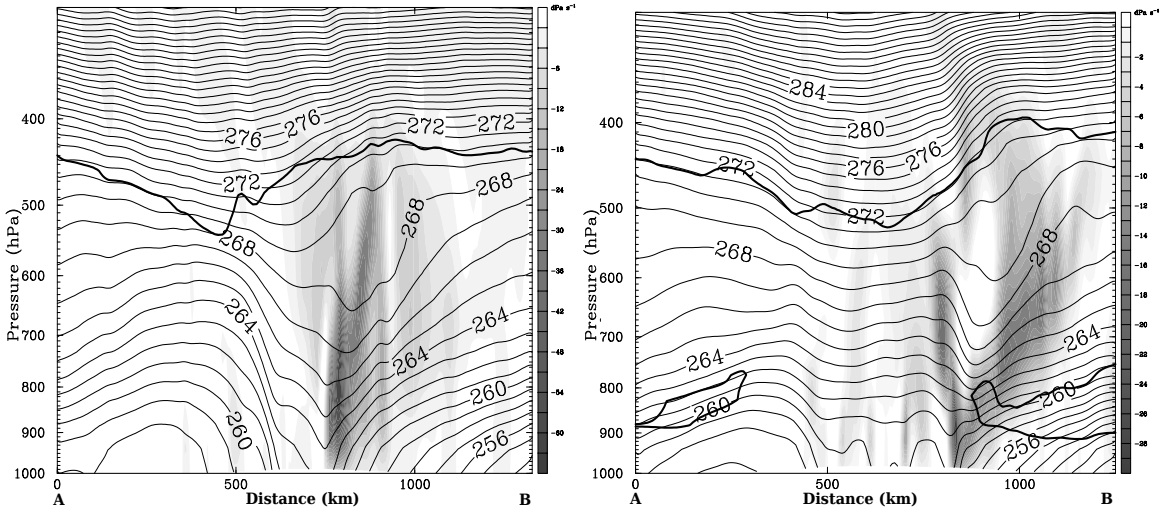

Figure 15. Vertical cross section across the PL along the lines A-B of Figure 14. Contour details are the same as in Figure 4.

result since it is a known fact that a particular variation in the baroclinicity forces a corresponding variation in the magnitude of the thermal wind to maintain the thermal wind balance. The change in the thermal wind will in turn affect the adiabatic ω-forcing as implied by the first term on the right-hand side of relation (2). Interestingly, the magnitude of the diabatic forcing too appears to be directly proportional to the degree of baroclinicity present in the troposphere. It was found that the diabatic ω-forcing was too weak to affect ω during both the phases of the PL in the B1 simulation (not shown). This is perhaps an outcome of the weakening in the intensity and the strength of the boundary layer convergence associated with the PL. As shown by Carlson (1991; pp 217), the convergence in the boundary layer is one of the major sources of diabatic forcing from to condensational heating in the clouds accompanying a cyclone.

The horizontal section of the PL during the development phase and the mature phase are shown in Figure 17. Note the weakening in the surface pressure gradient and the central pressure anomaly of the PL in both the phases for this case in comparison with the situation in the CTL simulation (Figures 3b and 3d). The horizontal scale of the PL appears to have been reduced to ~ 600 km due to the weakening of the baroclinicity in the B1 simulation (cf. ~ 1000 km in the CTL simulation). The features such as the presence of a vertical tilt in the development phase and the absence of the same in the mature phase are similar to the CTL run.

The reduction in the baroclinicity in the B1 experiment is found to have reduced the tendency for the vertical PV coupling. Figure 18 displays the vertical structure of the PL along the line AB of Figure 17b. The downward penetration depth of the upper-level PV anomaly when the mature phase was reached is roughly 1 km as indicated by the 0.5 PVU contour in the figure. In the development phase, the upper-level anomaly did not show any signs of propagating downwards (not shown). The isentropic distribution around the center of the PL shown in Figure 18 reveals that the perturbation of the baroclinicity in the B1 experiment forces a significant decrease in the strength of the lower-level frontal circulation associated with the PL when compared to Figure 4b (which represents the CTL situation). This comparison also suggests that the impacts

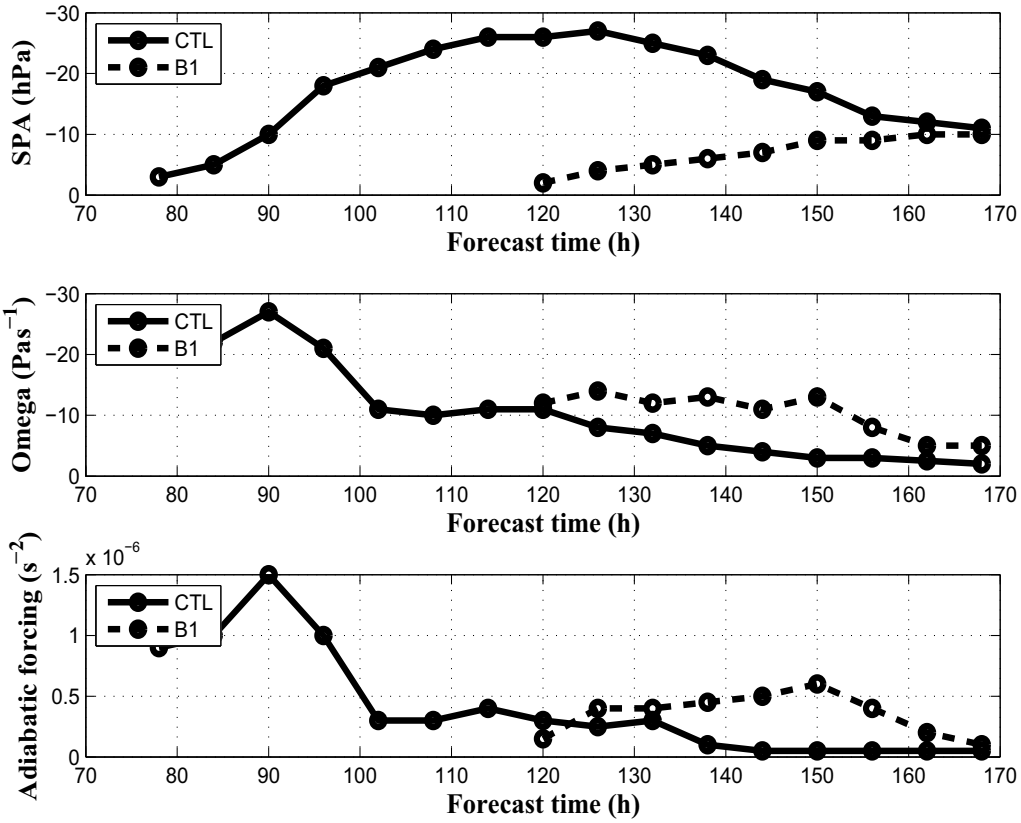

Figure 16. The evolution of surface pressure anomaly and the parameters of equation (2) for B1 and CTL simulations (SPA stands for surface pressure anomaly).

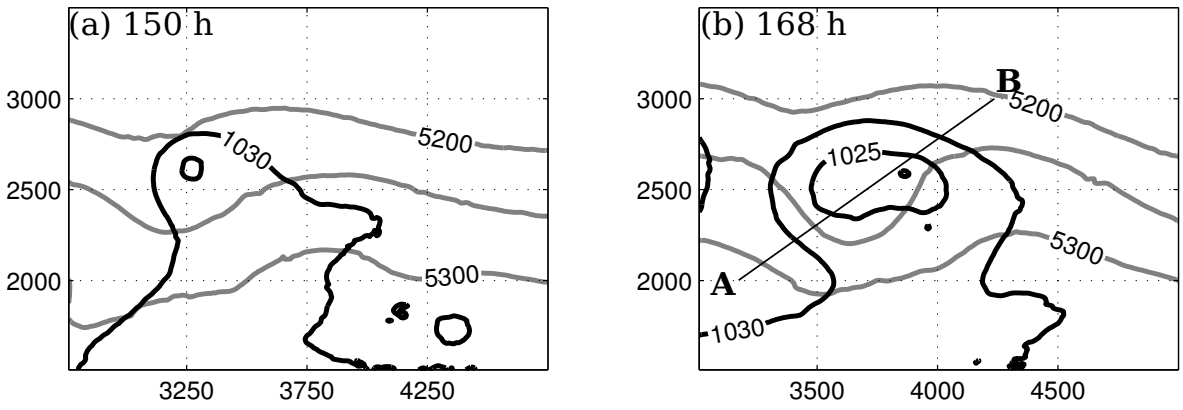

Figure 17. Horizontal cross sections across the PL in the B1 experiment showing the 500 hPa flow (gray contours at 50 m interval) and the surface pressure (black contours at 5 hPa interval).

of baroclinicity were more concentrated on the lower-level features associated with the PL than on the upper-level features. The reduction in the downward penetration depth of the upper-level PV anomaly can be seen most likely as a consequence of the weakening in the strength of the PL due to low baroclinicity.

The results of the B1 experiment suggest that the main driving mechanism of the PL tends to be more of a baroclinic nature, with the diabatic ω-forcing becoming less significant, as the baroclinicity is reduced. But it is important to note that the amount of adiabatic forcing too reduces when the baroclinicity gets weaker which in turn

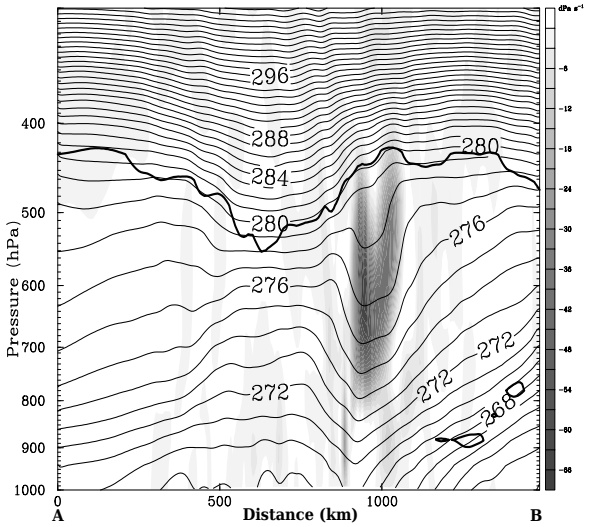

Figure 18. Vertical cross section across the PL along the lines A-B of Figure 17. Contour details are the same as in Figure 4.

results in the development of a polar low that is relatively weaker than the one developed when the baroclinicity was stronger.

3.3. Effects of the background conditions on the growth rate and phase speed of the PL

It is apparent from the above discussions that the growth of the PL in each of the sensitivity experiments differed from that in the CTL simulation. It thus becomes important to estimate the growth rate and phase speed of the PL in each of the cases to get a clear picture of the impacts of the scale of the upper-level PV anomaly, static stability, baroclinicity and surface heating on the PL growth. Table IV displays the estimated values of the growth rate and phase speed of the PL in different experiments. Since the PL grew slowly in the mature phase than in the development phase as indicated by the respective results, the growth rates have been computed separately for the two phases in all the simulations. However, for the computation of the velocity of the propagation of the PL, both the phases were combined since the PL moved in the east-northeastward direction throughout its growth. The total distance covered by the PL from the time it formed until the steady state was reached was considered while estimating the phase speed of the PL. The growth rates were computed in the simplest way possible, i.e., just by noting the rate of change of the surface pressure perturbation with time in the development and the mature phases. In a general practice, growth rate and phase speed are determined as the eigen values of different normal modes present and hence are functions of the wavelength corresponding to the individual modes. For a polar low with a wavelength in the range 800−1000 km (like the PL in the CTL simulation of this paper), the growth rate and phase speed are of the order ~ 10^{-5}s^{-1} and ~ 10 ms^{-1} (Mansfield, 1974). The values for the CTL simulation shown in the table suggest that the estimated values of the growth rate and phase speed in the present work are slightly higher but still comparable with the theoretical values.

The table reflects two aspects related to the PL growth. The first is a considerable decrease of the growth rate in the mature phase in some cases and a moreorless maintenance of the initial growth rate in the mature phase in the rest of the cases. The second aspect is the changes in the magnitudes of the growth rate and phase speed in different experiments, which accounts for the relative influence of different parameters on the growth rate and phase speed of the PL. As far as the first aspect is concerned, it has been described in section 3.2.1 that the presence of a vertical tilt of the PL axis in the mature phase caused the maintenance of the initial growth rate in the PV2 case and the absence of a vertical tilt in the mature phase caused a decrease in the growth rate in the PV1 and the CTL cases. The same reasoning applies to the rest of the experiments as well. A vertical tilt was identified in the mature phases of the N1 and θ1 experiments (not shown). The upper-level vortex was positioned over the surface vortex only when the steady state was reached in these two cases, whereas no vertical tilt was seen in the mature phase of the B1 experiment. Accordingly, the growth rate in the development phase is moreorless similar to that in the mature phase in N1 and θ1 cases while the growth rate drops considerably in the mature phase of the B1 simulation.

Regarding the second aspect, i.e., the relative influence of the key background conditions on the growth rate and phase speed of the PL, static stability seems to be the crucial most factor amongst the factors tested. For the sake of simplicity, we consider only the development phase to analyse the sensitivity of the growth rate. The growth rates in the PV1 and PV2 experiments are of a similar magnitude while that of θ1 and B1 appear to be comparable with each other, with the magnitude in the N1 experiment being the least of all. The growth rate in the latter case is lower by an order of two with respect to that in the CTL experiment. Note that, of all the sensitivity experiments, the N1 experiment is the closest to the CTL experiment (see Table-I). It is thus reasonable to assert that the growth rate of a PL is more sensitive to static stability than either to baroclinicity or surface heating/cooling or the scale of upper-level anomalies. If one compares the PV1 and PV2 cases with both the θ1 and B1 cases, it appears from the table that the growth rate of the PL is more sensitive to surface-related parameters than to upper-level related parameters. However, in terms of the phase speed, the situation is somewhat different. The phase speed of the PL seems to be equally sensitive to features connected both to upper- and lower-levels. It should be noted that both the growth rate and phase speed were determined in this paper in a direct and simple manner in contrast with the conventional dynamical way of the estimation and therefore might include some errors. Nonetheless, the qualitative nature of the results would not differ much from that presented in this paper.

3.4. Effects of the background conditions on the upward heat fluxes at the surface

Surface fluxes of sensible and latent heat provide moisture to the vortex associated with a polar low and thus are important in its growth. This section presents the results from the analysis that was based on the comparison of the magnitude of the total surface heat fluxes between different experiments. The time when the steady state was reached in different experiments was considered for the analysis. Note that this time was different in different experiments. The magnitude of the surface fluxes as the PL reached a

Table IV. The growth rate and phase speed of the PL in different experiments.

Exp.	Growth rate ($hPas^{-1}$)		Phase speed (ms^{-1})
	Development phase	**Mature phase**	
CTL	~ 2 x 10^{-4}	~ 0.8 x 10^{-4}	~ 11
PV1	~ 9 x 10^{-5}	~ 4 x 10^{-5}	~ 4.6
PV2	~ 9.3 x 10^{-5}	~ 9.3 x 10^{-5}	~ 1
N1	~ 1 x 10^{-6}	~ 0.83 x 10^{-6}	~ 8
θ1	~ 7.7 x 10^{-5}	~ 8 x 10^{-5}	~ 1
B1	~ 6.5 x 10^{-5}	~ 1.5 x 10^{-5}	~ 3.97

steady state in different experiments is shown in Table-V. In the case of the $\theta 1$ simulation, it is quite obvious that the fluxes are weaker due to the surface cooling. The PV1 and the B1 simulations are comparable in terms of the surface fluxes. The fluxes are relatively weaker in both of these simulations than the CTL simulation, the reason being a higher Richardson number (R_f) in the latter two cases with respect to that in the CTL case. Remember that the Richardson number is directly proportional to the ratio of buyoancy to the vertical wind shear (Stull, 1988; pp 175). The buyoancy was the same in PV1 and B1 cases as in the CTL case in the basic state. However, the vertical wind shear was reduced in the B1 experiment by nearly half of the CTL case and the perturbation in the PV1 experiment had indirectly led to a decrease in the wind shear. So, the denominator of R_f was smaller in PV1 and B1 simulations when compared to that in the CTL simulation while the numerator was roughly the same. This explains why the magnitude of the surface fluxes was lower in the latter two sensitivity experiments. Concerning the N1 case, which has fluxes of similar order to that of the CTL case, it should be remembered that the static stability in the N1 case was only slightly modified with respect to the CTL case. It is logical to assert that such a small variation was not sufficient to alter the magnitude of R_f and thus the influence of this perturbation on the surface fluxes was very weak. Regarding the PV2 case, neither the buyoancy nor the vertical wind shear was different from that in the CTL case and it is no surprise to have this sensitivity experiment showing the surface fluxes of the same order as the CTL experiment.

Table V. The magnitude of total surface fluxes as the PL reached its steady state in different experiments.

Exp.	Forecast time	Total upward fluxes at the surface (Wm^{-2})
CTL	120	~ 500
PV1	120	~ 360
PV2	120	~ 500
N1	144	~ 500
θ1	144	~ 330
B1	168	~ 280

4. Summary and conclusions

Development of polar lows (PL) and their sensitivity to different background conditions have been described in this paper. The experiments were carried out in an ideal baroclinic channel which has a baroclinic jet at the tropopause level superposed by a finite amplitude perturbation in the form of potential vorticity (PV) anomalies. The aim was to study the relative influences of different initial conditions on the structure and certain intrinsic features of the PLs. The PL evolves through two phases in the control (CTL) simulation; a development phase and a mature phase. The development phase is charaterised by strong vertical motion (ω) in association with the PL, rapid growth of the PL and a westward tilt of the PL axis in the vertical. This phase lasts for ~ 18 h. In the mature phase, magnitude of ω drops, the growth of the PL slows down and a steady state is reached in about 18−24 h after the onset of the mature phase. No vertical tilt of the PL axis is identified in the mature phase. Both diabatic and adiabatic ω-forcings contribute simultaneously to the magnitude of ω during the growth of the PL. A tendency for a vertical coupling of upper- and lower-level features is noticable during the mature phase of the PL in the CTL simulation.

A series of sensitivity experiments were carried out wherein the scale and structure of the upper-level anomaly, static stability, baroclinicity and surface potential temperature of the basic state were subjected to modifications. Each experiment has variation in only one of these parameters with respect to the control simulation. In all the sensitivity experiments, the formation of the PL gets delayed and its intensity reduced due to the modified initial conditions. The reduced intensity suppresses the tendency for a vertical coupling of upper- and lower-level features of the polar low. The experiments with the scale and structure of the upper-level anomaly indicate that the structure of the polar low is directly proportional to the structure of the

upper-level anomaly. A contraction of the scale of the upper-level anomaly along its meridional or zonal axis exhibits a similar effect on the structure of the PL.

It is shown that the pattern of the vertical motion associated with the PL and the degree to which individual ω-forcing terms contribute to the total vertical motion is highly sensitive to above background conditions, in particular to the baroclinicity and surface temperature. A reduction in the degree of baroclinicity inherent in the initial conditions leads to a substantial reduction in the strength of the adiabatic ω-forcing. This outcome is on expected grounds since the adiabatic forcing depends on the strength of the thermal wind, which is a measure of the baroclinicity. Interestingly, the diabatic ω-forcing becomes negligibly weak in the same experiment. This is most likely due to the weakening in the strength of the lower-level convergence associated with the PL due to reduced baroclinicity. The lower-level convergence is a major source for the diabatic forcing for cyclone developments. The results from the experiment where the surface potential temperature was decreased by 10 K appear to be similar to that of the reduced baroclinicity case, as far as the pattern of vertical motion and its forcings are concerned. In other words, the diabatic ω-forcing gets suppressed completely and the adiabatic forcing weakens due to the surface cooling. It can thus be claimed that, in these two experiments, the PL manifests as a pure baroclinic system in contrast to the CTL case where the diabatic ω-forcing was also important. This implies that the nature of a PL depends largely on the surface temperature and the amount of baroclinicity present during its development.

The static stability seems to have more influence on the growth rate of the polar low rather than on the pattern of vertical motion, when compared to the effects of other parameters tested. In an experiment where the static stability was slightly increased with respect to the CTL case, the PL has the least growth rate in comparison with the rest of the experiments. Although the magnitude of the vertical motion in this experiment is quite lower than that in the CTL experiment, it is still comparable with the CTL case. Moreover, both adiabatic and diabatic forcings are important for the total vertical motion in the higher static stability case.

The work presented in this paper was an attempt to understand the relative influence of important physical factors on the growth of polar lows. The paper presents certain interesting results regarding the sensitivity of polar lows to individual physical parameters. However, the study has focussed only on the forward-shear polar lows. The results might differ if one considers other types of polar lows such as the reverse-shear systems, the pure-convective systems, merry-go-round systems and so on. Furthermore, the initial conditions were highly ideal since the variation of the Coriolis parameter in a meridional direction (the β-effect) was neglected and there was a homogenous distribution of water at the surface. A more realistic set-up involving the application of the β-plane approximation and the inclusion of an ice-cover over some surface points would provide more information regarding the feature of polar lows that would be much closer to reality than it is now. These ideas shall be implemented in a future, probably an extension of the present, work.

Acknowledgements

This is publication no. XXXX from the Bjerknes Centre for Climate Research. The research was funded by the Norwegian Research Council's Arc-Change project which is a part of the International Polar Year (IPY) programme. The author is indebted to Dr. Heini Wernli for providing the code which was implemented in WRF for the experiments. Discussions with Dr. Idar Barstad, Dr. Haraldur Olafsson and Dr. Nils Gunnar Kvamstø are appreciated.

5. APPENDIX

An important feature of upper-level induced baroclinic cyclones is a coupling between upper- and lower-level disturbances which occurs as the cyclone intensifies (Pettersen and Smebye, 1971). Such a coupling could be effectively diagnosed through an analysis of the distribution of isentropic potential vorticity (PV, hereafter) fields during the cyclone development. After Hoskins et al. (1985) elaborated the application of isentropic potential vorticity in the diagnosis of upper-level forcing in the development of synoptic-scale cyclones, the approach has been used in analysing many cases of PL developments (Sunde et al., 1994; Røsting et al., 2003; Røsting and Kristjansson, 2006). Two important characteristics that make PV an useful diagnostic tool are the invertibility principle and the conservation of PV in an adiabatic, frictionless flow (Hoskins et al., 1985). According to the invertibility principle, it is possible to determine the distribution of wind and temperature for a particular flow once the PV associated with that flow field is known. For the sake of clarity of the discussions, the important relations from Hoskins et al. (1985) is rewritten below: The invertibility principle for a frictionless, adiabatic and axisymmetric flow in isentropic coordinates (r, θ) is given by

$$\frac{\partial}{\partial r}\left(\frac{1}{r}\frac{\partial(rv)}{\partial r}\right) + g^{-1}\xi_\theta \frac{\partial}{\partial \theta}\left(\frac{f}{R}\frac{\partial v}{\partial \theta}\right) = \sigma\frac{\partial \xi_\theta}{\partial r} \qquad \text{(A1)}$$

where v is the horizontal wind field and ξ_θ is the potential vorticity. r is the radial distance from the center of the vortex and θ refers to the potential temperature. g and f have their customary meaning. σ is the density in $xy\theta$ space. R is defined as

$$R(p) = \left(\frac{d\Pi(p)}{dp}\right)$$

where $\Pi(p)$ is called the Exner function and is given by

$$\Pi(p) = c_p\left(\frac{p}{p_0}\right)^{\kappa}$$

Equation (A1) implies that a particular anomaly in the PV $\xi(r,\theta)$ induces a similar anomaly in the wind field $v(r,\theta)$ or vice-versa. The wind anomaly induced by a PV anomaly at a particulat level in the atmosphere tends to decay exponentially above and below the location of the PV anomaly in order to preserve the thermal wind balance. The depth through which the wind field decreases by a factor e (the e-folding depth) is termed as *Rossby penetration depth* or simply *Rossby height*. In other words, *Rossby height* represents the vertical penetration depth of the upper-level PV anomaly. By using the hydrostatic balance, an expression for the *Rossby height* D can be obtained in

physical space (for the derivation, see Rasmussen and Turner, 2003 in page 367). The expression is as given below:

$$D \approx \frac{\sqrt{f(f+\zeta_\theta)}L}{N} \qquad \text{(A2)}$$

where ζ_θ is the isentropic relative vorticity, L is the horizontal scale of the PV anomaly and N is static stability. Note that the penetration depth of an upper-level PV anomaly depends on the horizontal scale of the anomaly and the static stability.

References

Adakudlu M and Barstad I. 2011. Impacts of the ice-cover and sea-surface temperature on a polar low over the Nordic seas: A numerical case study. *Quart. J. Roy. Met. Soc*. In review.

Albright MD, Reed RJ and Ovens DW. 1995. Origin and structure of a numerically simulated polar low over Hudson Bay. *Tellus* **47A**: 834-848

Businger S, Reed RJ. 1989. Cyclogenesis in Cold Air Masses. *Weather and Forecasting* **2**:133-156

Carlson TN. 1991. *Mid-latitude weather systems* Harper-Collins Academic press, London, UK

Charney J and Eliassen A. 1964. On the growth of the hurricane depression. *J. Atmos. Sci.* **21**: 68-75

Dudhia J, Hong SY and Lim KS. 2008. A new method for representing mixed-phase particle fall speeds in bulk microphysics parametrisation. *J. Met. Soc. Japan*. **86A**: 33-44.

Duncan CN. 1977. A numerical investigation of polar lows. *Quart. J. Roy. Met. Soc*. **103**: 255-68.

Duncan CN. 1978. Baroclinic instability in a reversed shear flow. *Met. Mag* **107**: 17-23.

Dyer AJ and Hicks BB. 1970. Flux-gradient relationships in the constant flux layer. *Quart. J. Roy. Meteor. Soc.* **96**. 715721.

Eady ET. 1949. Long waves and cyclone waves. *Tellus* **1**: 33-52

Farrel B. 1982. The initial growth of disturbances in a baroclinic flow. *J. Atmos. Sci* **39**: 1663-86

Farrel B. 1985. Transient growth of damped baroclinic waves. *J. Atmos. Sci* **42**: 2718-27

Fehlmann R. 1997. Dynamics of seminal PV elements. *PhD thesis, Dissertation no. 12229* **143 pp**, ETH Zürich, Switzerland

Harrold TW and Browning KA. 1969. The polar lows as a baroclinic disturbance. *Quart. J. Roy. Met. Soc*. **95**: 710-23.

Haugen JE. 1986. Numerical simulations with an idealized model. In *Proceedings of the International Conference on Polar Lows* **pp 151-60**, Norwegian Meteorological Institute, Oslo

Holton JR. 2004. An Introduction to Dynamic Meteorology.(4^{th} edn). Elsevier Academic press.

Hong SY, Dudhia J and Chen SH. 2004. A Revised Approach to Ice Microphysical Processes for the Bulk Parametrisation of Clouds and Precipitation. *Mon. Wea. Rev*. **132**: 103-120.

Hong SY and Lim JOJ. 2006. The WRF Single-Moment 6-Class Microphysics Scheme (WSM6). *J. Korean Meteor. Soc*. **42**: 129-151.

Hoskins BJ, McIntyre ME and Robertson AW. 1985. On the use and significance of isentropic potential vorticity maps. *Quart. J. Roy. Met. Soc*. **111**: 877-946.

Kain JS. 2004. The Kain-Fritsch convective parametrisation: An update. *J. Appl. Meteor*. **43**: 170-181.

Mansfield DA. 1974. Polar lows: the development of baroclinic disturbances in cold air outbreaks. *Quart. J. Roy. Met. Soc*. **100**: 541-54.

Meteorological Office. 1962. *A course in Elementary Meteorology*. HMSO. London.

Nordeng TE. 1990. A model based diagnostics study of the development and maintenance of two polar lows. *Tellus **42A***. 92-108.

Ooyama K. 1964. A dynamical model for the study of tropical cyclone development. *Geofis. Intern* **4**: 187-98

Økland H. 1977. On the intensification of small scale cyclones formed in very cold airmasses heated over the ocean. *Institute report series NO. 26*. Institutt for Geofysikk, Universitet, Oslo.

Pagowski M and Moore GWK. 2001. A Numerical Study of an Extreme Cold-Air Outbreak over the Labrador Sea: Sea Ice, AirSea Interaction, and Development of Polar Lows. *Mon. Wea. Rev* **129**:47-72.

Paulson CA. 1970. The mathematical representation of wind speed and temperature profiles in the unstable atmospheric surface layer. *J. Appl. Meteor*. **9**: 857-861.

Petterson S and Smebye SJ. 1971. On the development of extratropical cyclones. *Quart. J. Roy. Met. Soc*. **97**: 457-82.

Rasmussen E. 1979. The polar low as an extratropical CISK disturbance. *Quart. J. Roy. Met. Soc*. **105**: 531-549

Rasmussen E and Turner J. 2003. Polar lows - Mesoscale weather systems in polar regions. (1^{st} edn). Cambridge University press

Reed RJ. 1979. Cyclogenesis in polar airstreams. *Mon. Wea. Rev* **107**:38-52.

Reed RJ and Duncan CN. 1987. Baroclinic instability as a mechanism for the serial development of polar lows: a case study. *Tellus* **39A**: 376-85.

Roch M, Benoit R and Parker N. 1991. Sensitivity experiments for polar low forecasting with the CMC mesoscale finite-element model. *Atmos.-Ocean.*. **29**: 381-419.

Rotunno R, Skamarock WC and Snyder C. 1994. An analysis of frontogenesis in numerical simulations. *J. Atmos. Sci* **51**: 3373-3398

Røsting B, Kristjansson JE and Sunde J. 2003. The sensitivity of numerical simulations to initial modifications of potential vorticity - a case-study. *Quart. J. Roy. Met. Soc*. **129**: 2697-2718.

Røsting B and Kristjansson JE. 2006. Improving simulations of severe winter storms by initial modification of potential vorticity in sensitive regions. *Quart. J. Roy. Met. Soc*. **132**: 2625-2652.

Sardie JM and Warner TT. 1983. On the mechanism for the development of polar lows. *J. Atmos. Sci* **40**: 869-881.

Sardie JM and Warner TT. 1985. A numerical study of the development mechanism of polar lows. *Tellus* **37A**: 460-77.

Stull RB. 1988. An Introduction to Boundary Layer Meteorology. Dordrecht, Boston, London: Kluwer Academic Publishers.

Sunde J, Røsting B, Breivik LA, Midtbø KH and Ulstad C. 1994. Operational monitoring and forecasting of mesoscale weather phenomena in ocean regions surrounding *Norway. Met. Apps*. **1**: 237-45.

Wang W, Barker D, Bruyere C, Duda M, Dudhia J, Gill D, Michalakes J, and Rizvi S. 2008. WRF Version 3 Modeling System User's Guide. (`http://www.mmm.ucar.edu/wrf/users/docs/arw_v3.pdf`)

Webb EK. 1970. Profile relationships: The log-linear range, and extension to strong stability. *Quart. J. Roy. Meteor. Soc.* **96**: 6790.

Wernli H, Shapiro MA and Schmidli J. 1999. Upstream development in idealized baroclinic wave experiments. *Tellus* **51A**: 574-87.

Wiin-Nielsen. 1989. On the precursors of polar lows. In *Polar and Arctic lows*. ed. P. F. Twitchell, E. Rasmussen and K. L. Davidson. pp. 85-107. A Deepak, Hampton, VA.

Yanase W and Niino H. 2007. Dependence of Polar Low Development on Baroclinicity and Physical Processes: An Idealized High-Resolution Numerical Experiment. *J. Atmos. Sci*. **64**: 3044-3067.

Bibliography

Albright MD, Reed RJ and Ovens DW. 1995. Origin and structure of a numerically simulated polar low over Hudson Bay. *Tellus* **47A**: 834-848.

Barstad I and Grønås S. 2005. Southwesterly flows over southern Norway - mesoscale sensitivity to large-scale wind direction and speed. *Tellus*. **57A**: 136-152.

Barstad I and Grønås S. 2006. Dynamical structures for southwesterly airflow over southern Norway: the role of dissipation. *Tellus*. **58A**: 2-18.

Barstad I, Kristjansson JE, Hov Ø, Shapiro M, Irvine E, Dörnbrack A, Probst F, Ólafsson H, Storvold R, Sætra Ø. 2008. The main observational campaign of the IPY-THORPEX-NORWAY project. *Technical report R29*. Bjerknes Centre for Climate Research.
(`http://www.uib.no/People/ngfib/R29.pdf`)

Bluestein HB. 1993. *Synoptic-dynamic meteorology in midlatitudes (2 vols)*. Oxford University Press, Oxford.

Bracegirdle TJ and Gray SL. 2008. An objective climatology of the dynamical forcing of polar lows in the Nordic Seas. *Int. J. Climatol.* **28**: 1903-1919.

Businger S. 1985. The synoptic climatology of polar-low outbreaks. *Tellus* **37A**: 419-432.

Businger S, Reed RJ. 1989a. Cyclogenesis in Cold Air Masses. *Weather and Forecasting* **2**:133-156.

Businger S, Reed RJ. 1989b. Polar lows. In Polar and Arctic Lows, ed. P.F. Twitchell, E. Rasmussen and K.L. Davidson. pp. 3-45. A Deepak, Hampton, VA.

Carleton AM. 1995. On the interpretation and classification of mesoscale cyclones from satellite infrared imagery. *Int. J. Rem. Sens*. **16**: 2457-2485.

Charney JG. 1947. The dynamics of long waves in a baroclinic westerly current. *J. Meteor.*. **4**: 135-162.

Charney J and Eliassen A. 1964. On the growth of the hurricane depression. *J. Atmos. Sci.* **21**: 68-75

Dannevig P. 1954. *Meteorologi for Flygere (in Norwegian).* Aschehoug, Oslo.

Drange H, Dokken T, Furevik T, Gerdes R, Berger W, Nesje A, Orvik KA, Skagseth Ø, Skjelvan I and Østerhus S. 2005. The Nordic Seas: An Overview. *Geophysical Monograph, Americal Geophysical Union, Washington, DC*. **158**: 1-11.

Duncan CN. 1977. A numerical investigation of polar lows. *Quart. J. Roy. Met. Soc*. **103**: 255-68.

Duncan CN. 1978. Baroclinic instability in a reversed shear flow. *Met. Mag* **107**: 17-23.

Eady ET. 1949. Long waves and cyclone waves. *Tellus* **1**: 33-52

Emanuel KA. 1986a. An air-sea interaction theory for tropical cyclones. Part I: steady state maintenance. *J. Atmos. Sci*. **43**: 585-604.

Emanuel KA and Rotunno R. 1989. Polar lows as arctic hurricanes. *Tellus*. **41A**: 1-17.

Gaberšek S and Durran DR. 2004. Gap flows through idealized topography. Part I: Forcing by large-scale winds in the non-rotating limit. *J. Atmos. Sci.* **61**: 2846-2862.

Grønås S et al 1986. Numerical simulations of polar lows in the Norwegian Sea. Part I: The model and simulations of the polar low 26-27 February 1984. *Polar Lows Project. Technical Report No. 5.* The Norwegian Meteorological Institute, Oslo, Norway.

Grønås S, Foss A and Lystad M. 1987a. Numerical simulations of polar lows in the Norwegian Sea. *Tellus*. **39A**: 334-354.

Grønås S, Foss A and Lystad M. 1987b. The Norwegian mesoscale NWP system. *Proceedings of the Symposium on Mesoscale Analysis and Forecasting, Vancouver, Canada*. ESA SP-282.

Grønås S and Hellevik OE. 1982. A limited area prediction model at the Norwegian Meteorological Institute. *Technical Report no. 61*. Norwegian Meteorological Institute, Oslo.

Grønås S and Kvamstø NG. 1995. Numerical simulations of the synoptic conditions and development of Arctic outbreak polar lows. *Tellus* **47A**: 797-814.

Grønås S and Sandvik AD. 1999. Numerical simulations of local winds over steep orography in the storm over North Norway on October 12, 1996. *J. Geophys. Res.*

104:9107-9120.

Grønås S and Skeie P. 1999. A case study of strong winds at an Arctic front. *Tellus*. **51A**: 865-879.

Harold JM, Bigg GR and Turner J. 1999a. Mesocyclone activity over the North-East Atlantic. Part I: Vortex distribution and variability. *Int. J. Climatol*. **19**: 1187-1204.

Harold JM, Bigg GR and Turner J. 1999b. Mesocyclone activity over the North-East Atlantic. Part II: An investigation of causal mechanisms. *Int. J. Climatol*. **19**: 1283-1299.

Harrold TW and Browning KA. 1969. The polar lows as a baroclinic disturbance. *Quart. J. Roy. Met. Soc*. **95**: 710-23.

Heinemann G. 1998. A mesoscale model-based study of the dynamics of a winter-time polar low in the Weddel Sea region of the Antarctic during the Winter Weddel Sea Program field phase 1986. *J. Geophys. Res*, **103**, 5983-6000.

Hewson TD. 1998a. A frontal wave database. Joint Centre for Mesoscale Meteorology (JCMM) internal report, 57. Department of Meteorology, The University of Reading: Reading.

Holton JR. 2004. An Introduction to Dynamic Meteorology.(4^{th} edn). Elsevier Academic press.

Hoskins BJ, McIntyre ME and Robertson AW. 1985. On the use and significance of isentropic potential vorticity maps. *Quart. J. Roy. Met. Soc*. **111**: 877-946.

Hoskins BJ and Hodges KI. 2002. New perspectives on the Northern Hemisphere winter storm tracks. *J. Atmos. Sci.* **59**: 1041-1061.

Hoskins BJ and Bretherton FP. 1972. Atmospheric frontogenesis: mathematical formulation and solution. *J. Atmos. Sci.* **29**: 11-37.

King JC and Turner J. 1997. Antarctic Meteorology and Climatology. Cambridge Atmospheric and Space Science Series, Cambridge University Press.

Kolstad EW. 2006. A new climatology of favourable conditions for reverse-shear polar lows. *Tellus*. **58A**: 344-354.

Kolstad EW. 2007. Extreme winds in the Nordic Seas: polar lows and Arctic fronts in a changing climate. *PhD Thesis, University of Bergen, Norway*.

Kolstad EW and Bracegirdle TJ. 2008. Marine cold-air outbreaks in the future: an assessment of IPCC AR4 model results for the Northern Hemisphere. *Climate Dynamics*. **30**: 871-885.

Kristjansson JE, Barstad I, Aspelien T, Føre I, Godøy Ø, Hov Ø, Irvine EA, Iversen T, Kolstad EW, Nordeng TE, McInnes H, Randriamampianina R, Reuder J, Saetra Ø, Shapiro MA, Spengler T, Ólafsson H. 2010. The Norwegian IPY-THORPEX: Polar Lows and Arctic Fronts during the 2008 Andøya campaign, *Bull. Amer. Met. Soc.* submitted.

Lystad M. 1986. *Polar lows in the Norwegian, Greenland and Barents Seas. Final report, Polar lows Project*. Norwegian Meteorological Institute, Oslo.

Mansfield DA. 1974. Polar lows: the development of baroclinic disturbances in cold air outbreaks. *Quart. J. Roy. Met. Soc*. **100**: 541-54.

Moore G and Renfrew I. 2005. Tip jets and barrier winds: A QuickSCAT climatology of high wind speed events around Greenland. *J. Climate*. **18**: 3713-3725.

Nielsen NW. 1997. An early-autumn polar low formation over the Norwegian Sea. *J. Geophys. Res.−Atmos.* **102**: 13955-13973.

Nordeng TE. 1987. The effect of vertical and slantwise convection on the simulation of polar lows. *Tellus*. **39A**: 354-376.

Nordeng TE. 1990. A model based diagnostics study of the development and maintenance of two polar lows. *Tellus **42A***. 92-108.

Nordeng TE and Rasmussen EA. 1992. A most beautiful polar low - a case study of a polar low development in the Bear Island region. *Tellus*. **44A**: 81-99.

Norhagen A. 2004. Arktiske fronter og sterk vind. *Master thesis, University of Bergen, Norway*.

Ooyama K. 1964. A dynamical model for the study of tropical cyclone development. *Geofis. Intern* **4**: 187-98

Økland H. 1977. On the intensification of small scale cyclones formed in very cold airmasses heated over the ocean. *Institute report series NO. 26*. Institutt for Geofysikk, Universitet, Oslo.

Økland H. 1998. Modifications of frontal circulations by surface heat flux. *Tellus*. **50A**: 211-218.

Petersen GN, Renfrew IA and Moore GWK. 2009. An overview of barrier winds off southeastern Greenland during the Greenland Flow Distortion Experiment. *Quart. J. Royal. Met. Soc*. **135**: 1950-1967.

Rabbe A. 1987. A polar low over the Norwegian Sea, 29 February−1 March 1984. *Tellus*. **39A**: 326-333.

Ralph FM, Shapiro MA, Neiman PJ and Miletta J. 1994. Observations of multiple mesoscale cyclones (50−700 km) within synoptic scale cyclones. *Proceedings, International Symposium on the life cycles of Extratropical Cyclones, 27 June−1 July 1994, Bergen, Norway, Vol. III, pp 192-198.*

Rasmussen EA. 1977. The polar low as a CISK phenomena. *University of Copenhagen, Institute for Theoretical Meteorology, Copenhagen*.

Rasmussen EA. 1979. The polar low as an extratropical CISK disturbance. *Quart. J. Roy. Met. Soc*. **105**: 531-49.

Rasmussen EA and Lystad M. 1987. The Norwegian polar lows project: a summary of the international conference on polar lows. *Bull. Amer. Met. Soc.*. **68**: 801-816.

Rasmussen EA and Turner J. 2003. Polar lows - Mesoscale weather systems in polar regions. (1^{st} edn). Cambridge University press

Reed RJ. 1979. Cyclogenesis in polar airstreams. *Mon. Wea. Rev.* **107**: 38-52.

Reed RJ and Duncan CN. 1987. Baroclinic instability as a mechanism for the serial development of polar lows: a case study. *Tellus* **39A**: 376-85

Renfrew IA, Moore GWK, Kristjansson JE, Ólafsson H, Gray SL, Petersen GN, Bovis K, Brown PRA, Føre I, Haine T, Hay T, Irvine EA, Lawrence A, Ohigashi T, Outten S, Pickart RS, Shapiro MA, Sproson D, Swinbank R, Woolley A and Zhang S. 2008. The Greenland Flow Distortion Experiment. *Bull. Amer. Met. Soc.*. **89**: 1307-1324.

Roch M, Benoit R and Parker N. 1991. Sensitivity experiments for polar low forecasting with the CMC mesoscale finite-element model. *Atmos.-Ocean.*. **29**: 381-419.

Røsting B, Kristjansson JE and Sunde J. 2003. The sensitivity of numerical simulations to initial modifications of potential vorticity - a case-study. *Quart. J. Roy. Met. Soc*. **129**: 2697-2718.

Røsting B and Kristjansson JE. 2006. Improving simulations of severe winter storms by initial modification of potential vorticity in sensitive regions. *Quart. J. Roy. Met. Soc*. **132**: 2625-2652.

Sandvik AD and Furevik BR. 2002. Case Study of a Coastal Jet at Spitsbergen - Comparison of SAR-and Model-Estimated Wind. *Mon. Wea. Rev.* **130**: 1040-1051.

Sardie JM and Warner TT. 1985. A numerical study of the development mechanism of polar lows. *Tellus* **37A**: 460-77.

Schär C and Smith R. 1993. Shallow-water flow past isolated topography, I: Vorticity production and wake formation. *J. Atmos. Sci*. **50**: 1373-1400.

Serreze MC, Kahl JD and Schnell RC. 1992. Low-level temperature inversions of the Eurasian Arctic and comparisons with Soviet drifting station data. *J. Climate*. **5**: 615-629.

Shapiro MA, Fedor LS and Hampel T. 1987. Research aircraft measurements of a polar low over the Norwegian Sea. *Tellus*. **39A**: 272-306.

Shapiro MA, Hampel T and Fedor LS. 1989. Research aircraft observations of an Arctic front over the Barents Sea. In *Polar and Arctic lows*, ed. P.F. Twitchell, E. Rasmussen and K.L. Davidson. pp. 279-289. A Deepak, Hampton, VA.

Skeie P and Grønås S. 2000. Strongly stratified easterly flows across Spitsbergen. *Tellus*. **52A**; 473-486.

Smith R. 1989a. Hydrostatic airflow over mountains. In: Advances in geophysics. Academic Press Inc.

Smolarkiewicz P and Rotunno R. 1989. Low Froude number flow past three-dimensional obstacles. Part I: Baroclinically generated lee vortices. *J. Atmos. Sci.*. **45A**: 28-43.

Sumner EJ. 1950. The significance of vertical stability in synoptic development. *Quart. J. Roy. Met. Soc.* **76**: 384-392.

Sunde J, Røsting B, Breivik LA, Midtbø KH and Ulstad C. 1994. Operational monitoring and forecasting of mesoscale weather phenomena in ocean regions surrounding. *Norway. Met. Apps*. **1**: 237-45.

Thompson WT and Burk SD. 1991. An investigation of an Arctic front with a vertically nested mesoscale model. *Mon. Wea. Rev.* **119**: 233-261.

Thorpe AJ and Emanuel KA. 1985. Frontogenesis in the presence of small sability to slantwise convection. *J. Atmos. Sci.*. **42**: 1809-1824.

Wagner JS. 2011. The mesoscale structure of a polar low: simulations and airborne measurements. *Diploma thesis, University of Innsbruck*.

Wilhelmsen K. 1985. Climatological study of gale-producing polar lows near Norway. *Tellus*. **37A**: 451-459.

Yanase W and Niino H. 2007. Dependence of Polar Low Development on Baroclinicity and Physical Processes: An Idealized High-Resolution Numerical Experiment. *J. Atmos. Sci*. **64**: 3044-3067.

Zängl G. 2002. Stratified flow over a mountain with a gap: Linear theory and numerical simulations. *Quart. J. Roy. Met. Soc*. **128**: 927-949.